

# Doctoral Thesis

Thesis Title

Development of a Novel Reactivity Index for  
Spark-Ignited Engine Fuels Based on Separated Weak  
Flames in a Micro Flow Reactor with a Controlled  
Temperature Profile

Department of Mechanical Systems and Design,  
Graduate School of Engineering,  
TOHOKU UNIVERSITY

PHILIPP GRAJETZKI

(ID No. B5TD1004)



Advising Professor at Tohoku Univ.	Professor Maruta, Kaoru
Research Advisor at Tohoku Univ.	
Dissertation Committee Members Name marked with “○” is the Chief Examiner	<u>○ Prof. Maruta, Kaoru</u> <u>1 Prof. Kobayashi, Hideaki</u> <u>2 Associate Prof. Nakamura, Hisashi</u>



TOHOKU UNIVERSITY  
Graduate School of Engineering

Development of a Novel Reactivity Index for Spark-Ignited Engine Fuels Based on Separated Weak  
Flames in a Micro Flow Reactor with a Controlled Temperature Profile

温度分布制御型マイクロフローリアクタ内の分離 weak flame に基づく火花点式機関の燃料  
のための新規反応性指標の開発

A dissertation submitted for the degree of Doctor of Philosophy (Engineering)

Department of Mechanical Systems and Design

by

Philipp GRAJETZKI

July 5, 2019



# Development of a Novel Reactivity Index for Spark-Ignited Engine Fuels Based on Separated Weak Flames in a Micro Flow Reactor with a Controlled Temperature Profile

Philipp Grajetzki

## Abstract

The automotive sector is among the largest contributors of worldwide CO<sub>2</sub> emissions, which contributes to global warming. As the numbers of vehicles with combustion engines is predicted to keep on rising, an increase of efficiency and, therefore, a decrease of emissions are of high priority. The maximum thermal efficiency in a gasoline engine is determined by the compression ratio. The maximum compression ratio, however, is limited by the occurrence of engine knocking, i.e., spontaneous auto-ignition of the fuel/air mixture. Therefore, a profound understanding of fuel reactivity is of high importance. Common methods for the determination of fuel reactivity include the measurement of ignition delay times in shock tubes and rapid compression machines as well as the determination of critical compression ratios. Recently, our group has investigated fuel reactivity by weak flames in a micro flow reactor with a controlled temperature profile (MFR). For low flow velocities, reaction zones separate into cool flames at low temperatures, blue flames at intermediate temperatures and hot flames at high temperatures. The goal of this thesis is to use these separated weak flames to develop a quantitative index that describes fuel reactivity in a comprehensive manner.

The first focus of this thesis was on the effect of ultra-lean conditions on the fuel reactivity. Under these conditions, excess air decreases the combustion temperature, which leads to lower thermal losses and therefore to increased thermal efficiency. Experimental results of the separated weak flames showed blue flames at intermediate temperatures and hot flames at high temperatures. Leaner conditions shifted the flames to lower temperatures, which indicated higher reactivity. Steady one-dimensional simulations by the KUCRS reaction mechanism, on the other hand, showed the opposite trend. Important reactions that lead to this behavior were investigated and several key reactions were identified. All these reactions included hydrogen- oxygen radicals. By comparing the rate parameters of these reactions to those of other reaction mechanisms, important differences in seven reactions were found. By modifying these rate parameters, the computational results showed very good agreement with the experiment. The effect of this modification was also tested on computational results of ignition delay times and laminar flame speeds. For these investigation methods, the changes did not exhibit any effect. This showed that by using weak flames in a MFR with a controlled temperature profile, chemical effects could be investigated.

The next step was the development of a quantitative reactivity index based on separated weak flames. To this end, the weak flames of fuels with research octane numbers (RON) between 0 and 100 were investigated at elevated pressure of 500 kPa, which is close to practical conditions. This increase of pressure resulted in stronger cool flames and blue flames as well as a shift of cool flames, blue flames and hot flames to lower temperatures. It was observed that the heat release in the hot flame was the same for all fuels. Large differences, however, existed

between the heat release in the cool flame and the blue flame. Fuels of low RON, i.e., fuels of high reactivity showed relatively strong heat release in the cool while fuels of high RON showed larger heat release in the blue flame. This observation led to the creation of the heat contribution index (HCI). It is the ratio of heat that is released in one of the separated weak flames to the total heat release. While the correlation between HCI and RON was weak, the HCI showed a strong dependence on the molecular structure of the fuel. Straight chain molecules showed high heat release in the cool flame, while more branched molecules showed higher heat release in the blue flame. This characteristic is governed by low temperature chain branching, which requires less energy in the case of straight chain molecules. Additionally, formaldehyde concentrations were measured in the experiments. High concentrations indicated high reactivity, which agreed well with the findings by the HCI. Furthermore, the HCI showed good agreement with critical compression ratios. These results showed that the HCI allows for comprehensive measurement of fuel reactivity.

The last part of this study investigated the effect of  $N_2$ ,  $CO_2$  and  $H_2O$  on the reactivity of *iso*-octane and *n*-heptane. In actual applications, this kind of exhaust gas recirculation shows three effects, namely the thermal effect, the chemical effect and the dilution effect. By using weak flames in the MFR, the thermal effect is eliminated and allows for detailed investigation of the chemical and dilution effects. In order to allow for better comparison between the flame locations in the experiment and in the simulation, photon emission by excited radicals was calculated and showed very good agreement with experimental chemiluminescence. In the experiment, the addition of  $N_2$  and  $CO_2$  shifted the cool flame, blue flame and hot flame to higher temperatures, indicating lower reactivity.  $H_2O$ , however, showed a shift to lower temperatures, which indicated higher reactivity. As the thermal effect was eliminated by the MFR setup, the chemical effect of  $H_2O$  became dominant, which enhanced reactivity at intermediate temperatures. Evaluation of computational results by the HCI showed a similar effect. While the dilution effect was dominant for the cool flame and decreased its reactivity, the chemical effect of  $H_2O$  was dominant on the blue flame where it increased reactivity. This again showed the capability of the MFR and the newly introduced HCI in evaluating fuel reactivity under a wide range of conditions.



# Contents

<b>1</b>	<b>Introduction</b>	<b>1</b>
1.1	Background of this thesis . . . . .	1
1.2	SIP project . . . . .	3
1.2.1	Super-lean combustion . . . . .	4
1.2.2	Exhaust gas recirculation . . . . .	6
1.2.3	Gasoline surrogates . . . . .	7
1.2.4	KUCRS reaction mechanism . . . . .	9
1.3	Common methods for the investigation of fuel reactivity . . . . .	10
1.3.1	Shock tubes . . . . .	10
1.3.2	Rapid compression machines . . . . .	11
1.3.3	Octane numbers . . . . .	13
1.4	Micro flow reactor with a controlled temperature profile . . . . .	13
1.5	Objectives and outline of this thesis . . . . .	20
<b>2</b>	<b>Evaluation of the reactivity of ultra-lean PRF/air mixtures by weak flames</b>	<b>23</b>
2.1	Introduction . . . . .	23

2.2	Methods . . . . .	26
2.2.1	Experimental method . . . . .	26
2.2.2	Computational method . . . . .	30
2.3	Results and discussion . . . . .	31
2.3.1	Flame locations and temperatures . . . . .	31
2.3.2	Effect of the equivalence ratio on chemical reactions . . . . .	36
2.3.3	Modification of H-O reaction parameters . . . . .	41
2.3.4	Validation by ignition delay times and laminar burning velocities . . . . .	53
2.4	Conclusions . . . . .	56
	<b>Appendix</b>	<b>59</b>
2.A	MFR setup . . . . .	59
2.B	Temperature measurement . . . . .	61
2.C	Applicability of modified KUCRS at elevated pressure . . . . .	64
2.D	Effect of equivalence ratio on SIP gasoline surrogates . . . . .	66
<b>3</b>	<b>A novel reactivity index for SI engine fuels by separated weak flames</b>	<b>69</b>
3.1	Introduction . . . . .	69
3.2	Method . . . . .	73
3.2.1	Experimental method . . . . .	73
3.2.2	Computational method . . . . .	75
3.3	Results . . . . .	76
3.3.1	Experimental weak flame locations . . . . .	76
3.3.2	Computational weak flame locations . . . . .	78
3.3.3	Computational flame structure . . . . .	80

3.3.4	Fuel reactivity by heat contribution index . . . . .	84
3.4	Conclusions . . . . .	94
<b>Appendix</b>		<b>97</b>
3.A	Cool flame temperature profile . . . . .	97
3.B	Fuel structure and HCI . . . . .	98
3.C	HCI of lean mixtures . . . . .	99
3.D	HCI of other fuels . . . . .	100
<b>4</b>	<b>Investigation of the chemical and dilution effects of major EGR constituents</b>	
	<b>on the reactivity of PRF by weak flames</b>	<b>103</b>
4.1	Introduction . . . . .	103
4.2	Method . . . . .	105
4.2.1	Experimental method . . . . .	105
4.2.2	Computational method . . . . .	107
4.3	Results . . . . .	109
4.3.1	Experimental results . . . . .	109
4.3.2	Computational results . . . . .	112
4.3.3	Determination of flame location . . . . .	114
4.3.4	Effect of pressure and EGR-like dilution on stoichiometric flame	
locations . . . . .		118
4.3.5	Effect of EGR diluents on <i>iso</i> -octane weak flames . . . . .	121
4.3.6	Effect of EGR diluents on <i>n</i> -heptane weak flames . . . . .	126
4.3.7	Heat contribution index . . . . .	133
4.4	Conclusions . . . . .	138

<b>Appendix</b>	<b>141</b>
4.A Results for LLNL . . . . .	141
<b>5 Conclusions and outlook</b>	<b>147</b>
5.1 Conclusions . . . . .	147
5.2 Outlook . . . . .	150
<b>6 Bibliography</b>	<b>151</b>
<b>7 Acknowledgments</b>	<b>171</b>

# List of Figures

1.1	Evolution of global light duty vehicle sales by technology type [2]. . . . .	2
1.2	Schematic of super-lean burn concept for gasoline engines [13]. . . . .	5
1.3	Typical operation regimes of shock tubes (ST) and rapid compression machines (RCM) [46]. . . . .	11
1.4	Two-stage ignition of <i>iso</i> -octane/air mixture [55]. . . . .	12
1.5	Schematic of the horizontal-type micro flow reactor with a controlled temperature profile [68]. . . . .	14
1.6	Measured positions of the normal flame, weak flame as well as ignition and extinction points of FREI. . . . .	16
1.7	Influence of research octane number (RON) on flame separation and location at $P = 100$ kPa and $\Phi = 1.0$ for various fuels. . . . .	17
1.8	Effect of $N_2$ , $CO_2$ and $H_2O$ on the hot flame of stoichiometric syngas/air mixtures at 100 kPa [76]. . . . .	19
1.9	Weak flame images of stoichiometric <i>n</i> -butane/air mixture between 0.1 MPa and 0.3 MPa [75]. . . . .	19

2.1	Influence of RON on weak flame patterns and positions at $\Phi = 1.0$ and $P = 100$ kPa by a horizontal-type MFR [73]. . . . .	25
2.2	Scheme of the vertical-type micro flow reactor with a controlled temperature profile. . . . .	26
2.3	Experimentally measured wall temperatures and fitted quadratic approximation between 373 K and 1300 K. . . . .	28
2.4	Experimental weak flame images of all nine cases. . . . .	31
2.5	Heat release rates of PRF100 with LLNL and KUCRS at $\Phi = 1.0, 0.75$ and $0.5$ and $P = 100$ kPa. . . . .	33
2.6	Wall temperature at hot flame location for all investigated cases ( $P = 100$ kPa), experiments and simulations. . . . .	34
2.7	Major species profiles for PRF100 at $P = 100$ kPa and $\Phi = 1.0$ by LLNL. . . . .	35
2.8	Normalized rate of progress variables at $T_{\text{wall}} = 1030$ K for major ten reactions as obtained by LLNL for PRF100 at $P = 100$ kPa and $\Phi = 1.0$ and $0.5$ . . . . .	36
2.9	Normalized rate of progress variables at $T_{\text{wall}} = 1030$ K for major ten reactions as obtained by KUCRS for PRF100 at $P = 100$ kPa and $\Phi = 1.0$ and $0.5$ . . . . .	38
2.10	Sensitivity coefficients with regard to the wall temperature at the hot flame location as obtained by KUCRS. . . . .	40
2.11	Sum of rate constants of K1938+K1939 multiplied by $[M]$ for KUCRS and rate constant of L26 for FFCM at $P = 100$ kPa and $\Phi = 1.0$ and $0.5$ . . . . .	46
2.12	Rate constants of reaction K1944: $\text{OH} + \text{HO}_2 \rightleftharpoons \text{H}_2\text{O} + \text{O}_2$ . . . . .	49

2.13	Heat release rate profiles of original KUCRS and KUCRS+FFCM for PRF100 at $P = 100$ kPa and $\Phi = 1.0$ and $0.5$ . . . . .	50
2.14	Wall temperature at hot flame location for all investigated cases, experiments and simulations including KUCRS+FFCM. . . . .	51
2.15	CH <sub>2</sub> O mole fraction profiles of original KUCRS and KUCRS+FFCM of PRF100 at $P = 100$ kPa and $\Phi = 1.0$ and $0.5$ . . . . .	52
2.16	Ignition delay times of original KUCRS and KUCRS+FFCM for PRF100 at $P = 500$ kPa and $\Phi = 1.0$ and $0.5$ . . . . .	54
2.17	Laminar burning velocities for <i>iso</i> -octane at 100 kPa and 298 K as obtained by KUCRS and KUCRS+FFCM. . . . .	55
2.A.1	Scheme of the vertical-type micro flow reactor setup. . . . .	59
2.A.2	Heated mixing tank. . . . .	60
2.B.1	Thermocouple inserted into the MFR from the lower end. . . . .	61
2.B.2	Temporal temperature profile in the low temperature region, i. e., upper part of the MFR. . . . .	62
2.B.3	Histogram of temperature profile in Fig. 2.B.2. . . . .	62
2.B.4	Temporal temperature profile in the high temperature region, i. e., lower part of the MFR. . . . .	63
2.B.5	Histogram of temperature profile in Fig. 2.B.4. . . . .	64
2.C.1	Effect of equivalence ratio on <i>iso</i> -octane weak flames at elevated pressure. . . . .	65
2.C.2	Wall temperature at hot flame of experiment and computations by LLNL, KUCRS and KUCRS+FFCM. . . . .	66
2.D.1	Wall temperature at experimental hot flame location of gasoline surrogates with RON = 90 at 100 kPa. . . . .	67

3.1.1	Critical compression ratios of various alkanes at 600 rpm and 450 K, $\Phi = 1.0$ .	70
3.3.1	Weak flame images of <i>iso</i> -octane and <i>n</i> -heptane at $\Phi = 1.0$ and pressures between 100 kPa and 500 kPa. . . . .	77
3.3.2	Intensity along the center of images in Fig. 3.3.1. . . . .	78
3.3.3	Computational heat release rate profiles by modified KUCRS of <i>iso</i> -octane and <i>n</i> -heptane at $\Phi = 1.0$ and pressures between 100 kPa and 500 kPa. . .	79
3.3.4	Computational species profiles by modified KUCRS of <i>iso</i> -octane at $\Phi = 1.0$ and pressures of 100 kPa and 500 kPa. . . . .	81
3.3.5	Computational species profiles by modified KUCRS of <i>n</i> -heptane at $\Phi = 1.0$ and pressures of 100 kPa and 500 kPa. . . . .	82
3.3.6	Heat release rate by modified KUCRS for different fuels at $\Phi = 1.0$ and 500 kPa. . . . .	83
3.3.7	The heat contribution index of the cool flame, blue flame and hot flame at $\Phi = 1.0$ and $P = 500$ kPa plotted over the RON. . . . .	85
3.3.8	Critical compression ratio (taken from Lovell [114]) and blue flame index over number of C atoms in molecule. . . . .	87
3.3.9	CH <sub>2</sub> O mole fraction profiles as obtained by modified KUCRS at $\Phi = 1.0$ and $P = 500$ kPa. . . . .	90
3.3.10	Blue flame index and formaldehyde index for simulation and experiment over number of carbon atoms in molecule. . . . .	91
3.3.11	Measured CH <sub>2</sub> O area and error bars of <i>n</i> -heptane over maximum wall temperature at 500 kPa. . . . .	92
3.3.12	Estimation of the linear relationship between experimental formaldehyde index and critical compression ratio as taken from Lovell [114]. . . . .	93



3.A.1	Wall temperature profile with $T_{\max} = 723$ K and image of <i>iso</i> -octane cool flame at 500 kPa and $\Phi = 1.0$ . . . . .	97
3.B.1	Relationship between fuel structure and Blue flame-HCI. . . . .	98
3.C.1	Heat contribution indexes of PRF0-100, S3R and Toluene at $P = 500$ kPa and $\Phi = 1.0$ and 0.5. . . . .	100
3.D.1	Comparison of critical compression ratio [114] on the left side and Blue flame-HCI by modified KUCRS for various fuels at 500 kPa and $\Phi = 1.0$ on the right side. . . . .	101
4.3.1	Weak flame images of <i>iso</i> -octane at $P = 200$ kPa and $\Phi = 1.0$ for dilution ratios of 0%, 20% and 50% of $N_2$ , $CO_2$ and $H_2O$ (only 20%). . . . .	110
4.3.2	Luminosity profiles of <i>iso</i> -octane at $P = 200$ kPa and $\Phi = 1.0$ for $CO_2$ dilution ratios of 0%, 20% and 50%. . . . .	111
4.3.3	Weak flame images of <i>iso</i> -octane for a dilution ratio of 20% $CO_2$ at $\Phi = 1.0$ and pressures between 100 kPa and 500 kPa. . . . .	112
4.3.4	Luminosity profiles (intensity of blue color channel of RGB image) of <i>iso</i> -octane for a dilution ratio of 20% $CO_2$ at $\Phi = 1.0$ and pressures between 100 kPa and 500 kPa. . . . .	113
4.3.5	Heat release rate profiles of <i>iso</i> -octane at $P = 200$ kPa and $\Phi = 1.0$ for $CO_2$ -dilution ratios of 0%, 20% and 50%, as obtained by the modified KUCRS mechanism. . . . .	114
4.3.6	Luminosity profiles of <i>iso</i> -octane for a dilution ratio of 20% $CO_2$ at $\Phi = 1.0$ and pressures between 100 kPa and 500 kPa, as obtained by the modified KUCRS mechanism. . . . .	115

4.3.7	Comparison of experimental luminosity profile of <i>iso</i> -octane for a dilution ratio of 20% CO <sub>2</sub> at $\Phi = 1.0$ and $P = 200$ kPa with computational results for photon emission. . . . .	117
4.3.8	Wall temperature at the blue flame and hot flame positions of <i>iso</i> -octane at $\Phi = 1.0$ and pressures between 100 kPa and 500 kPa. . . . .	119
4.3.9	Main reaction pathways of hydrogen-oxygen reactions at $\Phi = 1.0$ and $T_w = 970$ K for <i>iso</i> -octane at 500 Pa as obtained by the modified KUCRS mechanism. . . . .	123
4.3.10	Wall temperature at the cool flame, blue flame and hot flame positions of <i>n</i> -heptane at $\Phi = 1.0$ and pressures between 100 kPa and 500 kPa as obtained by the experiment and computations by the modified KUCRS mechanism. . . . .	127
4.3.11	Explosion limits of stoichiometric H <sub>2</sub> -O <sub>2</sub> mixture. . . . .	131
4.3.12	Comparison of the rate constants of R1932 and R1938 for different dilution conditions at 100 kPa as obtained by the modified KUCRS mechanism. . . . .	132
4.3.13	Heat contribution index of the cool flame, blue flame and hot flame of <i>iso</i> -octane at $\Phi = 1.0$ and $P = 500$ kPa for different diluents and dilution ratios as obtained by KUCRS. . . . .	134
4.3.14	Heat contribution index of the cool flame, blue flame and hot flame of <i>n</i> -heptane at $\Phi = 1.0$ and $P = 500$ kPa for different diluents and dilution ratios as obtained by KUCRS. . . . .	136
4.A.1	Comparison of experimental luminosity profile of <i>iso</i> -octane for a dilution ratio of 20% CO <sub>2</sub> at 200 kPa with computational results by LLNL. . . . .	142

4.A.2	Wall temperature at the blue flame (left side) and hot flame positions (right side) of <i>iso</i> -octane at pressures between 100 kPa and 500 kPa as obtained by the experiment and computations by the LLNL mechanism. .	143
4.A.3	Wall temperature at the cool flame (left side), blue flame (middle) and hot flame positions (right side) of <i>n</i> -heptane at pressures between 100 kPa and 500 kPa as obtained by the experiment and computations by the LLNL mechanism. . . . .	145



# List of Tables

1.1	Overview of chemical species in SIP gasoline surrogate fuels. . . . .	8
2.1	Experimental conditions. . . . .	29
2.2	Arrhenius parameters of KUCRS and FFCM of selected H-O reactions. . .	42
2.3	Enhanced third body efficiencies of KUCRS and FFCM for reaction K1938/L26.	43
2.4	Effect of individual reactions on the wall temperature at the hot flame location when Arrhenius parameters are changed from KUCRS to FFCM for PRF100 at $\Phi = 1.0$ and 0.5. . . . .	44
2.5	Species with highest mole fractions at hot flame locations of KUCRS, PRF100 at $\Phi = 1.0$ and 0.5. . . . .	45
3.1.1	RON of selected fuels. . . . .	73
4.2.1	Chemiluminescence reactions used to model CH* formation and quenching.	108



# Nomenclature

## Abbreviations

Symbol	Description	Unit
GC	Gas Chromatography	-
CFR	Cooperative Fuel Research	-
EGR	Exhaust Gas Recirculation	-
HC	Hydrocarbon	-
HCI	Heat Contribution Index	-
ICE	Internal Combustion Engine	-
IDT	Ignition Delay Time	-
JSR	Jet-Stirred Reactor	-
LTO	Low Temperature Oxidation	-
MFR	Micro Flow Reactor	-
MON	Motor Octane Number	-
NTC	Negative Temperature Coefficient	-
OI	Octane Index	-
PRF	Primary Reference Fuel	-

RCM	Rapid Compression Machine	-
RON	Research Octane Number	-
SIP	Strategic Innovation promotion Program	-
SI	Spark-Ignited	-
TRF	Toluene Reference Fuel	-
WF	Weak Flame	-

### Latin symbols

Symbol	Description	Unit
$A$	Area	$\text{m}^2$
CCR	Critical Compression Ratio	-
$c_p$	Constant pressure heat capacity	$\text{J}/(\text{kg K})$
$c_v$	Constant volume heat capacity	$\text{J}/(\text{kg K})$
FAI	Formaldehyde Index	-
$h$	Heat transfer coefficient	$\text{W}/(\text{m}^2 \text{K})$
HCI	Heat Contribution Index	-
HRR	Heat Release Rate	$\text{W}/\text{cm}^3$
$k$	Rate constant	$\text{mole}/\text{cm}^3/\text{s}$
$m$	Mass	kg
$n$	Mole number	-
$Nu$	Nusselt number	-
$\dot{Q}$	Heat transfer	W
$T$	Temperature	K



$x$	Location	cm
-----	----------	----

## Greek symbols

Symbol	Description	Unit
$\gamma$	Adiabatic index, $\frac{c_p}{c_v}$	-
$\epsilon$	Compression ratio	-
$\eta_{th}$	Thermal efficiency	-
$\lambda$	Air-fuel equivalence ratio	-
$\phi$	Fuel-air equivalence ratio	-

## Subscripts

Symbol	Description	Unit
CS	Cross Section	-
ox	Oxidizer	-
st	Stoichiometric	-
surf	Surface	-
w	Wall	-



# 1 Introduction

## 1.1 Background of this thesis

Currently, more than 1.3 billion cars and trucks are in use worldwide [1]. It is expected that this number will increase to more than two billion vehicles over the course of the next decades [2]. This vast amount of vehicles makes the transport sector currently responsible for approximately 20 % of global carbon dioxide (CO<sub>2</sub>) emissions [3, 4]. As CO<sub>2</sub> has a strong effect as a greenhouse gas and is among the causes of climate change, a further increase of vehicle numbers poses a severe problem. On the other hand, it is expected that fuel consumption per vehicle can be reduced by 50 % by the year 2035 as compared to 2005 [5, 6]. This reduction is based on various aspects, such as improved aerodynamics, improved power consumption of auxiliary components, such as lighting and air conditioning as well as reduced vehicle weight [4]. Furthermore, increased adaptation of alternative drive concepts such as hybrid and fully electric engines will decrease individual CO<sub>2</sub> emissions per vehicle. Fig. 1.1 shows the sales of light duty vehicles based on past numbers and future predictions. While the sales of conventional Internal Combustion Engines (ICE) are going to decline in the near future, sales of hybrid technologies that include ICEs are predicted to continue increasing until 2035. Gasoline-based systems are

## 1 Introduction

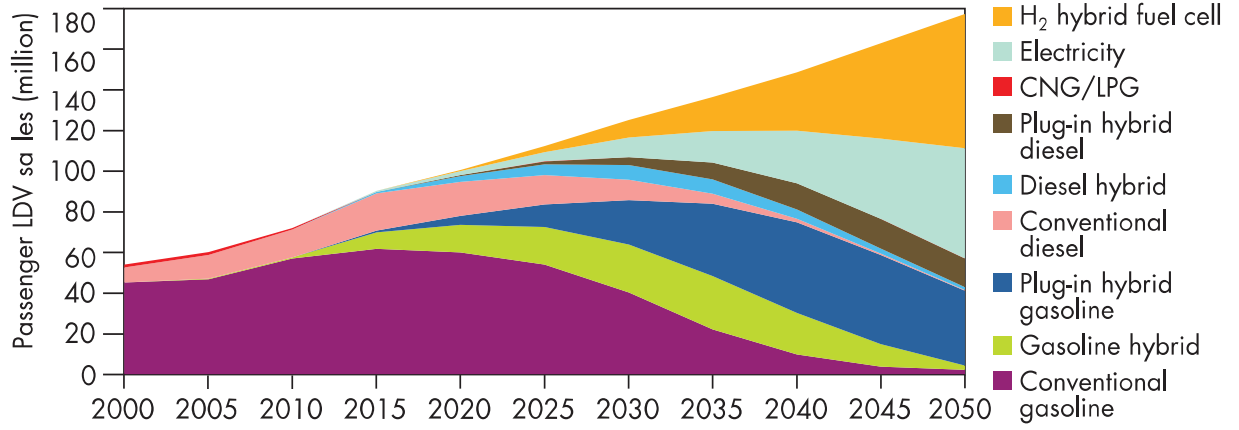


Figure 1.1: Evolution of global light duty vehicle sales by technology type [2].

expected to make up the largest part of these hybrid technologies. Therefore, optimization and improvement of gasoline engines is of great importance in order to decrease greenhouse gas and pollutants emissions from vehicles.

In addition to the aforementioned factors that decrease power consumption, the increase of the thermal efficiency  $\eta_{th}$  has a big impact on overall fuel consumption and emissions. Gasoline engines are based on the Otto cycle, whose ideal thermal efficiency is given by Eq. (1.1).

$$\eta_{th, ideal} = 1 - \frac{1}{\epsilon^{(\gamma-1)}} \quad (1.1)$$

In its ideal form, the thermal efficiency is only dependent on the compression ratio  $\epsilon$  and the heat capacity ratio  $\gamma$  of the compressed gas. In practical gasoline engines, however, additional losses occur that decrease the actual thermal efficiency. These losses include heat transfer between the gas-phase and the combustion chamber wall, non-instantaneous and incomplete combustion, exhaust blowdown losses due to early opening of exhaust valves as well as crevice effects and leakage [7]. Furthermore,  $\epsilon$  and  $\gamma$  cannot be increased at will. As  $\gamma$  of air is 1.4 and that of combustion products is often taken as a constant value between 1.25 and 1.3 [8], their effect on  $\eta_{th}$  is small. Consequently, an increasing

compression ratio has the biggest effect on the ideal thermal efficiency. The maximum achievable compression ratio in a Spark-Ignited (SI) gasoline engine, however, is limited by the occurrence of engine knock. Engine knock is the spontaneous auto-ignition of end-gas ahead of the flame front, which leads to a rapid pressure increase that can damage the engine. In order to avoid this phenomenon from occurring, the maximum compression ratio has to be limited below a critical compression ratio. Current gasoline engines are approaching thermal efficiencies of 40% [9, 10]. In order to further increase this value, the Japanese government introduced the Cross-Ministerial Strategic Innovation promotion Program (SIP) in 2014 [11]. As parts of the contents of this dissertation played a role in that effort, a brief overview of the SIP project will be given in the following part (section 1.2).

## 1.2 SIP project

The SIP program is a Japanese national program that was established under the Cabinet Office, Government of Japan. The SIP program consists of eleven different projects that cover many aspects of innovative technologies from material research to cyber security [12]. Among these, the innovative combustion technology project is a collaboration between the nine major Japanese car makers and more than 80 Japanese universities. It consists of four groups that are concerned with gasoline combustion, diesel combustion, loss reduction and general control, respectively. The target of the gasoline combustion group was to increase the thermal efficiency of SI gasoline engines to 50%, which was achieved in January 2019 (51.5%). The underlying approach of this development was to enable stable low temperature combustion. This was facilitated by several interconnected approaches.

## 1 Introduction

The main concept is super-lean combustion, i. e., combustion with excess air. This will be discussed in the following part (section 1.2.1).

### 1.2.1 Super-lean combustion

The balance of fuel and air can be expressed by the fuel-air equivalence ratio  $\Phi$ , which is shown in Eq. (1.2).

$$\Phi = \frac{m_{\text{fuel}}/m_{\text{ox}}}{(m_{\text{fuel}}/m_{\text{ox}})_{\text{st}}} = \frac{n_{\text{fuel}}/n_{\text{ox}}}{(n_{\text{fuel}}/n_{\text{ox}})_{\text{st}}} \quad (1.2)$$

The equivalence ratio is the ratio of the fuel-to-oxidizer ratio of the given mixture to the fuel-to-oxidizer ratio of a stoichiometric mixture. It can be expressed as mass ratios or as mole ratios. Lean mixtures have equivalence ratios of  $\Phi < 1.0$ , stoichiometric mixtures have  $\Phi = 1.0$  and rich mixtures have  $\Phi > 1.0$ . Another common measure is the air-fuel equivalence ratio  $\lambda$ , which is the inverse of  $\Phi$ .

As was shown in Eq. (1.1), the ideal thermal efficiency is dependent on the heat capacity ratio  $\gamma$ , where larger values of  $\gamma$  lead to higher efficiency. Air has a heat capacity ratio of  $\gamma = 1.4$ , which is larger than that of combustion products that is between 1.25 and 1.3 [8]. Therefore, as lean conditions contain larger amounts of air, this leads to higher average  $\gamma$ , which directly enables higher ideal efficiencies. Furthermore, lean conditions lead to a decrease of the combustion temperature, as less fuel has to heat a larger amount of air. This, in turn, decreases heat loss from the gas phase to the wall, as the heat loss is a direct function of the temperature difference (see Eq. 1.3). A schematic of this effect is shown in Fig. 1.2.

$$\dot{Q} = hA(T_{\text{gas}} - T_{\text{surf}}) \quad (1.3)$$

While the combustion at super-lean conditions may offer many benefits, it also poses

## ➤ Super-Lean burn

$$q(\theta) = h(\theta) \{T_g(\theta) - T_{surface}(\theta)\}$$

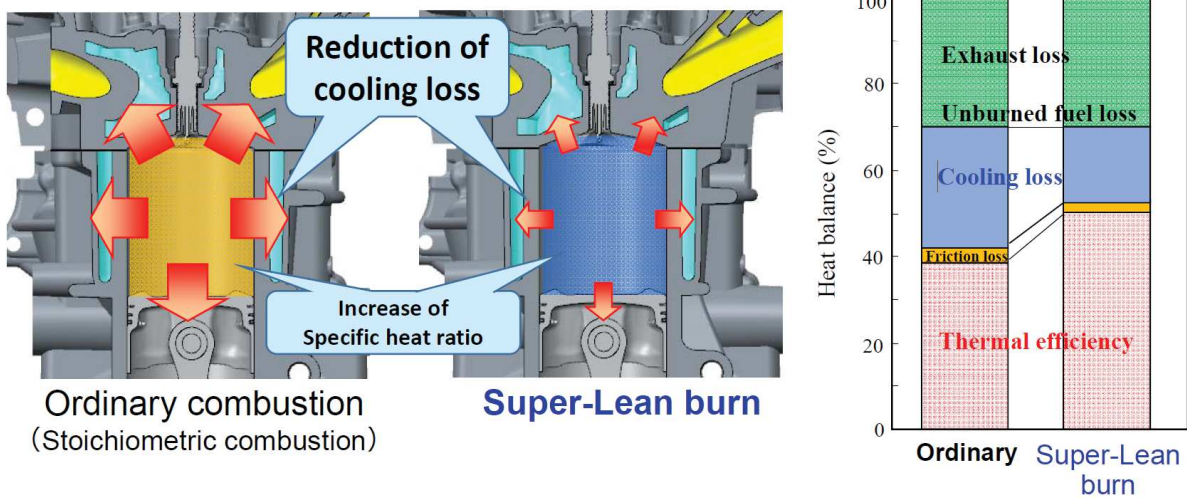


Figure 1.2: Schematic of super-lean burn concept for gasoline engines [13].

many challenges. The common combustion limit for lean conditions in actual engines is around  $\Phi = 0.7$  [14]. The goal of the SIP project, however, was to realize combustion at  $\Phi = 0.5$  (super-lean condition). In order to make combustion at this equivalence ratio feasible, several approaches were considered. For most hydrocarbons (HC), the laminar burning velocity decreases for decreasing  $\Phi$  below unity [15]. This also decreases the flame propagation speed at turbulent engine conditions. In order to counter this phenomenon, high intensity turbulent flows can be used to enhance the flame spread throughout the combustion chamber. This high intensity turbulence, however, has to be well controlled in order to not spread the flame too thinly, which might lead to extinction. Furthermore, super-lean conditions and high turbulence can cause lower ignitability by spark discharge. This, in turn, can be countered by more sophisticated ignition design. One proposed solution is the optimization of the fluid flow around the spark plug. This improves the development of the flame kernel, which is essential for ignition. The other part is strengthening the

## 1 Introduction

ignition itself. The approach in the SIP project for this problem was to increase the number of discharge coils to ten and to distribute their energy release over a longer time period. Additionally, a profound understanding of the chemical aspect of the ignition process is of great importance.

### 1.2.2 Exhaust gas recirculation

Even for super-lean conditions, engine knock is still the limiting factor for the maximum compression ratio. The usage of Exhaust Gas Recirculation (EGR) has been shown to decrease the propensity of engine knock. When EGR is used, portions of the exhaust gas are combined with fresh fuel/air mixture before combustion. There are three main effects of EGR, namely the thermal effect, the dilution effect and the chemical effect [16–19]. The thermal effect is controlled by large fractions of  $\text{CO}_2$  and  $\text{H}_2\text{O}$  in the recirculated gas, which have higher specific heat capacities than the pure fuel/air mixture. On the one hand, this leads to higher intake temperatures when the recirculated gas is not cooled [20]. On the other hand, this lowers the maximum combustion temperature as the recirculated gas can absorb more heat during combustion. The thermal effect is therefore important in controlling the formation of  $\text{NO}_x$ , as large amounts are produced through the thermal pathway [21]. At the same time, lower combustion temperatures also decrease the heat loss through the combustion chamber walls, which increases the thermal efficiency [22]. Furthermore, lower temperatures inside the chamber reduce the risk of engine knocking [23–25].

The dilution effect refers to lower concentrations of  $\text{O}_2$  and fuel in the combustion chamber by replacing parts of the fuel/air mixture with recirculated gas. The reduction of  $\text{O}_2$  concentration leads to longer Ignition Delay Times (IDTs) [20, 26, 27], while, at



the same time, concentrations of reactive species are reduced. The dilution effect is most prominent for fuels that show multi-stage ignition, such as *n*-heptane, while fuels that show single-stage ignition, such as *iso*-octane and ethanol are less affected [28].

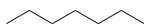
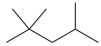
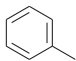
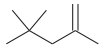
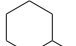
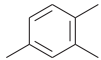
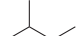

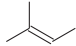
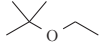
The third effect, the chemical effect, is mainly controlled by the concentration of CO<sub>2</sub> and H<sub>2</sub>O in the recirculated gas. In addition to the aforementioned higher specific heat capacity, these species play an important role in three-body reactions. As both species, in general, enhance three-body reactions, their addition leads to shorter ignition delay times [26, 28, 29]. This trend is in competition with the retarding thermal effect, which is caused by their higher specific heat capacity [30]. Furthermore, CO<sub>2</sub> has an inhibiting effect on the reaction  $\text{CO} + \text{OH} \rightleftharpoons \text{CO}_2 + \text{H}$ , which, in turn, slows down the important high-temperature chain branching reaction  $\text{H} + \text{O}_2 \rightleftharpoons \text{OH} + \text{O}$  and therefore decreases reactivity [31].

### 1.2.3 Gasoline surrogates

In order to increase the compression ratio without increasing the risk of engine knock, even when using methods that decrease the probability of engine knock, a profound knowledge of the reactivity of the fuel/air mixture is necessary. As gasoline is a complex fuel that consists of several hundred chemical species and as individual gasoline blends differ from each other, detailed investigation, especially computational, remains a challenging task. In order to simplify investigations, surrogate fuels have been developed that mimic certain physical and chemical properties by mixing two or more pure chemical species. These properties include density, viscosity and boiling point as well as ignition delay times and laminar flame speeds. The simplest gasoline surrogates are Primary Reference Fuels (PRF), which are mixtures of *n*-heptane, a fuel of high reactivity, and *iso*-octane, a

## 1 Introduction

Table 1.1: Overview of chemical species in SIP gasoline surrogate fuels.

Component	Structure	PRF90	PRF100	S3R	S5R	S5H	S10R	S10H
<i>n</i> -Heptane		10.0%	0.0%	21.1%	21.5%	10.0%	13.5%	1.0%
<i>iso</i> -Octane		90.0%	100%	33.0%	29.0%	31.0%	20.5%	11.0%
Toluene		-	-	46.0%	30.5%	40.0%	7.0%	29.0%
Diisobutylene		-	-	-	14.0%	14.0%	7.0%	7.0%
Methylcyclohexane		-	-	-	5.0%	5.0%	5.0%	5.0%
Trimethylbenzene		-	-	-	-	-	15.0%	15.0%
<i>iso</i> -Pentane		-	-	-	-	-	14.0%	14.0%
<i>n</i> -Pentane		-	-	-	-	-	8.0%	8.0%
2-Methyl-2-butene		-	-	-	-	-	7.0%	7.0%
Ethyl-tert-butyl-ether		-	-	-	-	-	3.0%	3.0%

fuel of low reactivity. Pure *n*-heptane is called PRF0, pure *iso*-octane is called PRF100 and mixtures of these two are denoted by the number that represents the volumetric fraction of *iso*-octane in the liquid mixture. These numbers also represent the Research Octane Number (RON) of each fuel, where lower numbers indicate higher reactivity (see section 1.3.2). When toluene is added to PRF, it is called Toluene Reference Fuel (TRF), which allows for better representation of the actual properties of gasoline. For the SIP project, additional surrogates with five species and ten species were developed. And overview of these surrogates is given in Tab. 1.1. Here, S stands for surrogate, the numbers 3, 5 or 10 represent the number of chemical components and R (regular) indicates a surrogate of RON = 90 while H (high-octane) indicates a surrogate of RON = 100.

The usage of these surrogates makes it easier to investigate ignition and combustion characteristics of fuels. The most common investigation methods for fuel reactivity will be presented in section 1.3.

### 1.2.4 KUCRS reaction mechanism

In addition to experimental investigations of fuel reactivity, simulations are a valuable addition as they allow for better understanding of underlying mechanisms such as chemical reactions. To this end, chemical reaction mechanisms haven been developed. Most reaction mechanisms for the combustion of hydrocarbons have a hierarchical order, e. g., the base is made of hydrogen-oxygen reactions, followed by C<sub>1</sub> reactions and then reactions of higher hydrocarbons. For gasoline and its surrogates, several reaction mechanisms have been developed. These include the Lawrence Livermore National Laboratory (LLNL) PRF mechanism [32], the LLNL gasoline surrogate mechanism [33] and the CRECK PRF mechanism [34], which are detailed reaction mechanisms as well as the CRECK gasoline surrogate mechanism [35–37], which is a reduced mechanism. While these mechanisms showed good results for simulations in motored engines, rapid compression machines and jet stirred reactors, they are only applicable for the selected fuel compositions. In case of the LLNL gasoline surrogate mechanism, this composition includes *n*-heptane, *iso*-octane, toluene and C<sub>5</sub>-C<sub>6</sub> olefins. However, as the gasoline surrogates of the SIP project cover a wider range of components, a more suited reaction mechanism was necessary.

The basis of the SIP reaction mechanism is KUCRS (Knowledge-basing Utilities for Complex Reaction Systems) [38]. This library uses the group additivity method [39], which estimates kinetic parameters based on analogy between chemical compounds. Special attention was paid to low temperature reactions, i. e., low temperature isomerization and

chain branching. To calculate rate parameters, quantum chemical methods were used. By using this approach, KUCRS can produce reaction mechanisms for complex mixtures, including the gasoline surrogates of the SIP project [40–44].

# 1.3 Common methods for the investigation of fuel reactivity

## 1.3.1 Shock tubes

A widely used method for the investigation of fuel reactivity is the shock tube. In general, it consists of a long tube that is divided into two closed-off sections by a diaphragm [45]. One chamber, the driver section, is filled with a gas, often helium, at high pressure. The other chamber, the driven sections, is filled with the reactive mixture that is to be investigated at lower pressure than that of the driver sections. When the diaphragm breaks, either from the pressure difference or an external impact, a shock wave travels through the driven section and is reflected on the opposite end. This results in a sharp increase of pressure and temperature in the test mixture, which leads to ignition. Often, the shock tube can be treated as a zero-dimensional system, which makes computations feasible [46]. The period of time that elapsed from the passing shock wave until ignition is called ignition delay time (IDT). It is a common measure for fuel reactivity, where fuels of higher reactivity show shorter IDTs. Shock tubes are mainly limited by the time in which constant conditions can be maintained, which is usually in the order of microseconds to several milliseconds [47, 48]. Typical IDTs and temperatures of shock tubes and rapid compression machines (see sections 1.3.2) are shown in Fig 1.3. In general, shock tubes

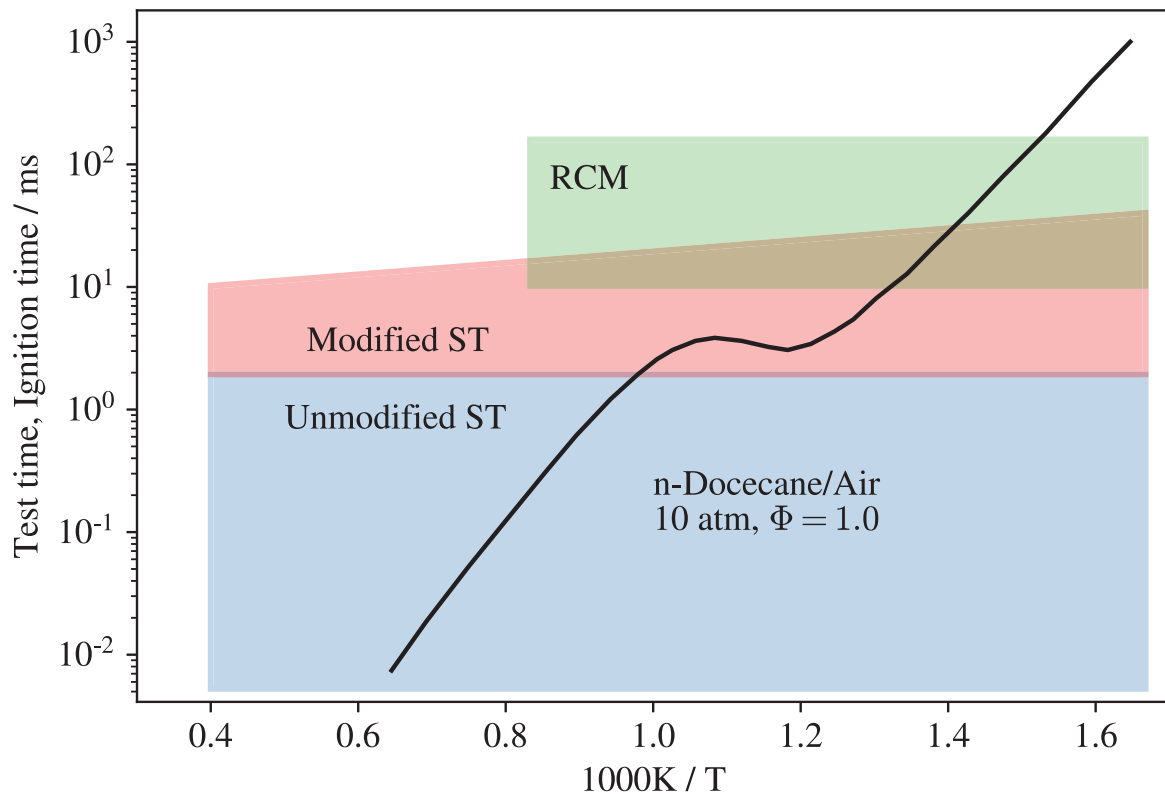


Figure 1.3: Typical operation regimes of shock tubes (ST) and rapid compression machines (RCM) [46].

show shorter IDTs than rapid compression machines and are therefore more commonly used at higher temperature and pressure conditions. By comparing experimental results and computations as well as by conducting species measurements, chemical reaction mechanisms can be validated and improved [49–51]. Species measurements are possible by techniques such as gas chromatography/mass spectrometry (GC/MS) [52] or optical methods [53, 54].

### 1.3.2 Rapid compression machines

As mentioned in section 1.3.1, Rapid Compression Machines (RCM) are another approach to measure IDTs. The aim of the RCM is to imitate a single compression stroke of a

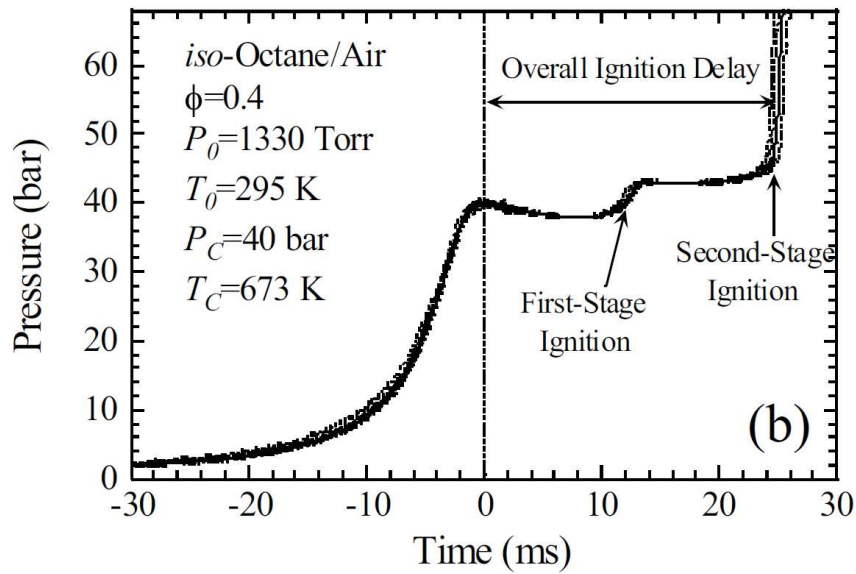


Figure 1.4: Two-stage ignition of *iso*-octane/air mixture [55].

reciprocating engine [55]. RCMs are able to investigate low to intermediate temperature regions, which partly overlap with those of shock tubes (see Fig. 2.16). These temperatures usually are within the range of 600 K to 1100 K. This makes it possible to observe two-stage ignition and Negative Temperature Coefficient (NTC) behavior [56]. Fig. 1.4 shows the two-stage ignition of an *iso*-octane/air mixture. The first stage ignition consists of reactions consuming the fuel that also lead to chain branching. The heat that is released by this Low Temperature Oxidation (LTO) leads to a temperature increase, which, in turn, shifts the balance away from chain branching to chain termination reactions. As the temperature further increases, high temperature chain branching reactions occur, which leads to the rapid pressure (and temperature) increase in Fig. 1.4. Similar to shock tubes, species and their time evolution can be measured [57, 58]. Due to their different temperature ranges, rapid compression machines and shock tubes can be used to complement each other's results.

### 1.3.3 Octane numbers

A widespread method to quantify fuel reactivity are the Research Octane Number (RON) [59] and the Motor Octane Number (MON) [60]. For their measurement, a single-cylinder Cooperative Fuel Research (CFR) engine at 600 rpm for RON or at 900 rpm for MON is used. For a given fuel, the compression ratio is varied until auto-ignition occurs. For this compression ratio, the PRF with the same critical compression ratio is determined. The percentage of *iso*-octane in this PRF corresponds to the RON or MON of test fuel, respectively. Therefore, a fuel that shows the same critical compression ratio as a mixture of 10 % *n*-heptane and 90 % *iso*-octane at 600 rpm is assigned a RON of 90. RON and MON can differ and the difference is called the fuel sensitivity (see. Eq. (1.4)) [61].

$$S = RON - MON \quad (1.4)$$

A more recent approach to octane numbers is the development of the Octane Index (OI) (see. Eq. (1.5)) [61].

$$OI = RON - KS \quad (1.5)$$

The OI was developed in order to describe fuel reactivity at more practical engine conditions, where  $K$  is an empirical factor that has to be determined experimentally.

## 1.4 Micro flow reactor with a controlled temperature profile

The Micro Flow Reactor with a controlled temperature profile (MFR) is a relatively recent investigation method [62, 63]. By the MFR-method, ignition characteristics of low and high reactivity fuels can be investigated at various conditions. The MFR was introduced

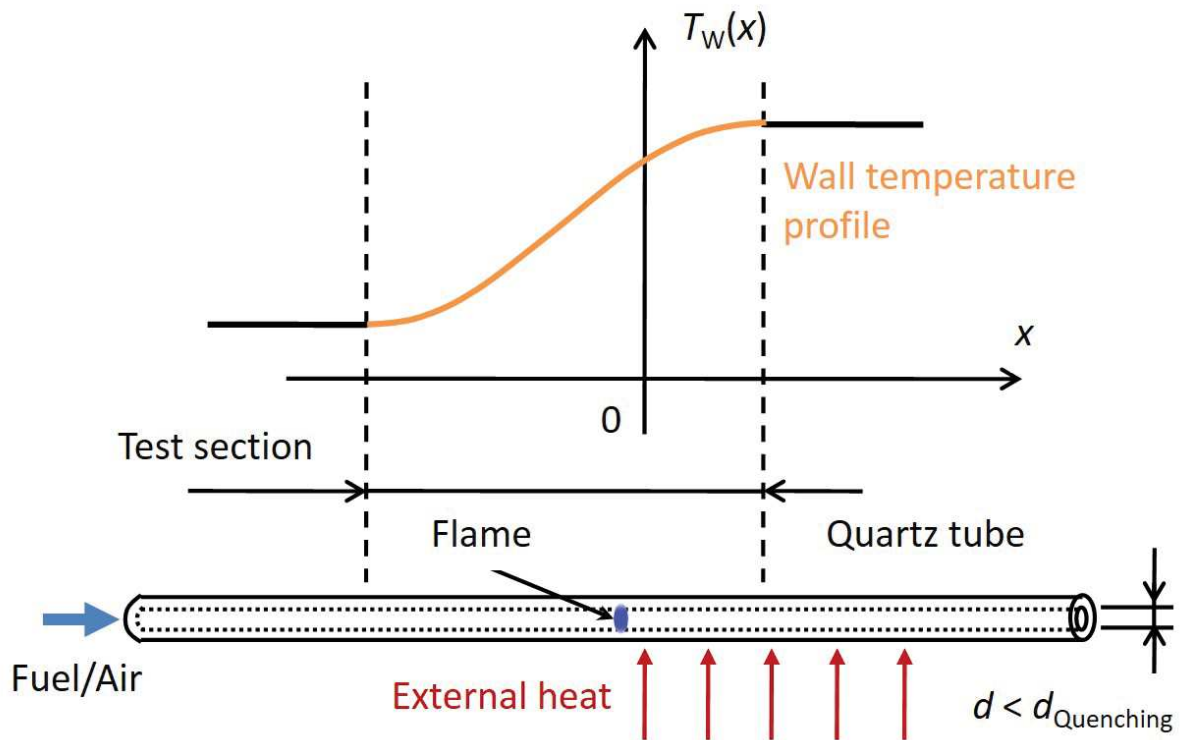


Figure 1.5: Schematic of the horizontal-type micro flow reactor with a controlled temperature profile [68].

by our group in 2005 and has since been used by other groups as well [64–67]. A scheme of the MFR (horizontal type) is given in Fig. 1.5. The MFR is made of a quartz tube whose inner diameter is smaller than the ordinary quenching diameter of the given fuel. This reactor channel is heated by an external heat source, which induces a stationary wall temperature profile along the axis of the quartz tube. The mixture of fuel and oxidizer is then supplied from the cool end of the tube. Inside the reactor channel, the flow is laminar and at constant pressure. With varying inlet flow velocity, three types of flame responses can be found. At high inlet flow velocities, a stable bright flame is observed. This so called *normal flame* represents flame propagation of a preheated mixture. As the flow velocity is reduced, an oscillating flame is seen. It is called *FREI* (Flame with



#### 1.4 Micro flow reactor with a controlled temperature profile

Repetitive Extinction and Ignition). The flame first ignites at the high temperature side of the reactor channel and propagates upstream to the lower temperature side, where it finally extinguishes. As the fresh mixture flows downstream again and reaches the region of higher temperature, it re-ignites and starts a new cycle. A third flame appears at very low flow velocities. This flame, again, is a stable flame but shows only low heat release and low luminosity. This flame was named *weak flame* [62]. Due to its low heat release, the gas-phase temperature is strongly controlled by the externally induced wall temperature. Temperature differences between the gas-phase and the wall are only significant at flame locations and even there, differences are less than 20 K [69]. As the surface-to-volume ratio is high, the effect of radical quenching on the flame location was investigated and it was shown to be negligible [64, 65, 70].

The flame locations of the normal flame and the weak flame as well as the ignition and extinction points of FREI for a stoichiometric methane/air mixture at 100 kPa for various mean inlet flow velocities are given in Fig. 1.6. Here, it can be seen that the locations of the normal flame are a continuation of the extinction points of FREI for higher flow velocities. The weak flame locations, on the other hand, are connected to the ignition points of FREI. Furthermore, the weak flame location practically does not change for changing inlet flow velocity. Based on theoretical considerations, the weak flame was found to be a stable solution of the Fendell curve and corresponds to the curve's ignition branch [63, 71]. This makes it possible to use weak flames for the investigation of ignition processes of fuels under a wide range of conditions.

An overview of stoichiometric weak flames at atmospheric pressure of several fuels with RON between 0 and 120 is given in Fig. 1.7. For fuels of high reactivity, the weak flame splits in up to three stationary, spatially-separated reaction zones. The zones were named

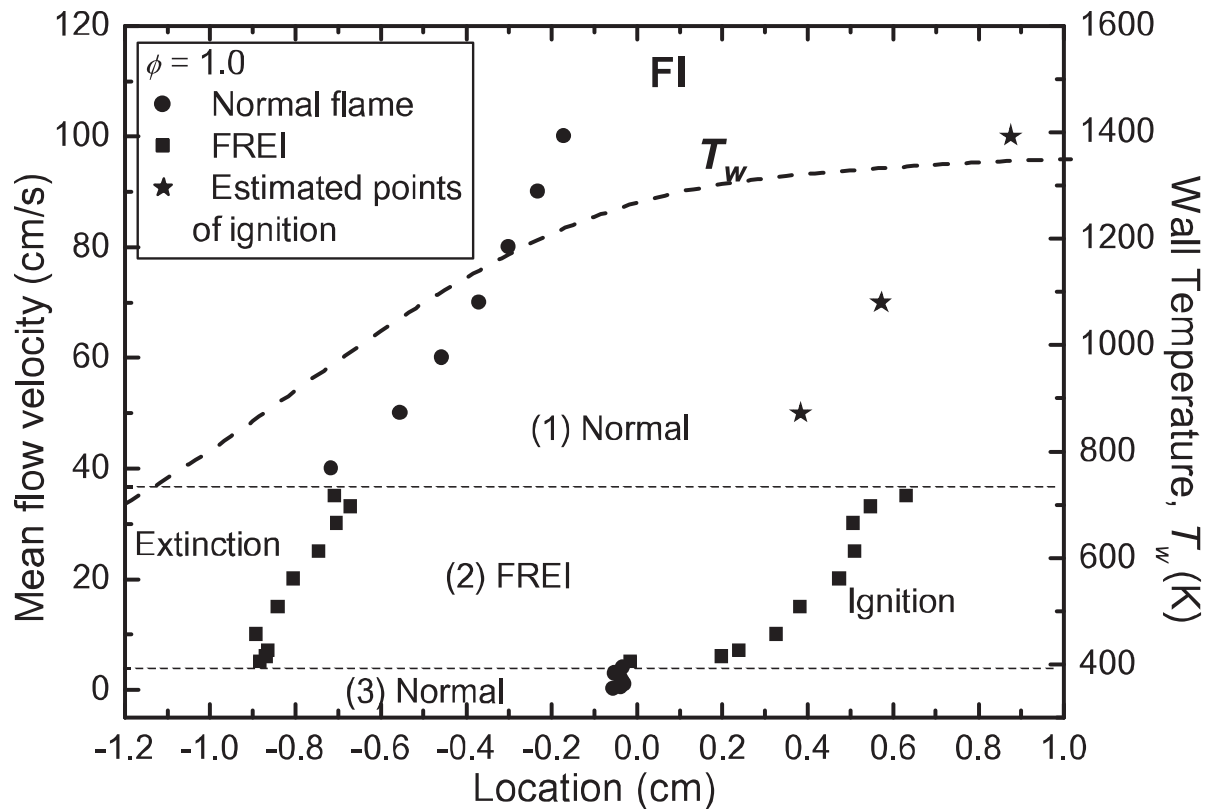


Figure 1.6: Measured positions of the normal flame ((1) Normal) and the weak flame ((3) Normal) as well as ignition and extinction points of FREI for a stoichiometric methane/air mixtures at 100 kPa and various mean inlet flow velocities [69].

cool flame, blue flame and hot flame, from low to high temperature, respectively. In Fig. 1.7, this can be seen for pure *n*-heptane (RON = 0) as well as PRF20 (RON = 20). The cool flame is the region of low temperature oxidization, where fuel is consumed and intermediate species such as hydrogen peroxide ( $\text{H}_2\text{O}_2$ ) and formaldehyde ( $\text{CH}_2\text{O}$ ) are formed. In the blue flame,  $\text{H}_2\text{O}_2$  dissociates in a chain branching reaction and produces two OH radicals. This enhances the consumption of the remaining fuel and intermediate species. Another important reaction is the consumption of  $\text{CH}_2\text{O}$  to form CO. The final stage of combustion is the hot flame, in which hydrogen-oxygen reactions dominate and where the oxidation of CO to the final combustion product  $\text{CO}_2$  takes place. Fuels of lower

#### 1.4 Micro flow reactor with a controlled temperature profile

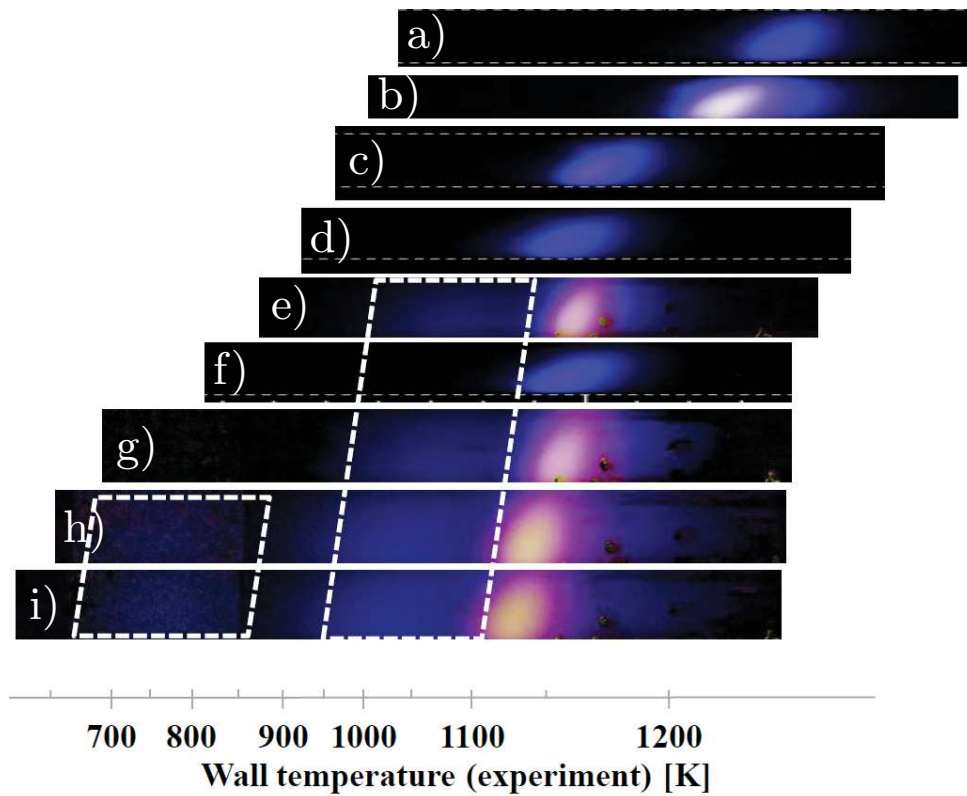


Figure 1.7: Influence of RON on flame appearance and position at  $P = 100$  kPa and  $\Phi = 1.0$ . Flame regions from left to right: cool flame, blue flame, (bright) hot flame. a) Methane (RON = 120), b) Toluene (120), c) Propane (112), d) Ethane (108), e) *iso*-Octane/PRF100 (100), f) *n*-Butane (94), g) PRF50 (50), h) PRF20 (20), and i) *n*-Heptane/PRF0 (0). Experimental conditions differ slightly. Data obtained from [72–75].

reactivity, such as PRF50 (RON = 50) and *iso*-octane (RON = 100), do not exhibit the cool flame but only the blue flame and the hot flame. For fuels of even lesser reactivity, e. g., toluene (RON = 120) and methane (RON = 120), only the hot flame remains. This single flame corresponds to the weak flame that was discovered in the original MFR paper [62]. From these results, it can be seen that the flame pattern and flame location are connected to the fuel reactivity. As fuel reactivity becomes less, i. e., as the RON increases, all three flames shift to higher temperatures and first the cool flame and then

## 1 Introduction

the blue flame disappear. These results show that the fuel reactivity has a strong impact on the weak flames characteristics in the MFR.

In addition to the aforementioned fuels, various other fuels have been investigated that include syngas [76], butane [75], DME [77], lower alkenes [78], ethanol [68], TRF [74] and diesel surrogates [79]. Most of these fuels were investigated at atmospheric pressure and at stoichiometry.

The effect of the equivalence ratio was tested for methane/air mixtures, where lean conditions moved the hot flame to lower wall temperatures [80]. Dilution of stoichiometric syngas/air mixtures by  $N_2$  did not show any effect on the hot flame, while dilution by  $CO_2$  and  $H_2O$  moved the flame to higher wall temperatures [76]. This effect is shown in Fig. 1.8.

The effect of pressure was investigated for PRF mixtures [73], ethanol [68] and *n*-butane [75]. Experimental images of *n*-butane/air weak flames at elevated pressure are shown in Fig. 1.9. It was found that elevated pressure shifted all the reaction zones to regions of lower wall temperature. Along with this shift, the heat release and relative luminosity of the cool flame and blue flame increased.

A study by another group used the MFR to investigate the transient FREI [67]. It found that the FREI of fuels with lower RON ignited and extinguished at lower wall temperatures than those of fuels with higher RON. These findings agree well with the results obtained by weak flames.

1.4 Micro flow reactor with a controlled temperature profile

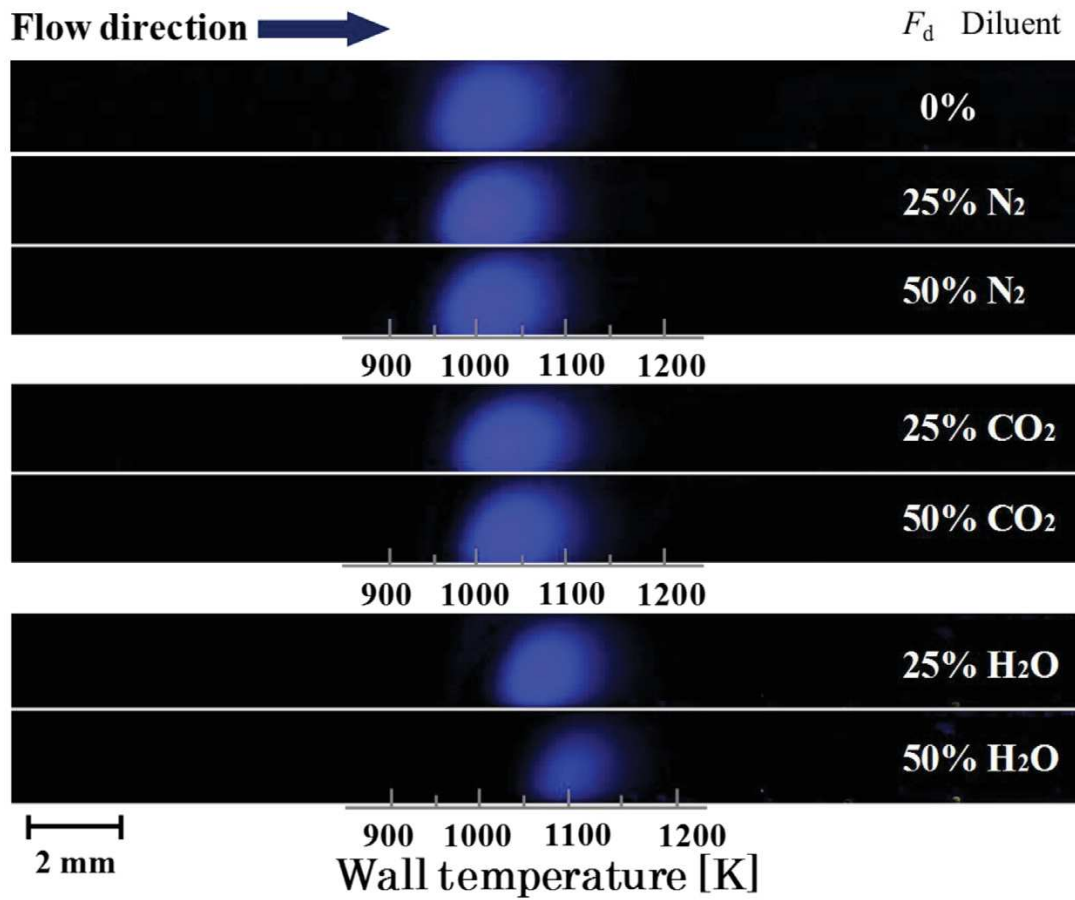


Figure 1.8: Effect of N<sub>2</sub>, CO<sub>2</sub> and H<sub>2</sub>O on the hot flame of stoichiometric syngas/air mixtures at 100 kPa [76].

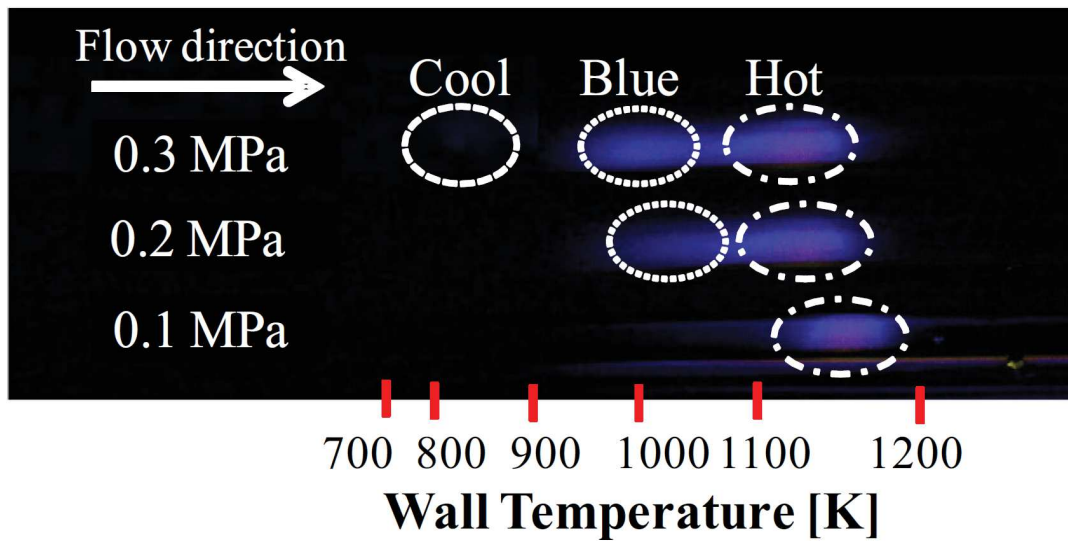


Figure 1.9: Weak flame images of stoichiometric *n*-butane/air mixture between 0.1 MPa and 0.3 MPa [75].

## 1.5 Objectives and outline of this thesis

Previous studies have shown that weak flames in the MFR can be used to qualitatively evaluate fuel reactivity. The purpose of this dissertation is to quantify these results and develop an index number that describes fuel reactivity. In order to achieve this, the main goals of this thesis are:

- Utilize a newly-developed vertical-type MFR to increase spatial resolution and accuracy of results
- Evaluate the applicability of existing reaction mechanisms for the given conditions
- Develop a reactivity index number that is applicable over a wide range of conditions, including ultra-lean, elevated pressure and EGR conditions

The structure of this dissertation is comprised of five chapters. The first chapter is the introduction and covers the background, an introduction to the MFR and weak flames as well as previous research.

The second chapter explores the effect of RON and equivalence ratio on the weak flames of PRFs. The equivalence ratio was varied between  $\Phi = 0.5$  and 1.0, while the RON was between 80 and 100. It was found that the KUCRS mechanism does not give accurate results for ultra-lean conditions. Therefore, parts of its hydrogen-oxygen reactions were modified. These changes lead to very good agreement between the experiment and the simulations.

The third chapter is the main part of this thesis and presents the development of the reactivity index, the Heat Contribution Index (HCI). Here, elevated pressure was used as this is closer to practical conditions. By investigating various fuels of different reactivity

## *1.5 Objectives and outline of this thesis*

and molecular structure, a relation between these two was found that can be expressed by the Blue flame-HCI.

In the fourth chapter, the effect of exhaust gas recirculation was investigated for PRFs. A new method for the comparison of flame locations was developed. Furthermore, the heat contribution index was used to evaluate the effect of diluents on the reactivity of the investigated fuels.

The fifth chapter is made up of the general conclusions of this dissertation and an outlook to future research.





# 2 Evaluation of the reactivity of ultra-lean PRF/air mixtures by weak flames in a micro flow reactor with a controlled temperature profile

## 2.1 Introduction

As was explained in section 1.2.1, ultra-lean combustion of gasoline has high potential for increasing thermal efficiency [81]. However, well-controlled ignition and stable combustion under those conditions are not well understood yet. This is a major problem for the application in commercial engines. As gasoline is a complex mixture of several hundred components, research is often conducted by Primary Reference Fuels (PRF), which are mixtures of *n*-heptane and *iso*-octane.

To investigate the effect of lean combustion on the reactivity of PRFs, past researches focused on shock tubes [33, 82–87], Rapid Compression Machines (RCM) [33, 84, 86] and Jet-Stirred Reactors (JSR) [32, 88]. By using shock tubes, ignition delay times (IDTs)

## 2 Evaluation of the reactivity of ultra-lean PRF/air mixtures by weak flames

were investigated at elevated temperatures. For pressures in the range of 1 MPa, a decrease of the equivalence ratio led to lower IDTs. This indicated higher reactivity for leaner conditions [84]. At higher pressures and decreasing equivalence ratio, shock tubes [82, 84] as well as RCMs [89, 90] showed longer IDTs, again hinting at lower reactivity.

In a previous study by our group, the micro flow reactor with a controlled temperature profile (MFR) was used to evaluate the effect of the Research Octane Number (RON) on PRF reactivity by weak flames [73]. As was explained in section 1.4, the MFR consists of a quartz tube with a small inner diameter, which is externally heated. At low inlet flow velocities, stable weak flames can be found, which correspond to the ignition branch of the Fendell curve. This allows for the usage of weak flames to investigate the ignition process and the reactivity of fuel/air mixtures. Figure 2.1 shows the images of weak flames of various PRFs at atmospheric pressure and stoichiometry. The fuels of RON between 20 and 100 showed hot flames at regions of high wall temperature and blue flames at intermediate wall temperatures. With decreasing RON, the hot flames and the blue flames shifted to lower wall temperatures. The cool flame only appeared for RON equal to or less than 20. This signifies strong Low Temperature Oxidation (LTO). These results showed a strong correlation between changing RON and the weak flame response.

Another study investigated the effect of the equivalence ratio on ultra-lean methane/air weak flames. This study found that as the equivalence ratio was decreased, the hot flames shifted to regions of lower wall temperature [80]. This is a trend that is similar to decreasing RON, which indicated higher reactivity.

Based on the results for changing RON and changing  $\Phi$ , the objective of this chapter is to evaluate the reactivity of ultra-lean PRF/air mixtures ( $\Phi = 0.5, 0.75, 1.0$ ) by separated weak flames in a MFR. PRF80, PRF90 and PRF100 were chosen as fuels as they have

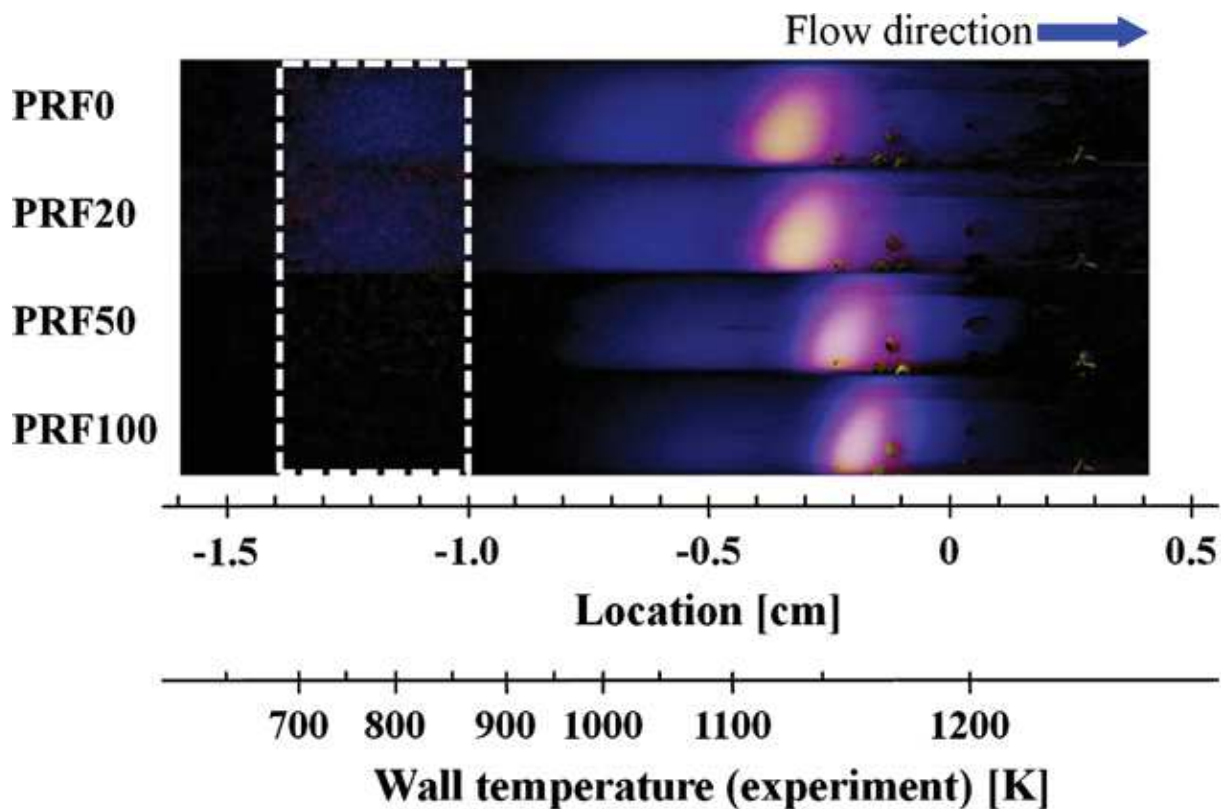


Figure 2.1: Influence of RON on flame patterns and positions at  $\Phi = 1.0$ ,  $P = 100$  kPa, horizontal-type MFR [73]. Flame regions from left to right: cool flame, blue flame and hot flame.

RONs that are in the range of actual gasoline. As the differences in flame locations for the given conditions were expected to be relatively small when using the horizontal-type MFR, a new vertical-type MFR was employed. The vertical-type MFR has a broad temperature profile that leads to a high resolution with regard to location and temperature. This allows for higher precision in the distinction of different weak flame responses. The pressure was set to 100 kPa. Additionally, simulations were conducted by the Lawrence Livermore National Laboratory (LLNL) PRF reaction mechanism [32] as well as by the KUCRS PRF reaction mechanism [38]. These results can be used to examine chemical reactions in more detail and to assess the capabilities of the reaction mechanisms.

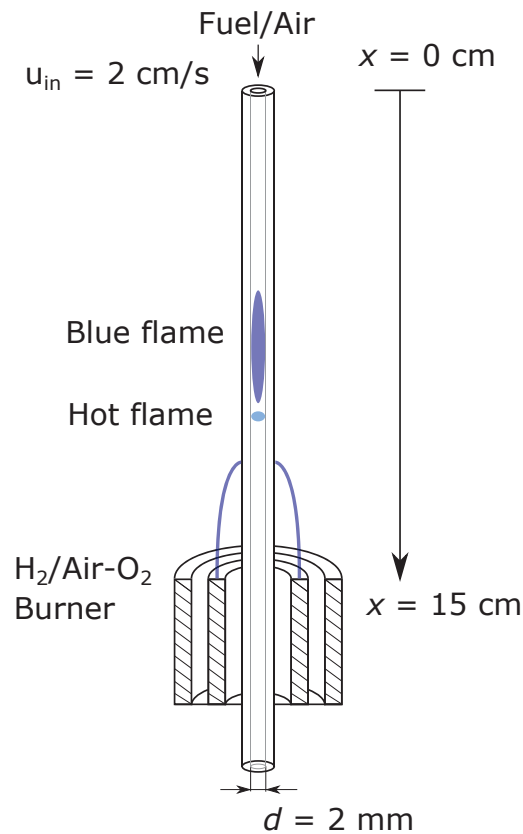


Figure 2.2: Scheme of the vertical-type micro flow reactor with a controlled temperature profile.

## 2.2 Methods

### 2.2.1 Experimental method

A vertical-type MFR was developed for this study with the goal of increasing the spatial resolution of the separated weak flames (see Figure 2.2). The vertical-type MFR contains a quartz tube with an inner diameter of 2 mm and a length of 15 cm. A coaxial non-premixed  $\text{H}_2/\text{O}_2$ -enriched-air burner was used as the external heat source at the lower end, leading to a mildly increasing temperature profile between the ends of the quartz tube. This increases the experimental temperature resolution as compared to the horizontal type, which was employed in previous studies [72, 77, 78]. The coaxial burner leads to an

axisymmetric temperature profile around the center axis. The temperature measurement of the tube's inner wall was conducted by a sheathed K-type thermocouple of 300  $\mu\text{m}$  diameter. The thermocouple was introduced from the lower end of the tube and measurements were conducted in the beginning and in the end of the experiments. In previous tests, measurement differences between sheath-type thermocouples with diameters of 320  $\mu\text{m}$  and 160  $\mu\text{m}$  and bare wires with diameters of 50  $\mu\text{m}$  were compared. For the temperature range of interest in this study, i. e., temperatures below 1200 K, no significant differences between the various thermocouple types were found. Therefore, the 300  $\mu\text{m}$  thermocouple was chosen as it achieves good accuracy while ensuring easy handling. When measuring the inner wall temperature, the thermocouple was in constant contact with the surface of the wall. The tip of the thermocouple was kept at each measurement point for up to five minutes. From this measurement, the average temperature as well as its temporal fluctuation were obtained (for details see appendix 2.B). The measurement location was obtained from digital image processing, where the spatial uncertainty was within 100  $\mu\text{m}$ . Figure 2.3 shows the measured wall temperature profile along the axis as well as its fluctuation. The minimum and maximum wall temperatures were set to 373 K and 1300 K, respectively. The standard deviation of the measured temperatures between 1000 K and 1100 K, i. e., the temperature range for hot flames, was within 3 K. Based on this temperature profile, a quadratic equation was fitted (see Eq. (2.1)) that was later used in the simulations. The flow of the mixture through the tube was considered to be laminar and at a pressure of 100 kPa.

$$T(x) = \frac{3.46 \text{ K}}{\text{cm}^2}x^2 + \frac{18.16 \text{ K}}{\text{cm}}x + 350.18 \text{ K} \quad (2.1)$$

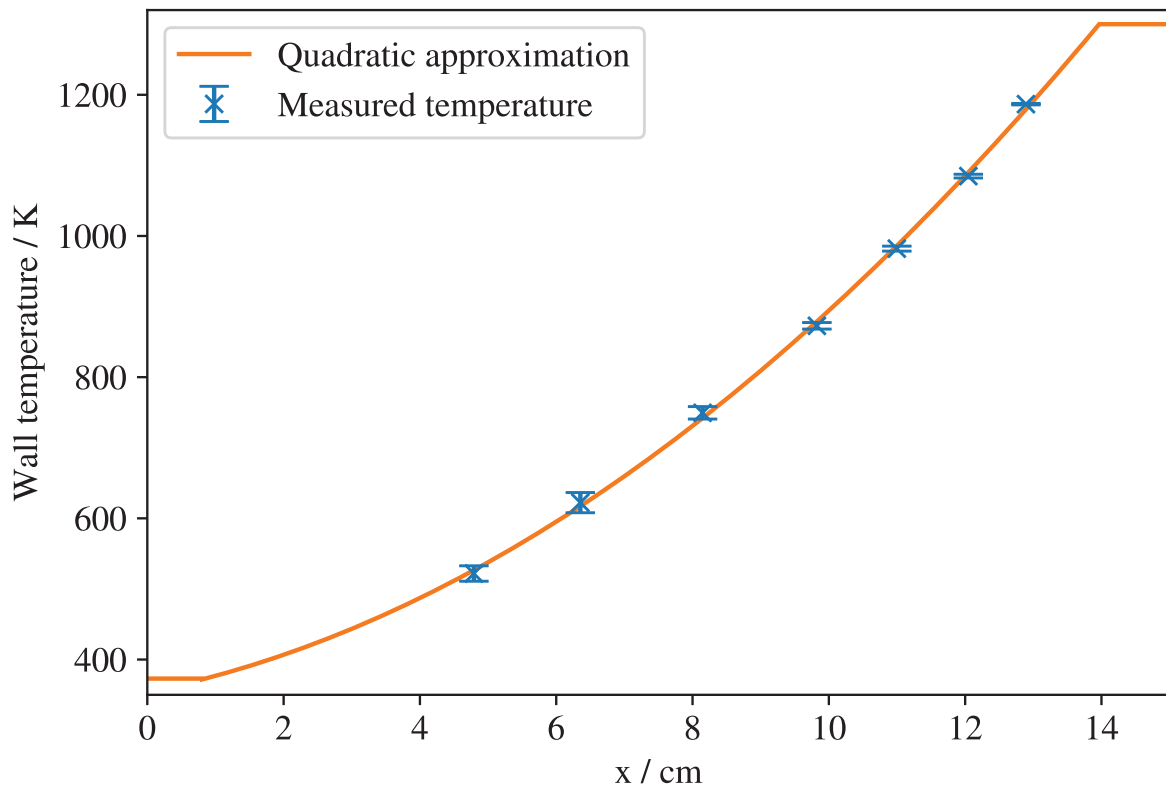


Figure 2.3: Experimentally measured wall temperatures and fitted quadratic approximation between 373 K and 1300 K.

An electrically heated tank, whose inside was vacuumed, was used to vaporize the liquid fuels (373 K at pressures less than 0.25 kPa). The liquid fuels were inserted into the tank by a syringe. After waiting several minutes for complete evaporation, nitrogen was added to the tank by the partial pressure method. To assure a uniform mixture, the contents were held in the tank for up to one hour. After this time, a heated mass flow controller was used to control the flow of the mixture from the tank to the upper end of the MFR. The mixture was sent through a heated pipe of 373 K, which prevented condensation of the fuel. Another mass flow controller was used to feed oxygen into the fuel/nitrogen mixture. The flow rate was chosen according to the  $O_2/N_2$  ratio of air and the chosen equivalence ratio. As weak flames appear only for low flow velocities, the inlet flow velocity into the MFR was

Table 2.1: Experimental conditions.

Parameter	Value
Fuels	PRF100, 90, 80
<i>iso</i> -octane/ <i>n</i> -heptane ratio	100:0, 90:10, 80:20
Research octane number (RON)	100, 90, 80
Equivalence ratio $\Phi$	1.0, 0.75, 0.5
Pressure	100 kPa
MFR length	15.0 cm
Inner diameter	2.0 mm
Temperature range	373 K to 1300 K
Inlet velocity	2 cm/s (at 373 K)

set to 2 cm/s at 373 K. Previous studies showed good agreement between locations of peak CH chemiluminescence in the experiments and the peaks of the heat release rate in the simulations [69, 73, 77, 91]. Consequently, a CH band-pass filter (transparent wavelength 432.3 nm, half-band width 6.4 nm) was used to take weak flame images by a Nikon D800 digital still camera. The exposure time was set to 100 s. In order to obtain better images of the flames, five images were averaged for every condition. In a second step, background subtraction was conducted, which led to clearer images of the flames. The hot flame location was obtained by the point of maximum luminosity. The wall temperature at this location was then calculated by Eq. 2.1. The experimental conditions are shown in Table 2.1.

## 2.2.2 Computational method

Simulations of the separated weak flames were conducted by modified Chemkin-Pro PREMIX [92]. Here, the MFR was modeled as a one-dimensional system with steady state reactive flow without boundary layer. Due to the low volume to surface ratio, the MFR shows strong heat transfer between the inner gas-phase and the reactor wall. To implement this heat transfer into the simulations, the energy equation was expanded by an additional term (see Eq. 2.2). Here,  $T_w$  and  $T$  are the wall temperature of the quartz tube and the temperature of the gas-phase, respectively. The value of the Nusselt number  $Nu$  was set to 4.0 [77]. These changes were made as part of a user-defined subroutine [62].

$$\begin{aligned} \dot{M} \frac{dT}{dx} - \frac{1}{c_p} \frac{d}{dx} \left( \lambda A \frac{dT}{dx} \right) + \frac{A}{c_p} \sum_{k=1}^K \rho Y_k V_k c_{p,k} \frac{dT}{dx} \\ + \frac{A}{c_p} \sum_{k=1}^K \dot{\omega}_k h_k W_k - \frac{A}{c_p} \frac{4\lambda Nu}{d^2} (T_w - T) = 0 \end{aligned} \quad (2.2)$$

The wall temperature  $T_w$  was modeled after the quadratic function that was taken from the experiment (see Figure 2.3).

The length of the computational domain was chosen as 15.0 cm. Adaptive grid spacing led to a minimum gridsize inside the hot flame of 50  $\mu\text{m}$ . The flow velocity at the inlet of the tube was set to 2.0 cm/s at 100 kPa and 373 K, according to the experiment. In order to model the chemical reactions, two detailed reaction mechanisms were used. The LLNL PRF mechanism [32] was chosen, as it is a well established reaction mechanism for PRF. It consists of 1034 species and 4206 reactions. Furthermore, the KUCRS PRF mechanism [38] was employed. This mechanism is the basis for the SIP project and mechanisms for gasoline surrogate fuels are built upon it [40]. It has 778 species and 2181 reactions. In the simulations, the hot flame location was obtained by finding the peak of the heat release rate.



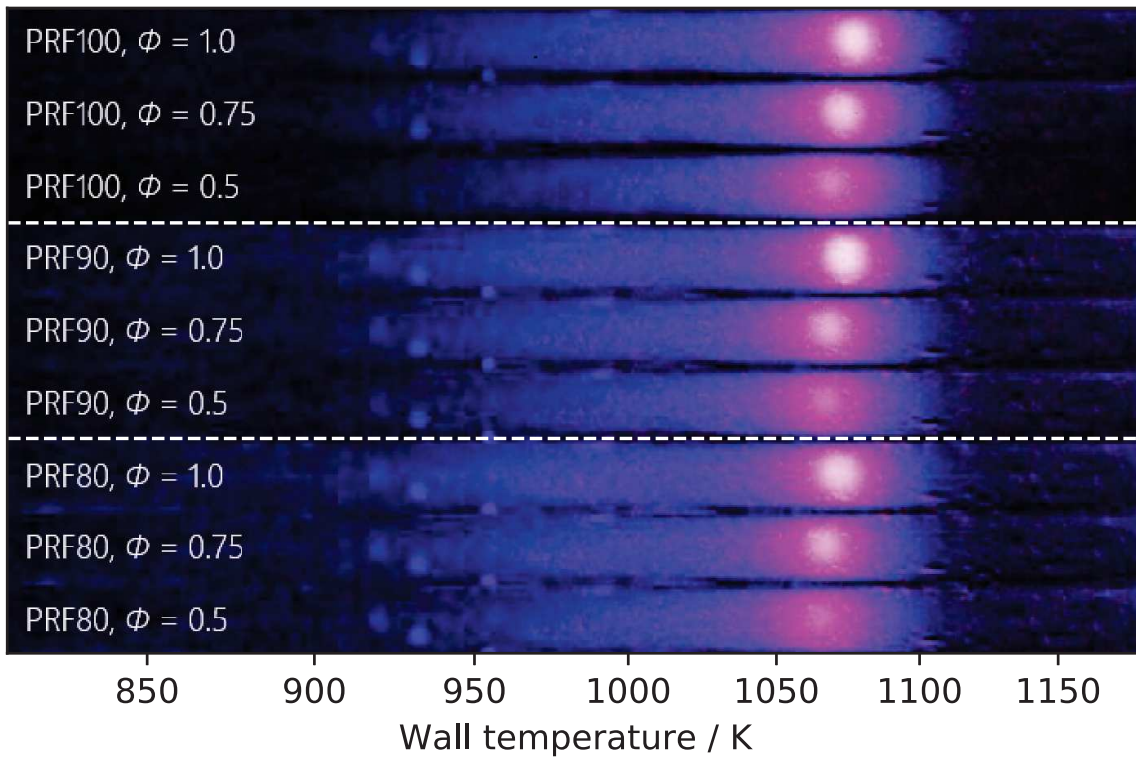


Figure 2.4: Experimental weak flame images of all nine cases. Flow direction from left to right.

## 2.3 Results and discussion

### 2.3.1 Flame locations and temperatures

Figure 2.4 shows the weak flame images of the experiment for PRF80, PRF90 and PRF100 at equivalence ratios of  $\Phi = 1.0$ , 0.75 and 0.5. The flow direction in the images is from left to right. On the right side of the images, bright circular spots are visible. These spots are the hot flames, which are located between wall temperatures of 1050 K (PRF80,  $\Phi = 0.5$ ) and 1070 K (PRF100,  $\Phi = 1.0$ ). To their left, at wall temperatures between 900 K and 1050 K, stretched blue zones can be seen. These are the blue flames. By lowering the RON from 100 (PRF100) to 80 (PRF80), the positions of the hot flames moved upstream,

## 2 Evaluation of the reactivity of ultra-lean PRF/air mixtures by weak flames

i. e., to lower wall temperatures. For a decrease of RON by 10, the flames moved to lower wall temperatures by 3 K. As the equivalence ratio was decreased, a similar effect was observed. For a decrease of the equivalence ratio by 0.25, the hot flames moved by 4 K to lower wall temperatures. For both cases, the shift to lower wall temperatures implies higher reactivity under these conditions. Furthermore, when the equivalence ratio was decreased, the intensity of the hot flame became weaker. This is a direct result of lower influx of fuel into the reactor channel at lower  $\Phi$ .

Figure 2.5 shows the Heat Release Rate (HRR) profiles as obtained by the LLNL and KUCRS mechanisms for PRF100 at  $\Phi = 1.0, 0.75$  and  $0.5$ . For both mechanisms, two regions of low and high HRR exist. The broad region between 850 K and 1050 K corresponds to the blue flame, while the peaks between 1050 K and 1100 K represent the hot flame. As the equivalence ratio was decreased, both mechanisms showed an overall decrease of the HRR. This is again caused by the overall reduction of fuel in the system and agrees with the experiment. As for the shift of the hot flame for changing equivalence ratio, however, differences exist between the two mechanisms. In case of the LLNL mechanism, decreasing equivalence ratio shifted the peak of the HRR to lower wall temperatures. The shift was from 1079 K at  $\Phi = 1.0$  to 1071 K at  $\Phi = 0.5$ . This shift indicates higher reactivity at lean condition, which agrees well with the experimental trend. For the KUCRS mechanism, however, the hot flame shifted to the opposite direction. As the equivalence ratio was decreased from  $\Phi = 1.0$  to  $0.5$ , the peak of the HRR shifted from 1066 K to 1080 K. As the hot flame moved to higher wall temperatures, it indicates lower reactivity. This trend is opposite to that of the experiment and that by the LLNL mechanism.

Figure 2.6 shows the wall temperatures at the experimental and computational location

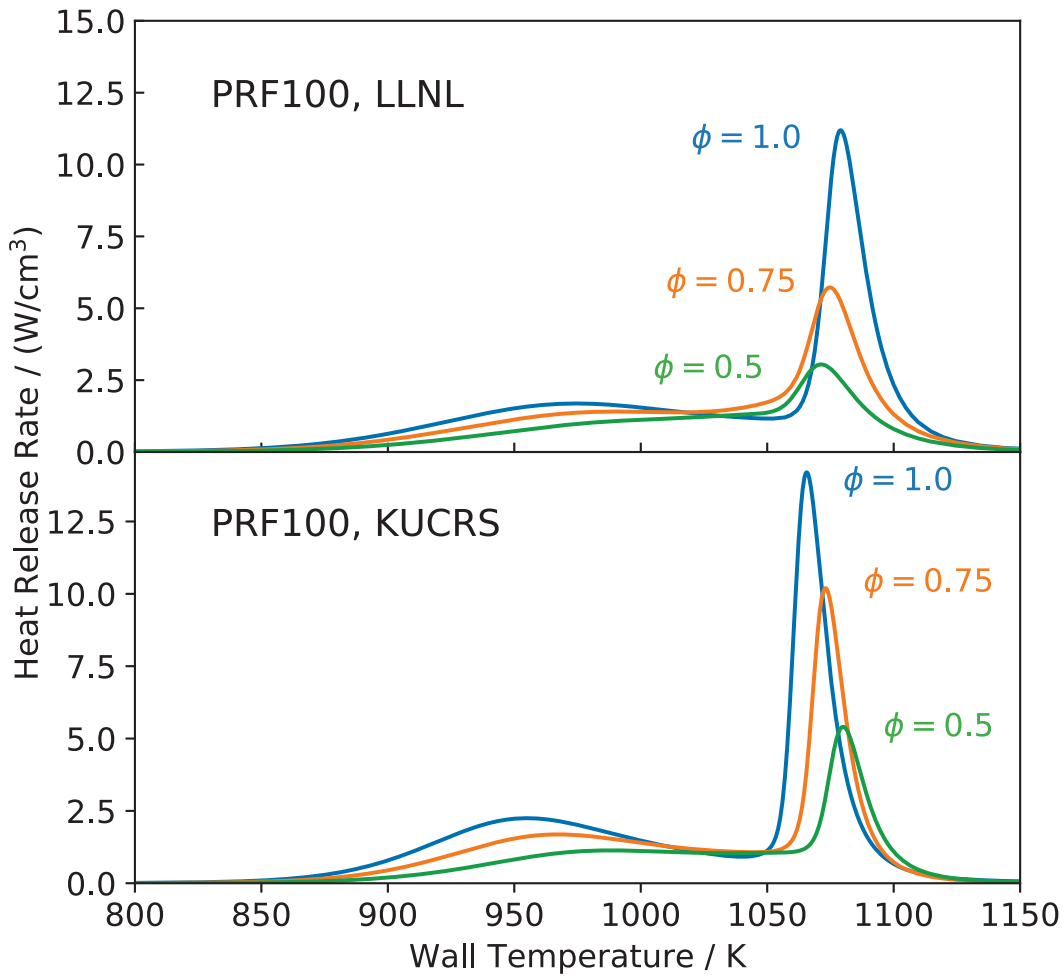


Figure 2.5: Heat release rates of PRF100 with LLNL and KUCRS at  $\Phi = 1.0, 0.75$  and  $0.5$  and  $P = 100$  kPa.

of the hot flames for all considered conditions. The trends of PRF80 and PRF90 are the same as those of PRF100 in both the experiments and computations. As  $\Phi$  was decreased, the luminosity peaks in the experiment moved to lower wall temperatures. In the simulations, the HRR peaks of the LLNL mechanism also moved to lower wall temperatures while those of the KUCRS mechanisms moved to higher wall temperatures. The hot flame locations of PRF80 and PRF90 by the LLNL and KUCRS mechanisms are located at lower wall temperatures than those of PRF100, which agrees well with the experiment. The hot flames moved upstream by about 3 K per  $\Delta\text{RON} = 10$ , which again

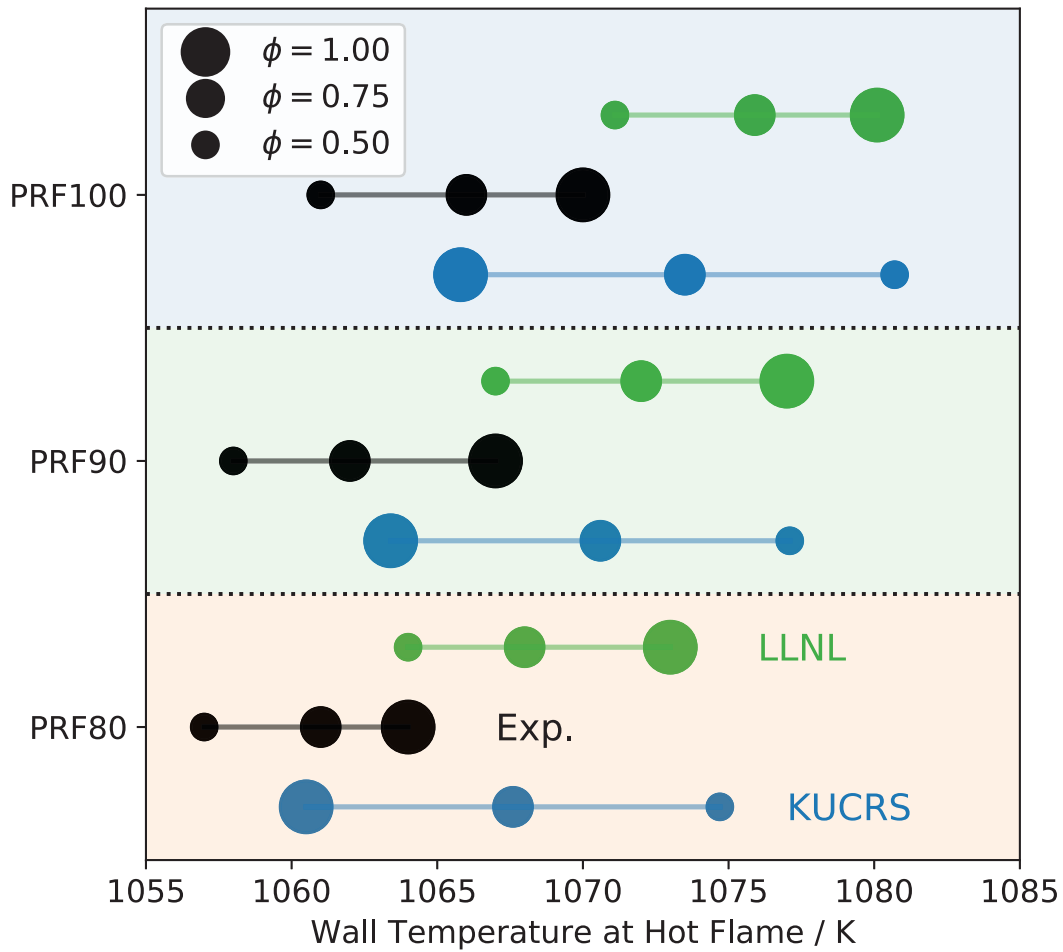


Figure 2.6: Wall temperature at hot flame location for all investigated cases ( $P = 100$  kPa), experiments and simulations.

is in very good agreement with the experiment. A similar trend for changing RON was found in a previous study for stoichiometric PRF/air mixtures [73]. That study, however, used a horizontal-type MFR, whose resolution with regard to the wall temperature was approximately 5 K. This only allowed for the differentiation of larger differences of RON. The usage of the vertical-type MFR in this study, on the other hand, allows for a much finer resolution that can detect changes for differences in RON of 10.

Fig. 2.7 shows the mole fraction profiles of important chemical species as obtained by the LLNL mechanism for PRF100 and  $\Phi = 1.0$ . These species profiles can be used to

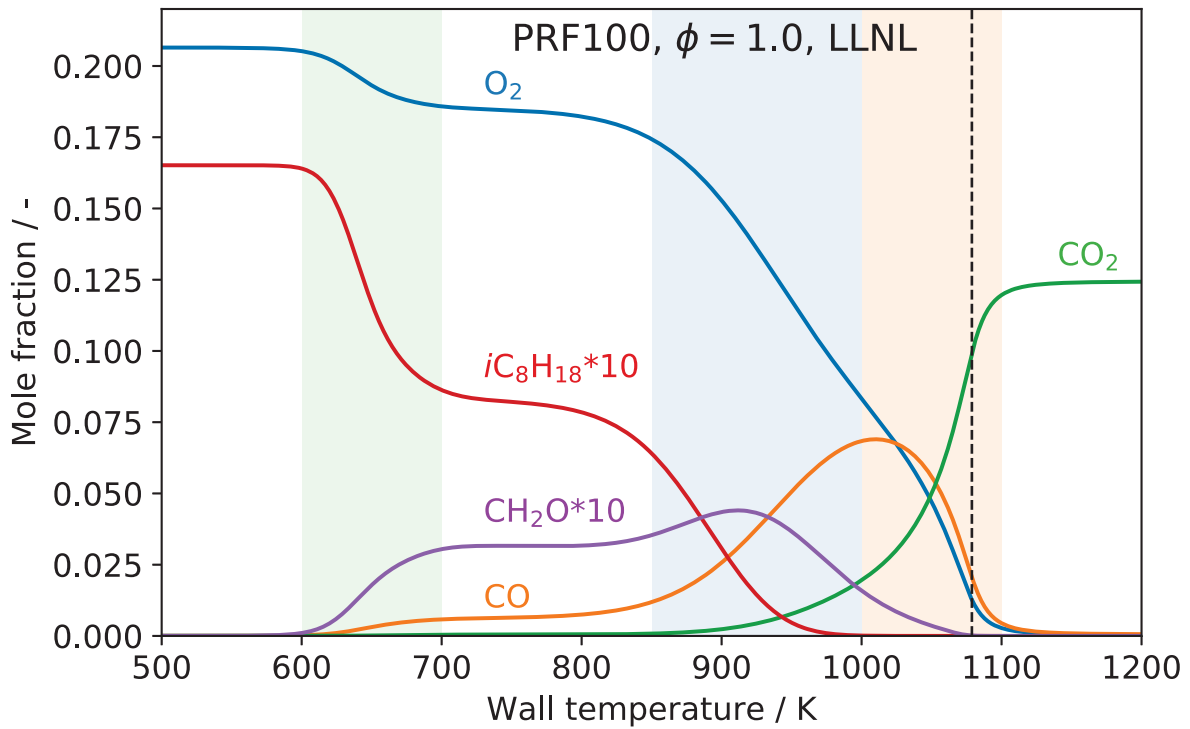


Figure 2.7: Major species profiles for PRF100 at  $P = 100$  kPa and  $\Phi = 1.0$  by LLNL. The vertical dashed line indicates the position of the HRR peak of the hot flame. The colored boxes indicate from left to right the approximate location of the cool flame, blue flame and the hot flame.

understand the structure of the separated weak flames. The species profiles can be divided into three distinct regions. At wall temperatures between 600 K and 700 K, the cool flame can be found. Here, Low Temperature Oxidation (LTO) consumes fuel and produces intermediate species, such as formaldehyde ( $\text{CH}_2\text{O}$ ). The next weak flame, the blue flame, can be found between wall temperatures of 850 K and 1000 K. Here, remaining fuel and a large part of the previously produced intermediate species are consumed, which leads to the production of carbon monoxide (CO). The final reaction zone, the hot flame, is then located at wall temperatures between 1000 K and 1100 K. At this stage of the weak flame, the remaining species, such as CO, are oxidized and  $\text{CO}_2$  is formed as a final combustion

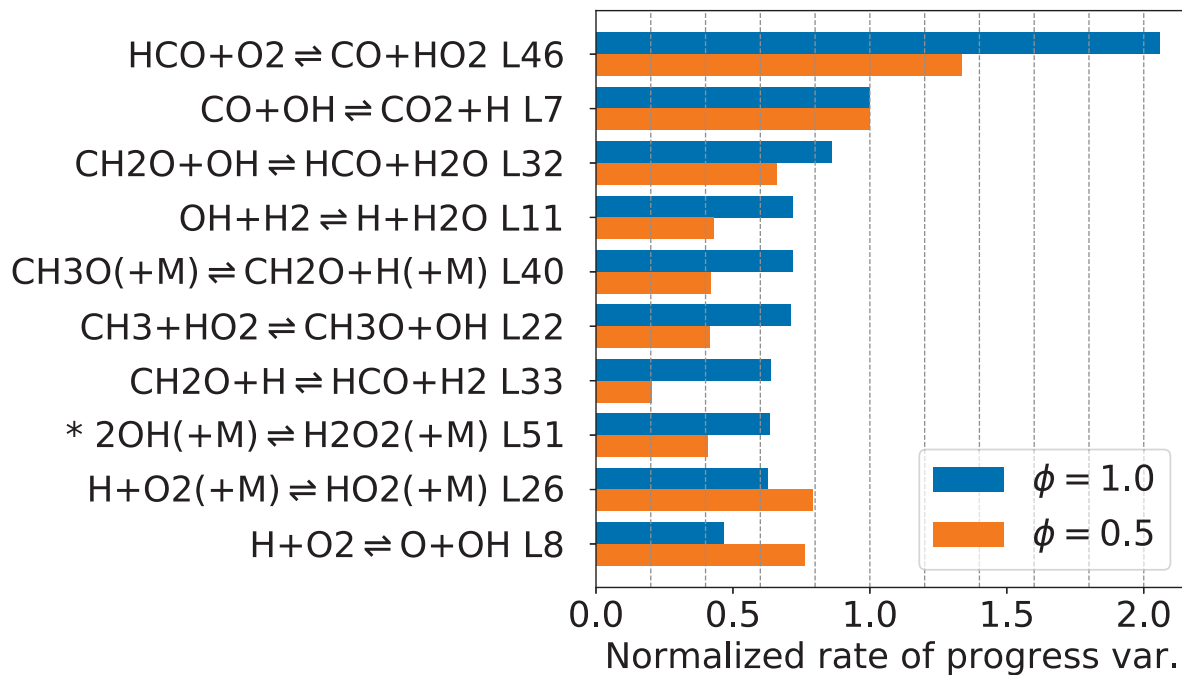


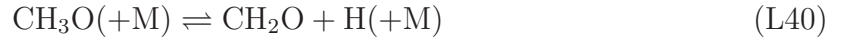
Figure 2.8: Normalized rate of progress variables (by  $\text{CO} + \text{OH} \rightleftharpoons \text{CO}_2 + \text{H}$ ) at  $T_{\text{wall}} = 1030 \text{ K}$  for major ten reactions as obtained by LLNL for PRF100 at  $P = 100 \text{ kPa}$  and  $\Phi = 1.0$  as well as corresponding values at  $\Phi = 0.5$ . \*net reaction rate is from right to left.

product.

### 2.3.2 Effect of the equivalence ratio on chemical reactions

In this section, chemical reactions will be discussed in more detail. Reactions will be numbered by their respective number in the reaction mechanisms, with an additional L or K in the beginning for the LLNL and KUCRS mechanism, respectively. Figure 2.8 shows the normalized rate of progress variables of the ten dominant reactions as obtained by the LLNL mechanism for PRF100 at  $\Phi = 1.0$  and  $0.5$ . The rate of progress variables were taken at a wall temperature of  $1030 \text{ K}$ , which is the location just before the hot flame. At this point, the HRR profiles of  $\Phi = 1.0$  and  $0.5$  show opposing trends. At  $\Phi = 1.0$ , the HRR

is decreasing, while that at  $\Phi = 0.5$  is increasing. The values were normalized by that of L7 (oxidation of CO, dominant reaction of the hot flame) for better comparison. Among all reactions, the consumption of HCO (L46) shows the highest values for both equivalence ratios. At  $\Phi = 1.0$ , however, it is significantly stronger than at  $\Phi = 0.5$ . Other reactions that include C1 species are the consumption of CH<sub>2</sub>O (L32, L33), the consumption of CH<sub>3</sub>O (L40) as well as the consumption of CH<sub>3</sub> (L22). Here, again, the contribution at  $\Phi = 1.0$  is higher than that at  $\Phi = 0.5$



For some hydrogen-oxygen reactions, e. g., L26 and L8, however, rate of progress variables are higher at  $\Phi = 0.5$  than at  $\Phi = 1.0$



## 2 Evaluation of the reactivity of ultra-lean PRF/air mixtures by weak flames

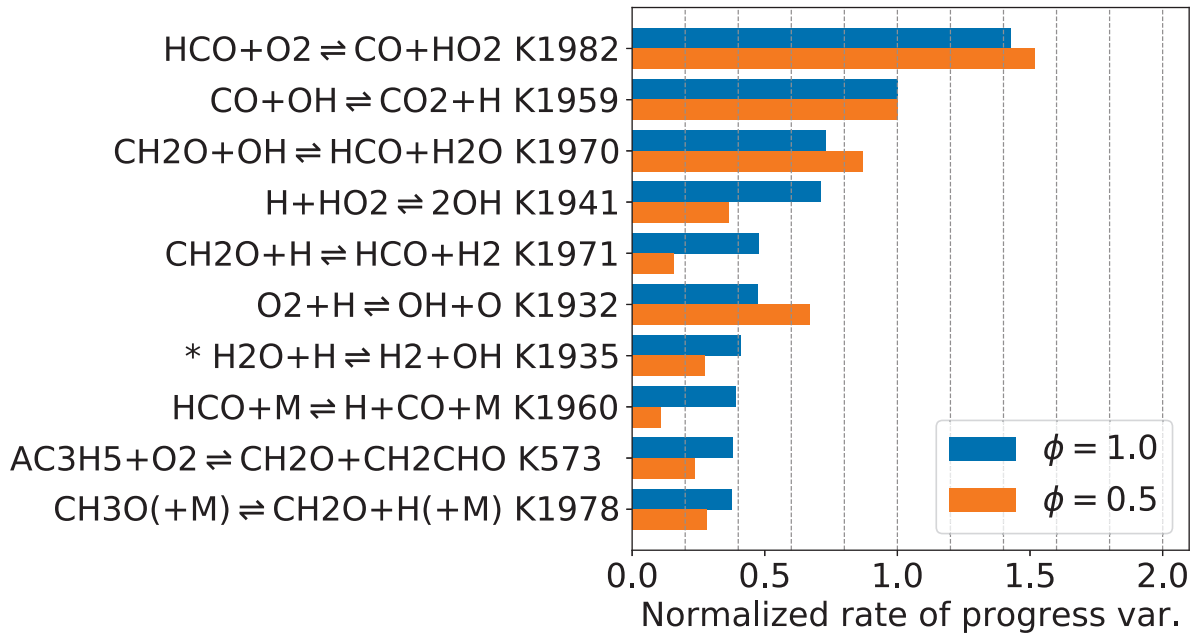


Figure 2.9: Normalized rate of progress variable (by  $\text{CO} + \text{OH} \rightleftharpoons \text{CO}_2 + \text{H}$ ) at  $T_{\text{wall}} = 1053 \text{ K}$  for major ten reactions as obtained by KUCRS for PRF100 at  $P = 100 \text{ kPa}$  and  $\Phi = 1.0$  as well as corresponding values at  $\Phi = 0.5$ . \*net reaction rate is from right to left.

Reaction L8 is an important chain-branching reaction that promotes reactivity. It, however, has to compete with other reactions for H radicals. In the stoichiometric case, the other reactions are stronger than L8 and, therefore, lead to lower reactivity. In the lean case, on the other hand, L8 is among the strongest reactions, which leads to increased chain branching and therefore increased reactivity. This allows the hot flame to be sustained at lower wall temperatures, which is in good agreement with the experimental findings.

In case of the KUCRS mechanism, the HRR profiles start to diverge at  $T_{\text{wall}} = 1053 \text{ K}$ . The ten dominant reactions, again normalized by the CO oxidization reaction K1959, are presented Figure 2.9. The strongest reaction at both equivalence ratios is again the consumption of HCO (K1982), followed by the oxidation of CO (K1959). For K1982, the effect of the equivalence ratio is smaller than in the case of the LLNL mechanism. For



hydrogen-oxygen reactions, however, larger differences between the equivalence ratios exist. At  $\Phi = 0.5$ , the strongest chain-branching reaction is K1932, while at  $\Phi = 1.0$  it is K1941. At stoichiometry, K1941 increases the reactivity, which shifts the hot flame to lower wall temperatures than that of the lean case.



In a next step, A-factor sensitivity analysis was performed in order to further understand why the reactivity trends with regard to equivalence ratio are opposite for the KUCRS mechanism. The A-factor sensitivity analysis was conducted with regard to the wall temperature at the location of the hot flame by increasing the pre-exponential factor by a factor of 2.0 and by decreasing it by a factor of 0.5, respectively (see equation 2.3).

$$S = \frac{T_{\text{wall}}(k_{2.0}) - T_{\text{wall}}(k_{0.5})}{1.5T_{\text{wall}}(k)} \quad (2.3)$$

By comparing the LLNL and the KUCRS reaction mechanisms, it was found that the Arrhenius parameters of the C1 reactions show the same values. Therefore, the sensitivity analysis put its focus on hydrogen-oxygen reactions. The sensitivity coefficients of the KUCRS mechanism for PRF100 at  $\Phi = 1.0$  and  $\Phi = 0.5$  are shown in Figure 2.10. At  $\Phi = 1.0$  as well as  $\Phi = 0.5$ , the reactions with the highest sensitivity coefficients are K1932 and K1938/39. Both reactions compete for H radicals. While K1932 is a chain branching reaction that promotes reactivity, K1938/39 is a chain termination reaction that decreases reactivity. The reactions K1941 and K1942 also consume H radicals and form two competing product channels of  $\text{H} + \text{HO}_2$ . Especially at  $\Phi = 1.0$ , these reactions also show high sensitivity. The third product channel, K1943 shows only low sensitivity and is at rank 19. At  $\Phi = 0.5$ , another chain termination reaction, K1944, shows a very high sensitivity coefficient that is almost as high as that of the other chain termination reaction

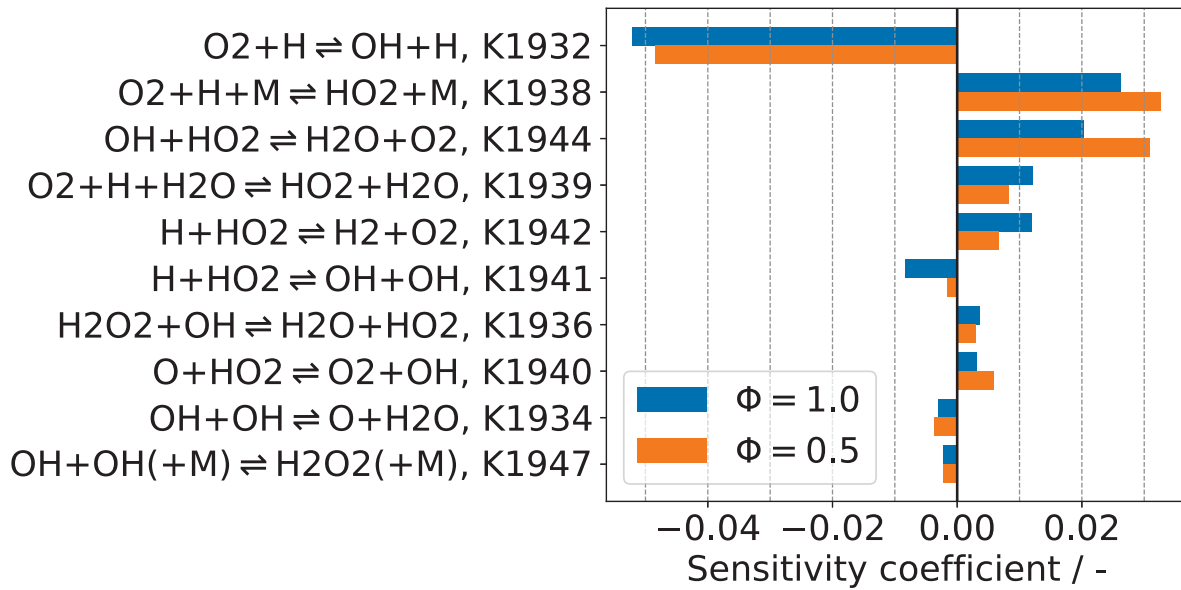


Figure 2.10: Sensitivity coefficients with regard to the wall temperature at the hot flame location of the ten most sensitive H-O reactions as obtained by KUCRS for PRF100 at  $P = 100$  kPa and  $\Phi = 1.0$  as well as  $\Phi = 0.5$ .

K1938. One characteristic that all the mentioned reactions have in common is that they consumer either H or HO<sub>2</sub>.



The sensitivity coefficients of the remaining reactions are small when compared to the strongest six reactions. The strongest reactions of Fig. 2.10 also appear among the reactions in Fig. 2.9. This emphasizes the important role that they have on the reactivity of the hot flame. Based on these results it can be concluded that the competition between chain termination and chain branching reactions governs the reactivity and therefore the location of the hot flame. In order to get a better understanding of the role of these reactions, the

next section will focus on them in more detail.

### 2.3.3 Modification of H-O reaction parameters

The previous section showed that six reactions have a big impact on the movement of the hot flames when the equivalence ratio is changed. Reaction K1943 was also taken into account as it is another product channel of the H + HO<sub>2</sub> group. When comparing the Arrhenius representation of these reactions between the KUCRS and the LLNL mechanism, large differences were found. Furthermore, K1943 is not represented in the LLNL mechanism, leaving out part of the H + HO<sub>2</sub> system. Therefore, another reaction mechanism was used to investigate the role of these reactions for the location of the hot flame. The mechanism that was chosen was the *Foundational Fuel Chemistry Model 1.0* (FFCM-1) [93]. This reaction mechanism was created very recently and contains C0–C2 reactions. It was optimized by using large amounts of theoretical and experimental data. A comparison of the Arrhenius parameters of the seven reactions between the KUCRS mechanism and FFCM is given in Table 2.2. As reaction K1938 is a three body reaction with enhanced third-body efficiencies, their values for both mechanisms are provided in Table 2.3.

Reaction K1932, a chain branching reaction, shows similar Arrhenius parameters for both mechanisms. FFCM shows a slightly higher activation energy that leads to a slightly lower rate constant than that of the KUCRS mechanism. As a chain branching reaction, a decrease of its rate constant by FFCM leads to lower reactivity. Compared to the KUCRS mechanism, this leads to a shift of hot flame to higher wall temperatures by 13 K at  $\Phi = 1.0$  and by 12 K at  $\Phi = 0.5$  (see Table 2.4).

The chain termination reactions K1938/39 shows differences in its representation between

Table 2.2: Arrhenius parameters of KUCRS and FFCM of selected H-O reactions.

Nr.	Mechanism	$A$	$\beta$	$E$
K1932	KUCRS	9.756E+13	0.0	14844.6
	FFCM	9.841E+13	0.0	15310.0
K1938 <sup>1</sup>	KUCRS	6.300E+18	-0.8	0.0
	FFCM	4.560E+12	0.4	0.0
	- Low	6.370E+20	-1.72	525.0
	- Troe	$\alpha = 0.5, T^{***} = 3.0E+01$ $T^* = 9.0E+04, T^{**} = 9.0E+04$		
K1939	KUCRS	6.89E+15	0.0	-2086.5
	FFCM	not available		
K1941	KUCRS	1.69E+14	0.0	874.8
	FFCM	5.89E+13	0.0	300.0
K1942	KUCRS	4.28E+13	0.0	1410.1
	FFCM	2.94E+06	2.1	-1455.0
K1943	KUCRS	3.01E+13	0.0	720.8
	FFCM	1.63E+12	0.0	0.0
K1944	KUCRS	2.89E+13	0.0	-497.1
	FFCM	7.35E+12	0.0	-1093.0
	- duplicate	4.53E+14	0.0	10930.0

<sup>1</sup>Enhanced third-body efficiencies are given in Table 2.3.

Table 2.3: Enhanced third body efficiencies of KUCRS and FFCM for reaction K1938/L26.

Species	KUCRS	FFCM
N <sub>2</sub>	0.223	0.96
O <sub>2</sub>	0.123	0.75
CO	0.25	1.90
CO <sub>2</sub>	0.5	3.45
H <sub>2</sub> O	0.0	15.81
He	not available	0.71
Ar	0.0967	0.60
H <sub>2</sub>	not available	1.87
CH <sub>4</sub>	not available	2.00
CH <sub>2</sub> O	not available	2.50
CH <sub>3</sub> OH	not available	3.00
C <sub>2</sub> H <sub>6</sub>	not available	3.00

Table 2.4: Effect of individual reactions on the wall temperature at the hot flame location when Arrhenius parameters are changed from KUCRS to FFCM for PRF100 at  $\Phi = 1.0$  and 0.5.

Reaction	$\Phi = 1.0$	$\Phi = 0.5$
K1932	13 K	12 K
K1938/39	3 K	-6 K
K1941	8 K	1 K
K1942	-6 K	-3 K
K1943	0 K	0 K
K1944	-17 K	-28 K

the two mechanisms. KUCRS provides it as a third order reaction that is pressure independent. KUCRS also separates the reaction into one with  $\text{H}_2\text{O}$  as a third body (K1939) and another one that contains all other species as third bodies (K1938). FFCM as well as LLNL, however, combine all third bodies into one reaction that is provided as a second order reaction with a Troe fall-off representation and a low-pressure limit (reaction L26 in case of the LLNL mechanism). In order to compare the rate constants of these three body reactions with enhanced third-body efficiencies, a gas composition had to be given. It was chosen as the composition at the location of the hot flame of PRF100 as obtained by the KUCRS mechanism (see Table 2.5 for details). The largest difference between the two equivalence ratios lies in the mole fraction of  $\text{O}_2$  that is approximately three times higher in the lean case. Mole fractions of  $\text{H}_2\text{O}$ ,  $\text{CO}_2$  and  $\text{CO}$ , however, are lower in the lean case. Figure 2.11 shows the comparison of the rate constants at  $\Phi = 1.0$  and  $\Phi = 0.5$  for reactions

Table 2.5: Species with highest mole fractions at hot flame locations of KUCRS, PRF100 at  $\Phi = 1.0$  and 0.5.

Species	Mole fraction	
	$\Phi = 1.0$	$\Phi = 0.5$
N <sub>2</sub>	0.721	0.758
O <sub>2</sub>	0.037	0.107
H <sub>2</sub> O	0.123	0.071
CO <sub>2</sub>	0.062	0.051
CO	0.047	0.012
Others	0.010	0.001

K1938/39 (KUCRS) and L26 (FFCM) over the temperature range that is of interest in this study (373 K to 1300 K). The gas composition was taken from Table 2.5. In case of the KUCRS mechanism, the two rate constants are multiplied by the total concentration of the mixture [M] and are added up to make it comparable to the single rate constant of FFCM. As the temperature increases, both reaction mechanisms provide decreasing rate constants at both equivalence ratios. For both reaction mechanisms, the rate constants at  $\Phi = 1.0$  are higher than those at  $\Phi = 0.5$ . In case of FFCM, the difference between the two equivalence ratios is smaller than that of KUCRS. The lower rate constants at lower equivalence ratios are caused by lower concentrations of species that have higher enhanced third-body efficiencies, e. g., CO<sub>2</sub>, H<sub>2</sub>O and CO. When comparing the rate constants of the two mechanisms, FFCM shows larger values at lower temperatures, while KUCRS has larger values at higher temperatures. The cross-over point at  $\Phi = 1.0$  is at

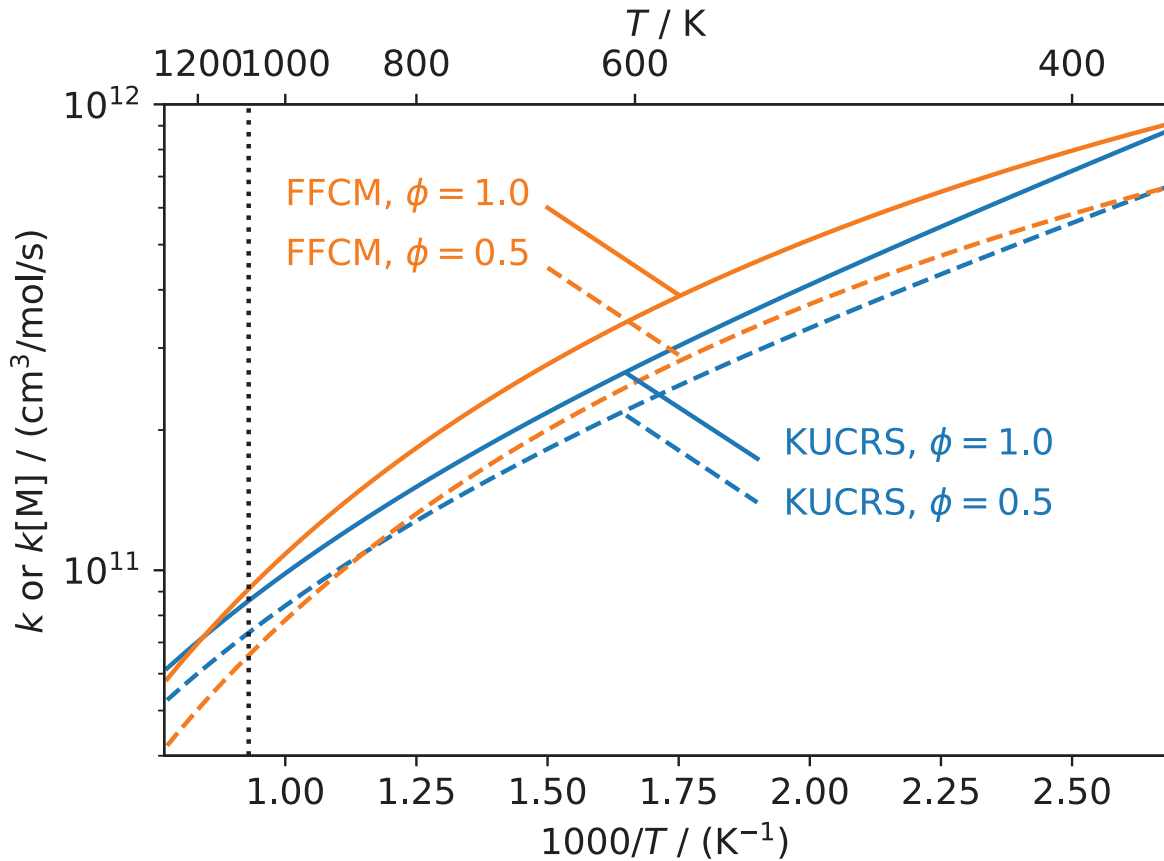


Figure 2.11: Sum of rate constants of K1938+K1939 multiplied by [M] for KUCRS and rate constant of L26 for FFCM at  $P = 100$  kPa and  $\Phi = 1.0$  and  $0.5$ . Vertical line indicates hot flame location of KUCRS for PRF100 at  $\Phi = 1.0$ .

approximately 1200 K, while it is at 900 K at  $\Phi = 0.5$ . This leads to important differences in the temperature range of the hot flame. In the stoichiometric case, FFCM has a higher rate constant than KUCRS. As this is a chain termination reaction, this leads to lower reactivity and a hot flame at higher wall temperatures. This effect can be seen in Table 2.4, where the hot flame of FFCM is located at 3 K higher than that of KUCRS. At ultra-lean conditions, however, FFCM shows a lower rate constant than KUCRS, which consequently leads to higher reactivity and a hot flame at lower wall temperatures by 6 K (see Table 2.4). A previous study by our group showed the effect of exhaust gas recirculation (EGR) on



the hot flame of syngas [76]. As  $\text{CO}_2$  and  $\text{H}_2\text{O}$  were added, the chain termination reaction K1938/39 was enhanced the hot flames shifted to higher wall temperatures. This agrees well with the current results and shows the possibility of using the MFR to investigate even small differences in reactivity, such as in the chain termination reaction.

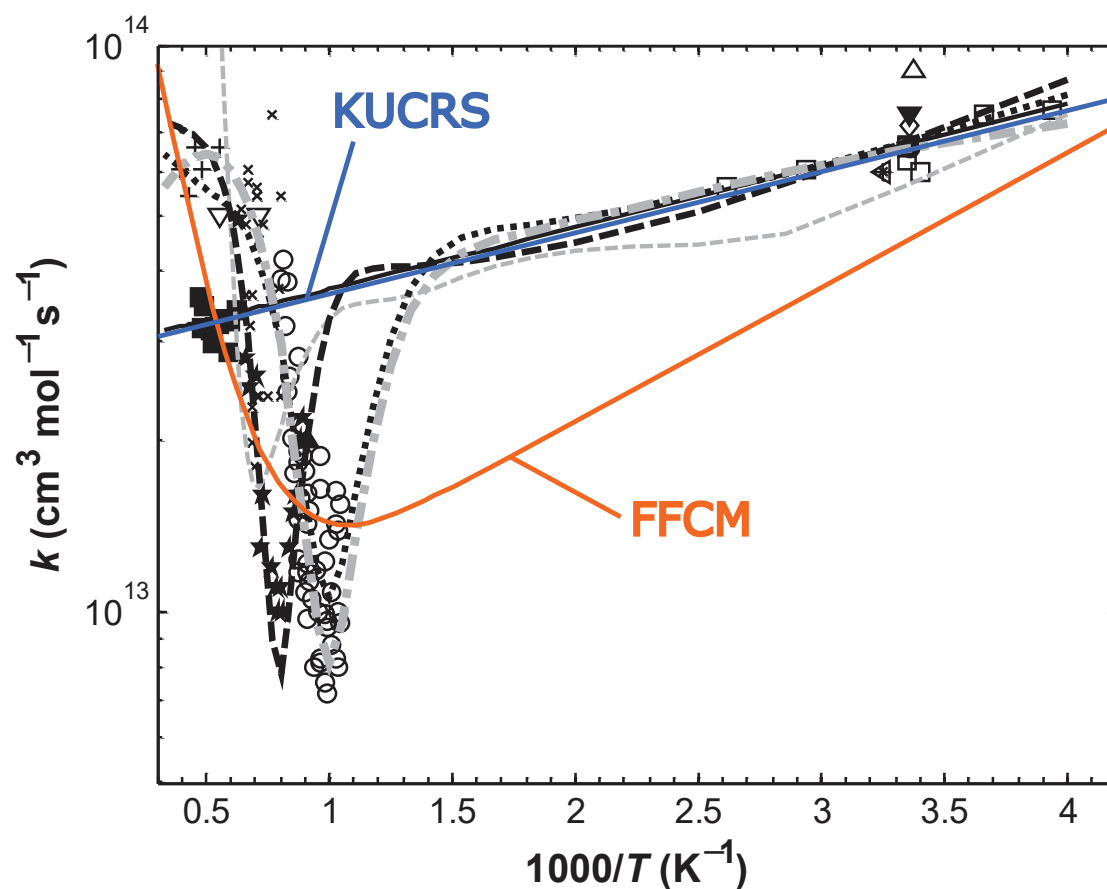
Reaction K1941 is another important chain branching reaction. It is one of the three distinct reaction channels of  $\text{H} + \text{HO}_2$  together with K1942 (chain termination) and K1943 (chain propagation). All three reactions depend on the concentrations of  $\text{H}$  and  $\text{HO}_2$ . They are therefore highly sensitive to changes of the equivalence ratio and show some of the highest sensitivities among the  $\text{H-O}$  reactions [94]. Over the temperature range of the MFR, the rate constant of K1941 of FFCM is lower than that of the KUCRS mechanism. As it is a chain branching reaction, this results in lower reactivity of FFCM and a shift of the hot flame at  $\Phi = 1.0$  to higher wall temperatures by 8 K as compared to KUCRS (see Table 2.4). At  $\Phi = 0.5$ , this reaction is not as important as the concentration of  $\text{H}$  radicals is lower and only leads to a shift of the hot flame to higher wall temperatures by 1 K (see Table 2.4). The rate constant of the chain termination reaction K1942 of FFCM is also lower than that of KUCRS, which, in this case, increases reactivity. This leads to a shift of the hot flames to lower wall temperatures by 6 K at  $\Phi = 1.0$  and 3 K at  $\Phi = 0.5$ . The third reaction, K1943 is a much weaker reaction than the previous two and contributes only about 5 % of their reaction rate. This reaction only has negligible effect on the flame location and shifts it by less than 1 K at both equivalence ratios.

Another reaction that competes for  $\text{HO}_2$  radicals is the chain termination reaction K1944. This reaction is especially important at lean conditions. Until now, however, an adequate representation of its Arrhenius parameters is still discussed controversially. Experimental studies found that a strong minimum of the rate constant exists in the temperature range

## 2 Evaluation of the reactivity of ultra-lean PRF/air mixtures by weak flames

from 1000 K to 1250 K [95, 96] (see Figure 2.12). This minimum was also investigated in a theoretical study [97]. In agreement with these findings, the FFCM mechanism employs a bi-Arrhenius expression. KUCRS, on the other hand, only used a single expression and, therefore, does not contain the rate constant minimum (see Figure 2.12). The minimum of the rate constant can be found in a temperature range that is close to the temperature at the location of the hot flame, which is around 1070 K. As the KUCRS mechanism does not contain this minimum, this leads to large differences between the FFCM and the KUCRS mechanism. By using the Arrhenius parameters of the FFCM mechanism, the reaction is weakened. As this is a chain termination reaction, this leads to higher reactivity, especially in the case of  $\Phi = 0.5$ . Here, the hot flame moves to lower wall temperatures by 28 K, while it moves by 17 K at  $\Phi = 1.0$  (see Table 2.4). This makes it the reaction with the largest impact among all investigated reactions and also with the biggest difference between  $\Phi = 1.0$  and  $\Phi = 0.5$ .

In order to evaluate the total effect of the differences in the rate parameters between the KUCRS and the FFCM mechanism, the parameters for the selected seven reactions (see Table 2.2) of the FFCM mechanism were inserted into the KUCRS mechanism. The resulting HRR profiles of the modified KUCRS mechanism (KUCRS+FFCM) and those of the original mechanism are plotted in Figure 2.13. At  $\Phi = 1.0$ , the heat release rate profile of the modified mechanism is similar to that of the original. In the blue flame, the differences are very small, with the KUCRS+FFCM showing slightly higher values. For the hot flame, the differences become larger. While the HRR peak of KUCRS+FFCM is slightly lower than that of KUCRS, its location is located 2 K upstream at  $T_{\text{wall}} = 1063$  K. Larger differences can be found at  $\Phi = 0.5$ . In the blue flame, the KUCRS+FFCM again shows higher values than the original mechanism. This is followed by a steady increase



▽ Peeters and Mahnen (1973)	★ Hippler et al. (1995)
▼ DeMore (1980)	○ Kappel et al. (2002)
◁ Lii et al. (1980)	× Srinivasan et al. (2006)
* Cox et al. (1981)	■ Hong et al. (2010)
△ Kurylo et al. (1981)	— Keyser (1988)
● Braun et al. (1982)	- - - - - Sivaramakarishnan et al. (2007)
◇ DeMore (1982)	- - - - - Chaos & Dryer (2008) - Hippler
+ Goodings & Hayhurst (1988)	⋯⋯⋯ Chaos & Dryer (2008) - Kappel
□ Keyser (1988)	- · - · - Rasmussen et al. (2008)
▲ Hippler & Troe (1992)	

Figure 2.12: Rate constants of reaction K1944:  $\text{OH} + \text{HO}_2 \rightleftharpoons \text{H}_2\text{O} + \text{O}_2$ . Symbols represent experimental data [95, 96, 98–110], and lines represent proposed rate constant expressions [101, 111–113] as indicated in the legend. Figure taken with permission from [94] and adjusted for KUCRS and FFCM curves.

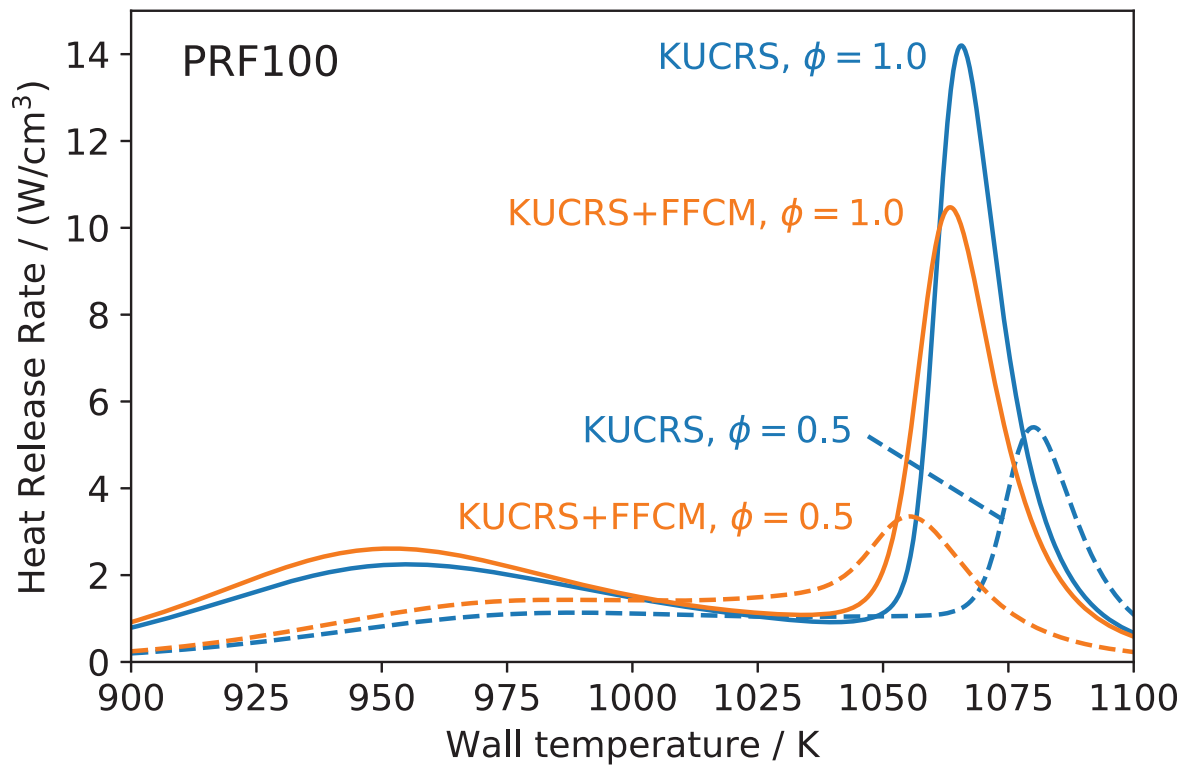


Figure 2.13: Heat release rate profiles of original KUCRS and KUCRS+FFCM for PRF100 at  $P = 100$  kPa and  $\Phi = 1.0$  and  $0.5$ .

towards the hot flame, which is located at a wall temperature that is 25 K lower than that of KUCRS. This shifts the peak location from 1080 K (KUCRS) to 1055 K (KUCRS+FFCM). Similar to the stoichiometric case, the peak HRR value of KUCRS+FFCM is lower than that of KUCRS. Through the modification of KUCRS by FFCM, the order of the peaks of the stoichiometric and lean case was switched. In the case of the original KUCRS, the peak at  $\Phi = 1.0$  showed higher reactivity and was located at a 15 K lower wall temperature than that at  $\Phi = 0.5$ . For the modified KUCRS+FFCM, however, the peak at  $\Phi = 0.5$  is located at 8 K lower wall temperature than that at  $\Phi = 1.0$ , which indicates higher reactivity. This result agrees very well with that of the experiment. These wall temperatures along with those of the other cases as obtained by the KUCRS+FFCM as well as those obtained by

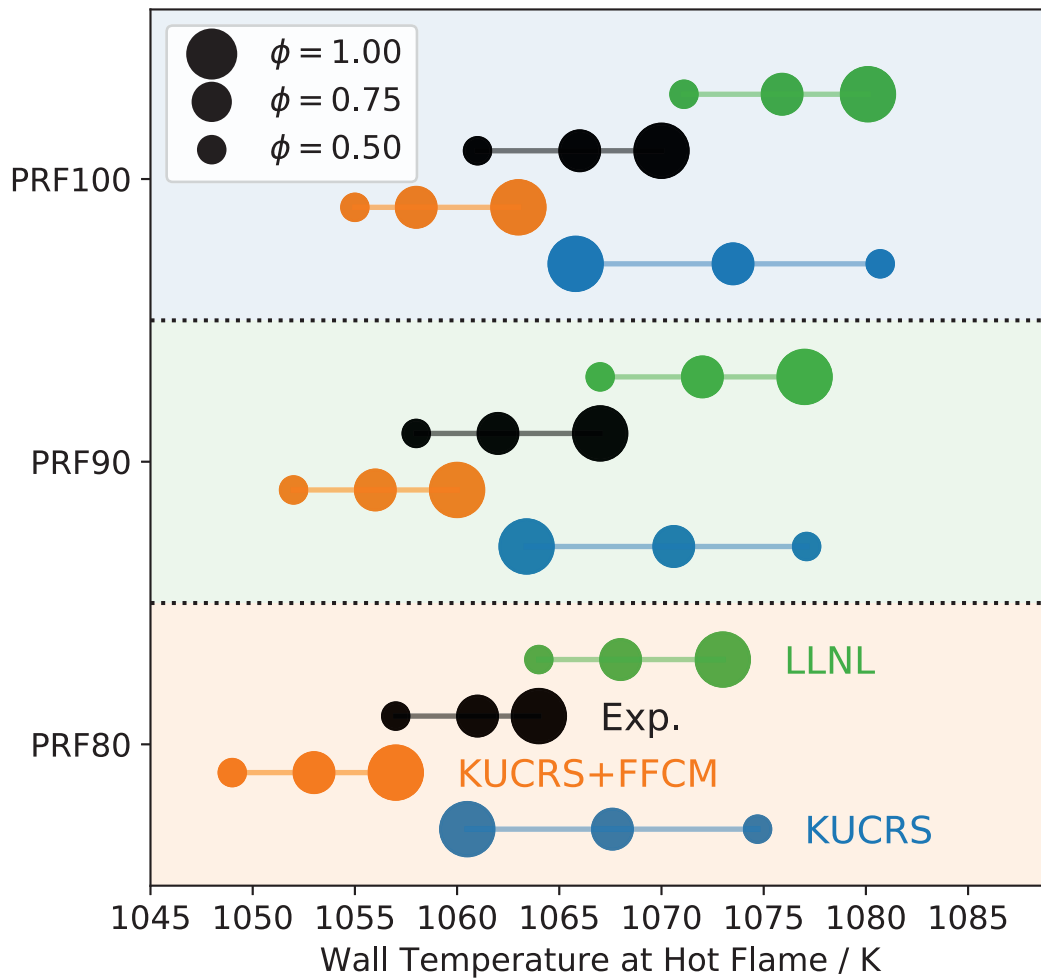


Figure 2.14: Wall temperature at hot flame location for all investigated cases, experiments and simulations including KUCRS+FFCM.

the original KUCRS and LLNL mechanisms and the experimental results are plotted in Figure 2.14. For all three fuels, KUCRS+FFCM shows the hot flames moving to lower wall temperatures when the equivalence ratio is decreased. As the RON is decreased from 100 to 80, the hot flames also shift to lower wall temperatures. These trends agree very well with the experimental flame locations. The agreement with the experiment is within 8 K, which is even an improvement over the LLNL mechanism.

To further investigate the effect of KUCRS+FFCM, the mole fraction profile of an

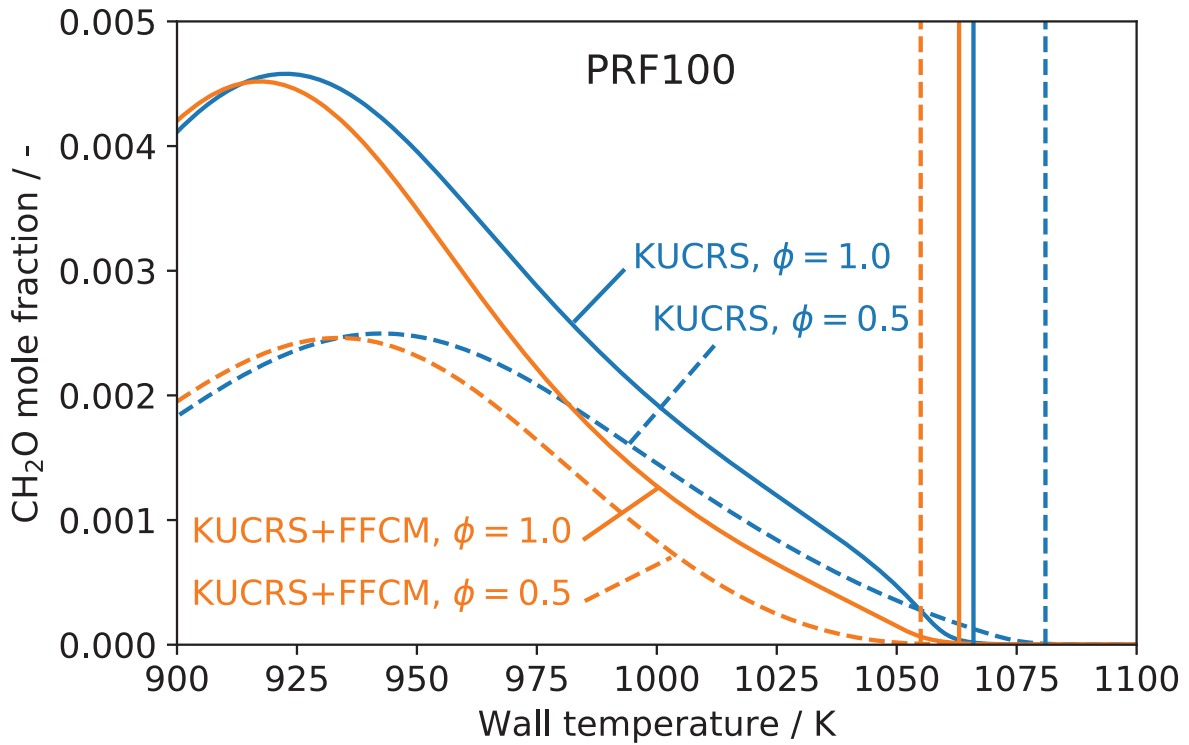


Figure 2.15: CH<sub>2</sub>O mole fraction profiles of original KUCRS and KUCRS+FFCM of PRF100 at  $P = 100$  kPa and  $\Phi = 1.0$  and  $0.5$ . Vertical lines represent the hot flame location of each case.

important intermediate species, CH<sub>2</sub>O, was analyzed. The profiles of KUCRS and KUCRS+FFCM at  $\Phi = 1.0$  and  $\Phi = 0.5$  are shown in Figure 2.15. As was explained in section 2.3.1, CH<sub>2</sub>O is mostly consumed in the blue flame. In Figure 2.15, this is true for all four conditions. The hot flames are then located at wall temperatures, where the CH<sub>2</sub>O mole fraction approaches zero. During the blue flame, the mole fractions at  $\Phi = 1.0$  are higher than those at  $\Phi = 0.5$  for both mechanisms. For the original KUCRS mechanism, as the wall temperatures approaches that of the hot flame (around 1050 K), the mole fraction at  $\Phi = 1.0$  shows a sudden decrease and falls below that at  $\Phi = 0.5$ . This sudden drop indicates an influence of the hot flame on the blue flame that is absent at  $\Phi = 0.5$ . The influence of the hot flame leads to an increased reactivity and, consequently, a shift of

the hot flame to lower wall temperatures, which is the opposite of the experiment. For KUCRS+FFCM, the mole fractions at both equivalence ratios are lower than those of KUCRS, which leads to lower wall temperatures at the hot flames. Furthermore, the sudden drop of the mole fraction at  $\Phi = 1.0$  is not observed. Therefore, the  $\text{CH}_2\text{O}$  mole fraction at  $\Phi = 1.0$  reaches zero slower than that at  $\Phi = 0.5$ , which leads to an order of the hot flames that agrees with that of the experiment.

### 2.3.4 Validation by ignition delay times and laminar burning velocities

Apart from MFR results, the KUCRS+FFCM mechanism has to be tested for other investigation methods. In this section, the modified mechanism will be used to evaluate ignition delay times and laminar burning velocities. Ignition delay times were calculated through 0-dimensional computations by Chemkin-Pro Aurora [92]. The system was modeled as adiabatic with constant volume. The temperature ranged from 500 K to 1428 K and the initial pressure was set to 500 kPa, which is in the pressure range of spark ignition in an SI-engine at ultra-lean conditions. Figure 2.16 shows the resulting IDTs of KUCRS and KUCRS+FFCM for PRF100 at  $\Phi = 1.0$  and 0.5. Two zones with different responses to the equivalence ratio are seen. In the lower temperature range up to 1000 K, a decrease of the equivalence ratio leads to longer ignition delay times, i. e., lower reactivity. In this temperature regime, the overall reactivity is governed by fuel reactions [32], which get stronger for higher equivalence ratios. At temperatures above 1000 K, however, lean conditions experience shorter ignition delay times and therefore have a higher reactivity. In this high temperature regime, the overall reactivity is governed by the chain branching

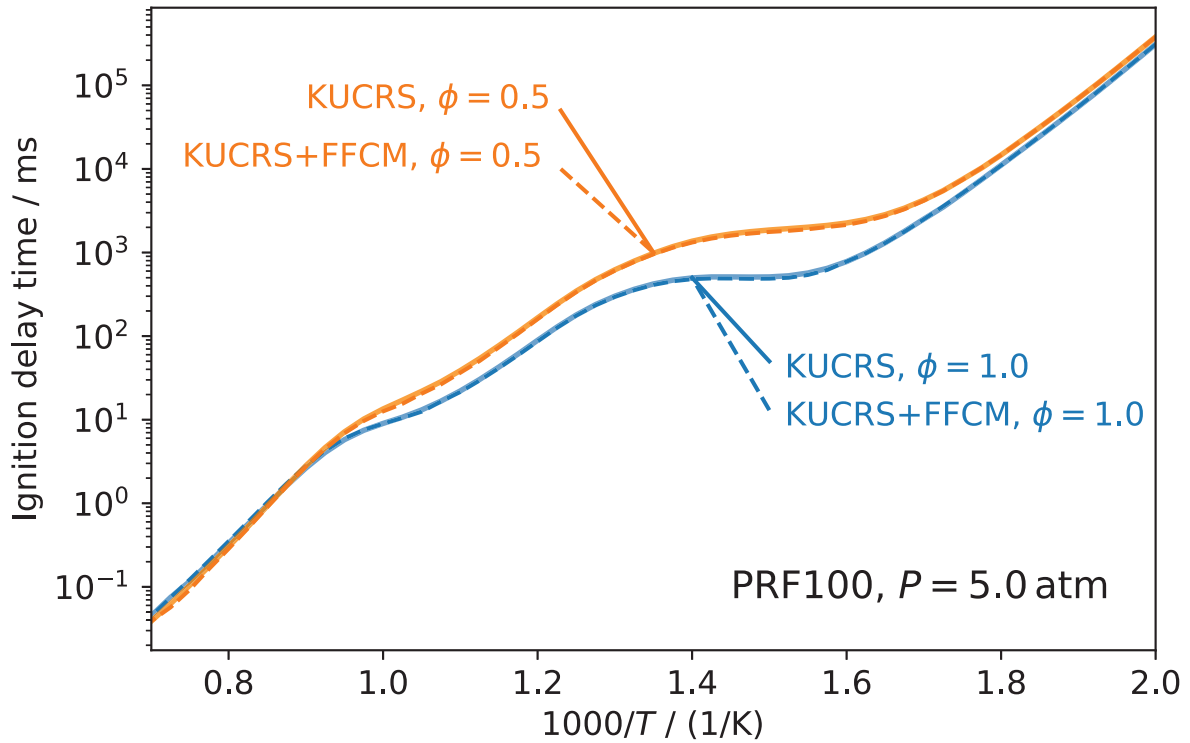


Figure 2.16: Ignition delay times of original KUCRS and KUCRS+FFCM for PRF100 at  $P = 500 \text{ kPa}$  and  $\Phi = 1.0$  and  $0.5$ .

reaction K1932:  $\text{O}_2 + \text{H} \rightleftharpoons \text{OH} + \text{O}$ . At  $\Phi = 0.5$ , this reaction becomes stronger [32], while it is weakened at  $\Phi = 1.0$  as it competes for H radicals with other reactions. At all investigated initial temperatures, the ignition delay times of the modified mechanism are practically identical to those of the original KUCRS mechanism. This agreement between the two reaction mechanisms is caused by the rapid heat release under adiabatic ignition conditions, which is only little affected by the small changes that were made to the H-O reactions. In the MFR, however, the system is not adiabatic and the chemical reactions proceed gradually. This allows for a larger impact of small changes to chemical reactions. Therefore, the competition between chain termination and chain branching can be observed more clearly.



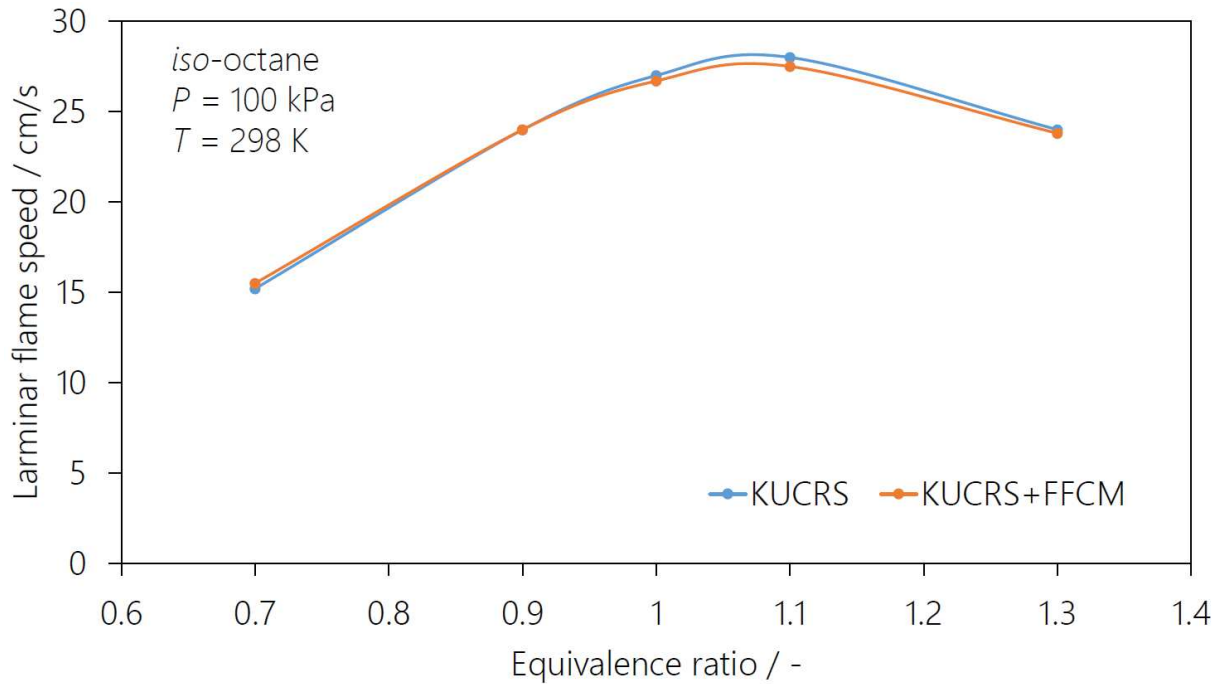


Figure 2.17: Laminar burning velocities for *iso*-octane at 100 kPa and 298 K as obtained by KUCRS and KUCRS+FFCM.

Laminar burning velocities are another common method for the investigation of fuels. To compare the laminar burning velocities of KUCRS and KUCRS+FFCM, computations of a 1-dimensional system were performed by Chemkin-Pro PREMIX [92]. The initial temperature was set to  $T = 298$  K at 100 kPa. The resulting laminar burning velocities at equivalence ratios between 0.7 and 1.3 are shown in Fig. 2.17. Over the whole range, the differences between the two reaction mechanisms are within 2%, which is a very good agreement.

Compared to the results by the MFR, the results of ignition delay times and laminar burning velocities show only small differences between the KUCRS and the KURCS+FFCM mechanism. On the other hand, the MFR shows larger differences even for small changes to chemical reactions, which makes it possible to investigate these reactions in more detail. Therefore, the MFR can be used in future studies to further improve existing and new

chemical reaction mechanisms.

## 2.4 Conclusions

In this chapter, the reactivity of PRF/air weak flames at stoichiometric and ultra-lean conditions was investigated by a vertical-type micro flow reactor with a controlled temperature profile. In the experiment, locations of the weak flames were obtained. To investigate chemical reactions in more detail, one-dimensional steady computations were conducted by modified Chemkin-Pro PREMIX, where heat transfer between the gas-phase and the wall was considered. The observations and conclusions that were made are as follows:

1. By conducting experiments, spatially separated weak flames, namely blue flames and hot flames, were observed. By decreasing the equivalence ratio, the blue flames and hot flames became weaker and the hot flames moved to regions of lower wall temperature, which indicated higher reactivity.
2. By conducting simulations with the LLNL and KUCRS reaction mechanisms, two distinct zones of the HRR profile were identified that corresponded to the blue and hot flames. As the equivalence ratio was decreased, only the LLNL mechanism showed an increased reactivity by shifting the hot flame to lower wall temperatures, while the KUCRS mechanism gave the inverse trend. By analyzing the mole fraction profiles of  $\text{CH}_2\text{O}$ , it was shown that for the LLNL mechanism, the blue flame (consumption of intermediate species) and the hot flame (oxidation of CO and H-O reactions) were well separated. Therefore, reactions of the H-O system governed the reactivity of the hot flame. This led to the shift of the hot flame to lower wall temperatures at  $\Phi = 0.5$  due to the high temperature chain branching reaction  $\text{O}_2 + \text{H} \rightleftharpoons \text{OH} + \text{O}$ .

For the KUCRS mechanism, however, the same analysis showed that the blue flame and the hot flame overlapped spatially. This led to an increase of chain branching at  $\Phi = 1.0$  and therefore to higher reactivity and a hot flame at lower wall temperatures than at  $\Phi = 0.5$ .

3. A sensitivity analysis was conducted for important reactions with regard to the location of the hot flame. For stoichiometric and ultra-lean conditions, seven important H-O reactions were found. These included competing chain termination and chain branching reactions. In a next step, these seven reactions of the KUCRS mechanism were replaced by those of the more recent FFCM model. This led to an inversion of the reactivity trend with regard to decreasing equivalence ratio, which agreed very well with the experimental data. The modified KUCRS+FFCM mechanism was further tested by applying it to ignition delay time simulations as well as simulations of laminar burning velocities. The results were in excellent agreement with the original mechanism, which showed that the changes only had an effect on the MFR but did not change the results for other methods. This highlights the strength of the MFR that allows for the investigation of chemical reactions and the effect of boundary conditions in very high detail.



# Appendix

## 2.A MFR setup

Figure 2.A.1 shows an extended scheme of the MFR setup. It consists of a heated part (373 K) and an unheated part. Three valves are connected to the heated mixing tank.

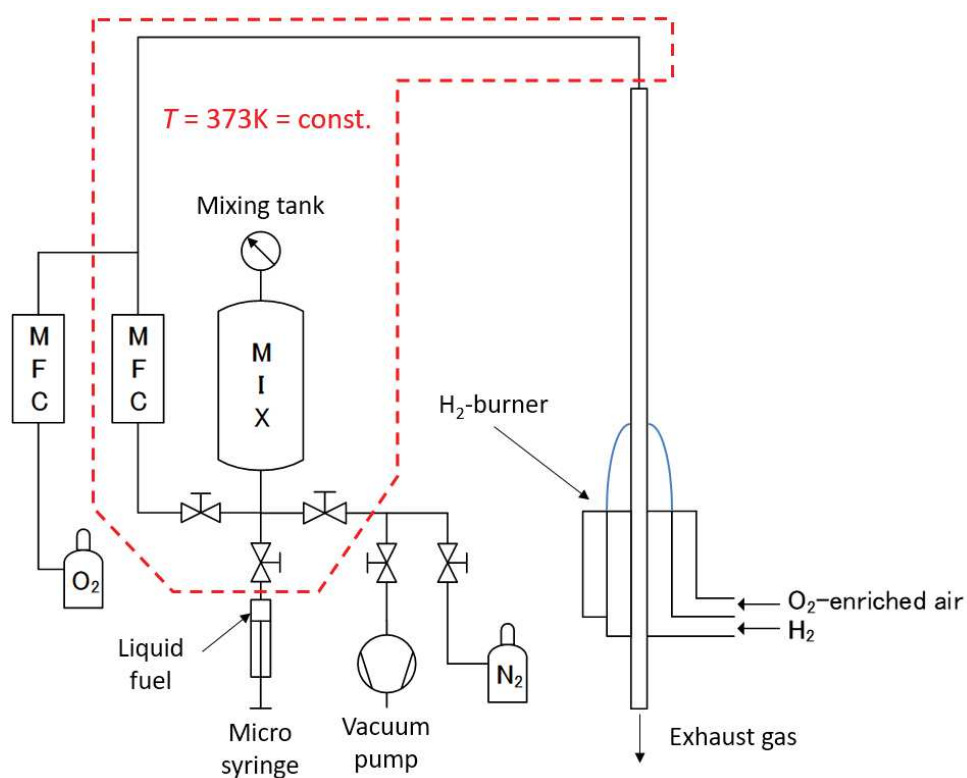


Figure 2.A.1: Scheme of the vertical-type micro flow reactor setup.



Figure 2.A.2: Heated mixing tank. a) Valve for  $N_2$  and vacuum pump. b) Inlet for liquid fuel. c) Heated mixing tank. d) Mass flow controller for fuel/ $N_2$  mixture. e) Mass flow controller for  $O_2$ .

One valve is used to create the vacuum in the mixing tank and to supply  $N_2$ . Another valve is equipped with a septum through which the liquid fuel can be supplied by a micro syringe. Once the fuel and the  $N_2$  are supplied to the tank, their temperature is kept at a constant 373 K to prevent condensation. This mixture is stored for at least 20 minutes to ensure sufficient mixing. The fuel/ $N_2$  mixture is then released from the tank by a third valve, which is connected to a mass flow controller. Oxygen is supplied by a second mass flow controller and fed to the fuel/ $N_2$  mixture. By using two mass flow controllers, the appropriate mixing ratio and flow rate can be controlled. The fuel/ $N_2$ / $O_2$  mixture is then supplied to the top end of the micro flow reactor. During this whole process, the temperature is kept at 373 K to prevent fuel condensation. Figure 2.A.2 shows an image of the mixing tank, the valves and the mass flow controllers.

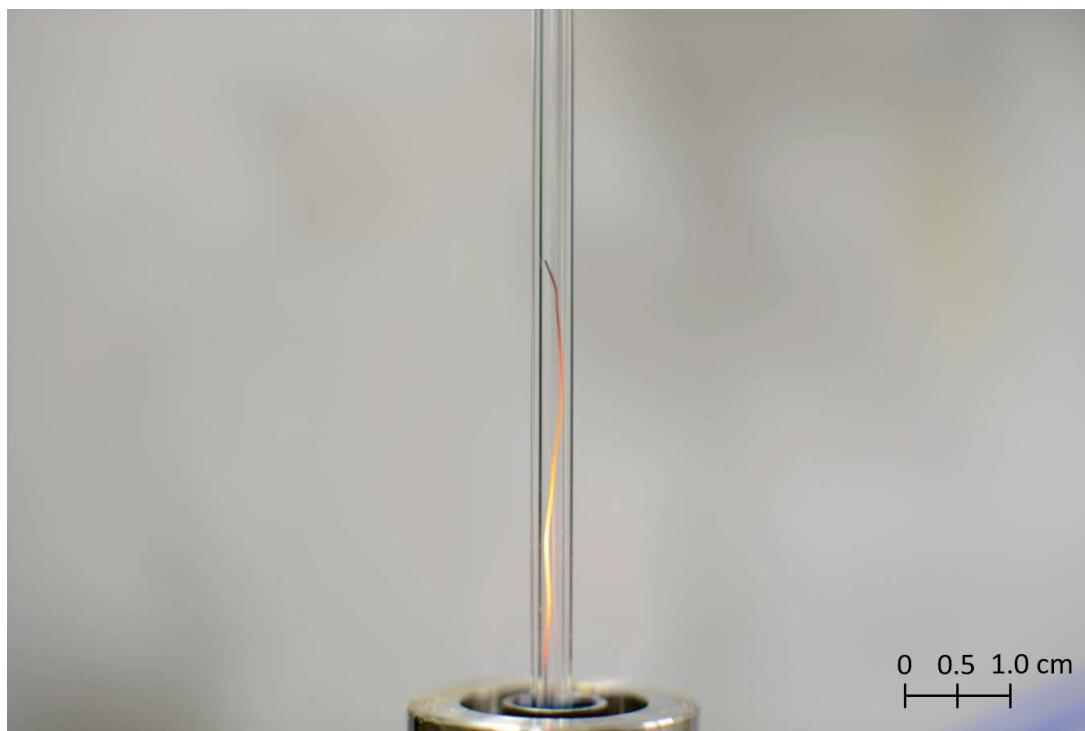


Figure 2.B.1: Thermocouple inserted into the MFR from the lower end.

## 2.B Temperature measurement

Figure 2.B.1 shows the thermocouple inserted into the quartz tube of the MFR. The tip of the thermocouple was slightly bent so that it was in direct contact with the inner wall of the quartz tube. Temperature measurements were started from the cooler top part of the quartz tube. At a given location, the temperature was sampled with a frequency of 10 Hz for up to ten minutes. The temporal temperature profile of a measurement point at the low temperature region is shown in Fig. 2.B.2. Here, the average temperature was 560 K, while the minimum was 13 K lower and the maximum was 22 K higher. The histogram of the measured data is given in Fig. 2.B.3. The measured values are approximately normal-distributed. Based on these measurements, the standard deviation was calculated to be 7.0 K.

The temporal temperature profile of a measurement point of high temperature is given

2 Evaluation of the reactivity of ultra-lean PRF/air mixtures by weak flames

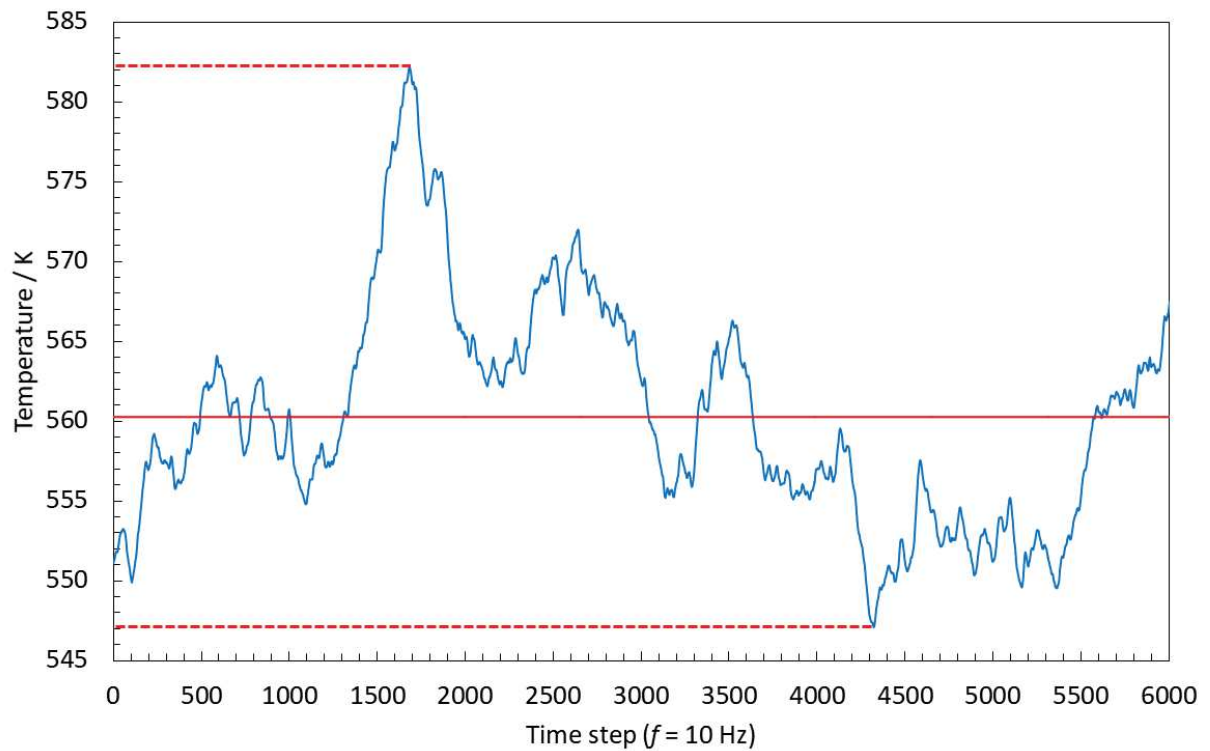


Figure 2.B.2: Temporal temperature profile in the low temperature region, i. e., upper part of the MFR.

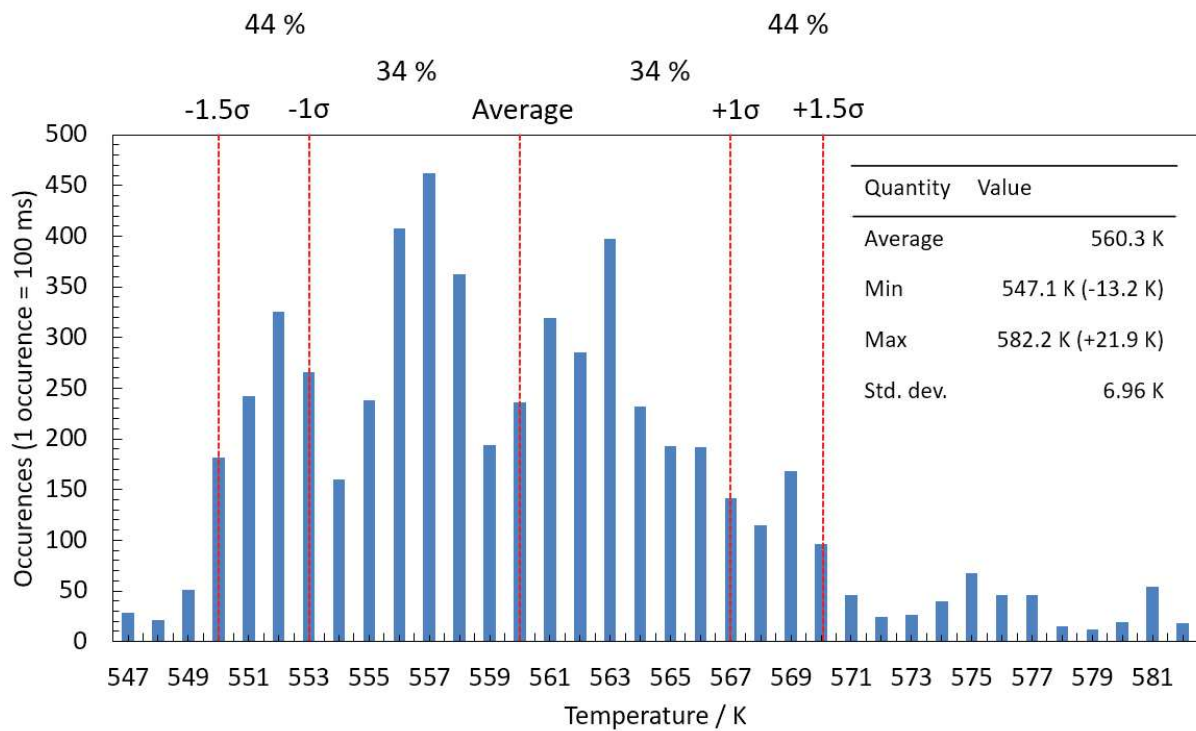


Figure 2.B.3: Histogram of temperature profile in Fig. 2.B.2.



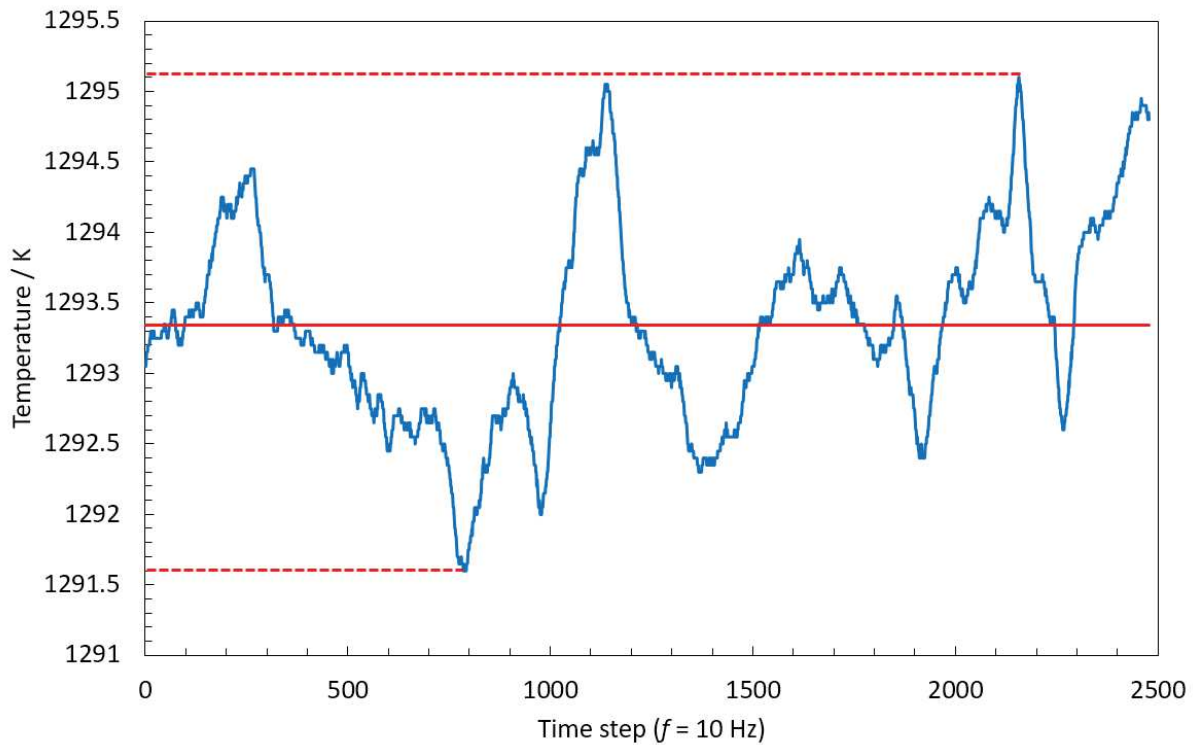


Figure 2.B.4: Temporal temperature profile in the high temperature region, i. e., lower part of the MFR.

in Fig. 2.B.4. Compared to Fig. 2.B.2, the variation of temperature is much smaller. The average temperature is 1293 K, while the minimum is 1292 K and the maximum is 1295 K. The histogram of this data is given Fig. 2.B.5. Here, the standard deviation was calculated to be 0.7 K, which is significantly smaller than in Fig. 2.B.3.

These results show that the wall temperature profile is fairly stable. As the main focus of this chapter was on hot flames, the standard deviation of the temperature in this region was less than 1.0 K.

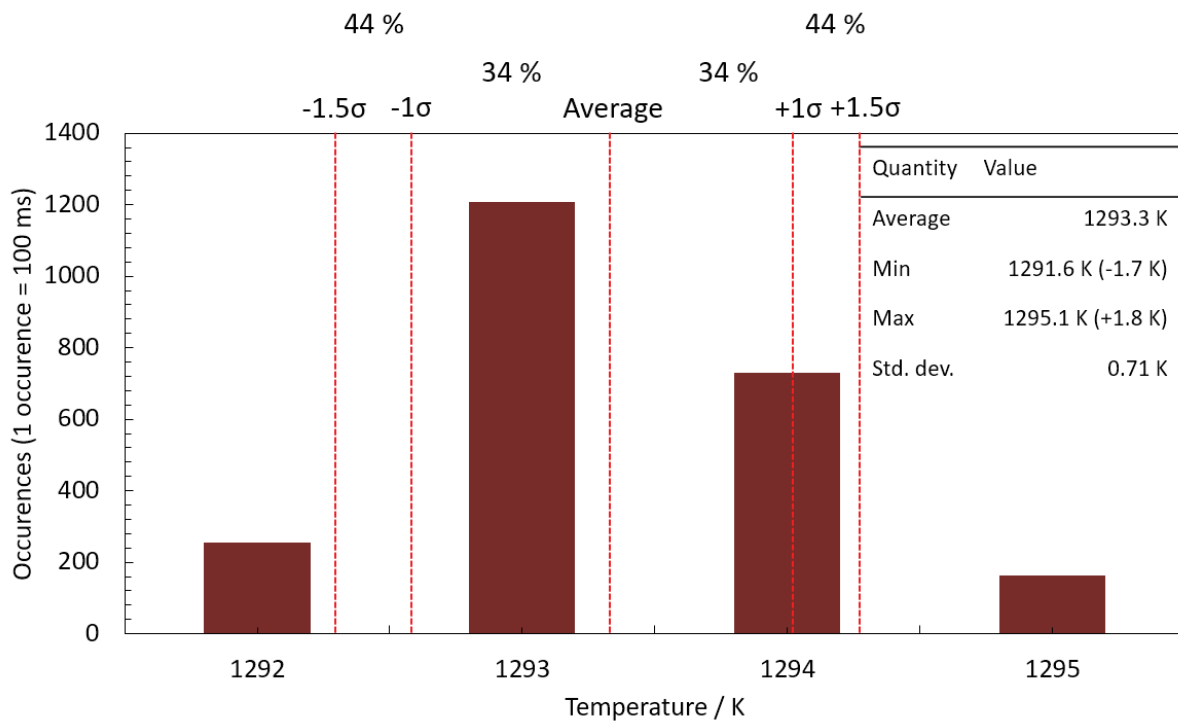


Figure 2.B.5: Histogram of temperature profile in Fig. 2.B.4.

## 2.C Applicability of modified KUCRS at elevated pressure

The effect of equivalence ratio on the weak flames of *iso*-octane at elevated pressure is shown in Fig. 2.C.1. In general, the weak flames of  $\Phi = 1.0$  were brighter than those of  $\Phi = 0.5$  due to the higher fuel mole fractions. For both equivalence ratios, the blue flames and the hot flames moved to lower wall temperatures as the pressure was increased. At all pressures, the hot flames of the ultra-lean case are located at lower wall temperatures than those at stoichiometry.

And overview of the experimental flame locations and the computational results by LLNL, KUCRS and KUCRS+FFCM are given in Fig. 2.C.2. The results of the original KUCRS mechanism diverge from the experimental results for increasing pressure. Furthermore,

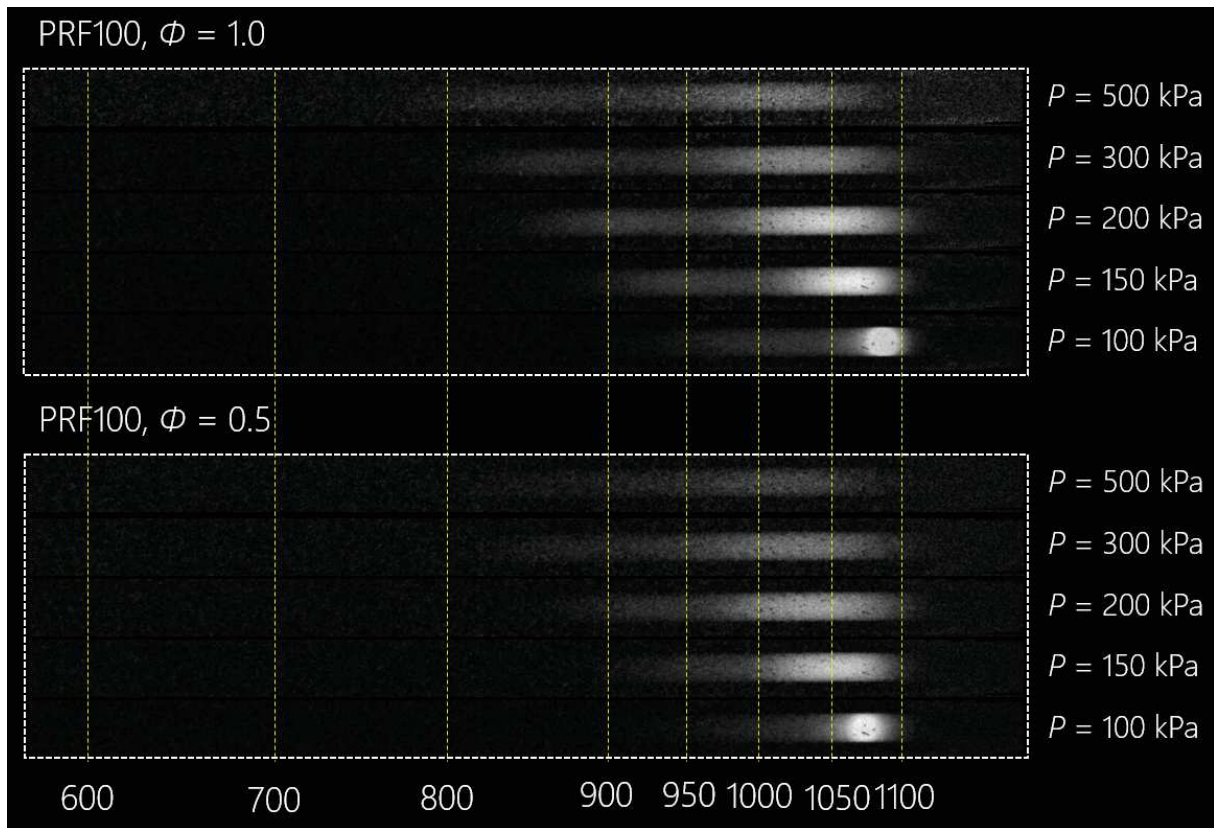


Figure 2.C.1: Effect of equivalence ratio on *iso*-octane weak flames at elevated pressure.

the flame locations of the stoichiometric hot flame and the ultra-lean hot flame change order between 200 kPa and 300 kPa. The modified KUCRS mechanism, on the other hand, showed very good agreement with the experiment even for elevated pressure. LLNL showed relatively good agreement at 100 kPa but the flames shifted downstream as the pressure was increased to 200 kPa. For higher pressures, the flames moved upstream again. This effect will be discussed in more detail in chapter 4. These results show that the modified KUCRS mechanisms can be used at atmospheric as well as at elevated pressures.

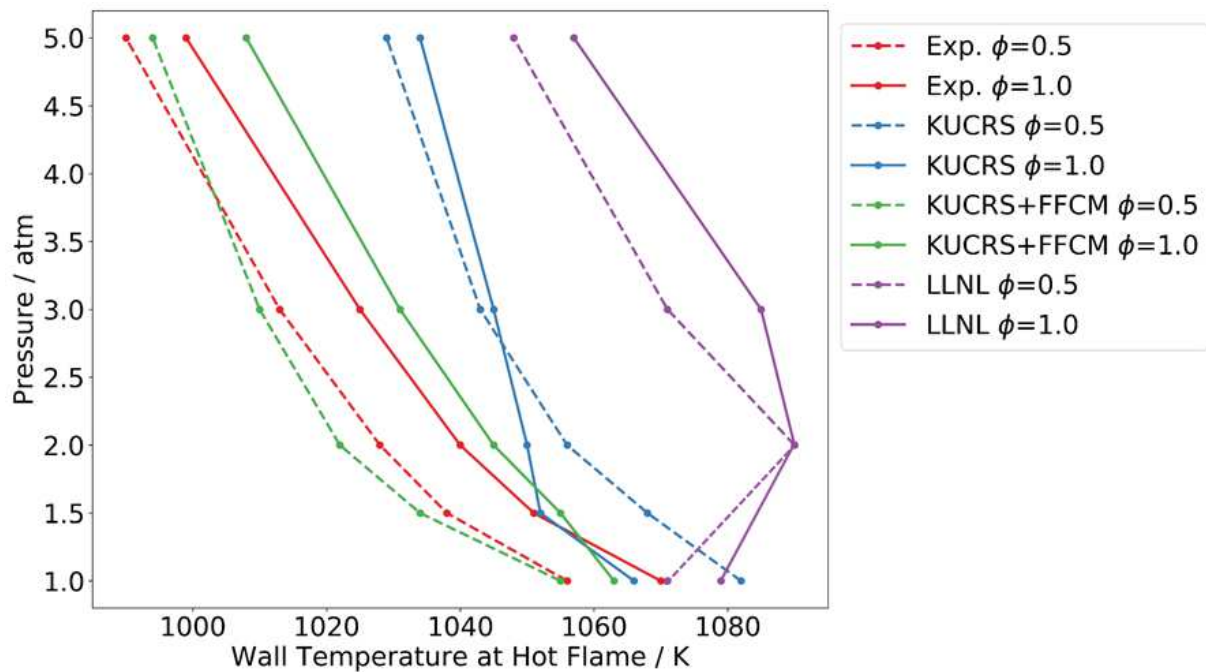


Figure 2.C.2: Wall temperature at hot flame of experiment and computations by LLNL, KUCRS and KUCRS+FFCM.

## 2.D Effect of equivalence ratio on SIP gasoline

### surrogates

Figure 2.D.1 shows the experimental wall temperature at the hot flame location of gasoline surrogates with RON = 90 at atmospheric pressure. It can be seen, that for all surrogates, leaner conditions lead to hot flames at lower wall temperatures. This shift is very similar for all the fuels. The locations of the hot flames agree very well with those of PRF90 with the exception of S3R, whose flame locations are approximately 20 K higher than those of PRF90. S3R has the highest amount of toluene, which has a very low reactivity. This might shift the hot flame to higher temperatures. As the other surrogates have lower toluene content, their results show better agreement with PRF90.

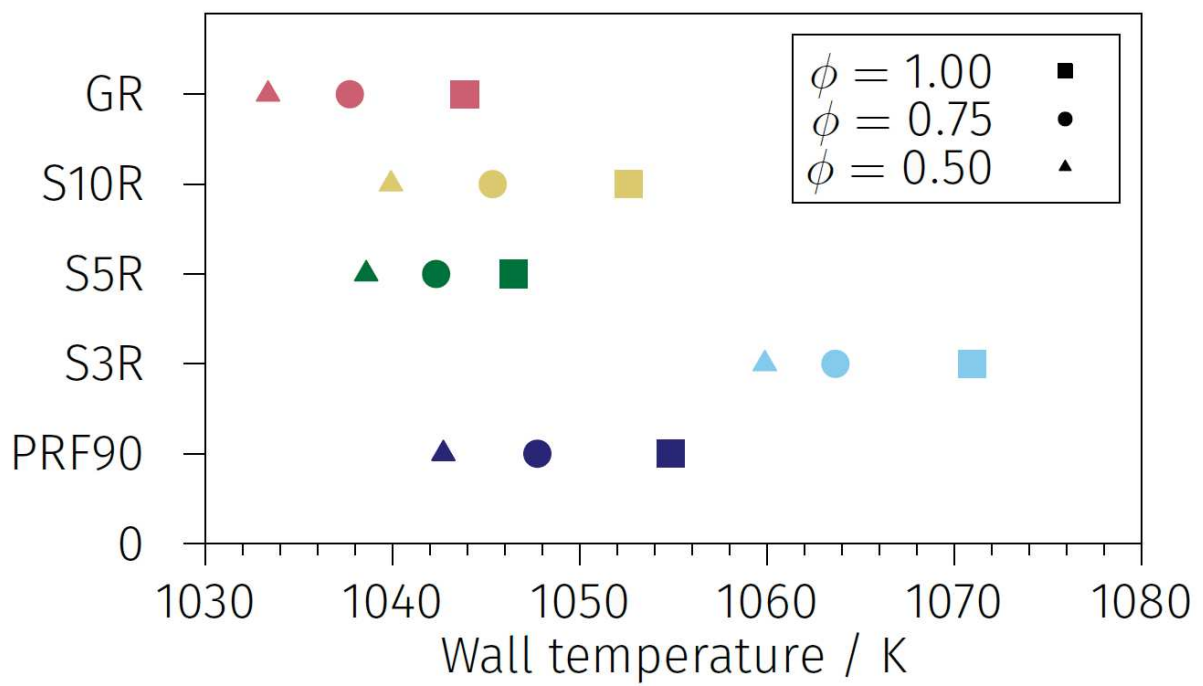


Figure 2.D.1: Wall temperature at experimental hot flame location of gasoline surrogates with RON = 90 at 100 kPa.



# **3 A novel reactivity index for SI engine fuels by separated weak flames in a micro flow reactor with a controlled temperature profile**

## **3.1 Introduction**

After having investigated the effect of ultra-lean conditions on the reactivity of PRF/air mixtures by separated weak flames and after having modified the KUCRS reaction mechanism in chapter 2, the next step was to systematically investigate reactivity for a wider range of fuels by separated weak flames in the micro flow reactor with a controlled temperature profile.

The characterization of fuel reactivity is an ongoing challenge. One approach is to relate the Critical Compression Ratio (CCR), i. e., the compression ratio at which auto-ignition occurs, to fuel reactivity [58, 114, 115]. In these cases, a higher CCR is associated with lower reactivity and vice versa. An influential study showed that the molecular structure

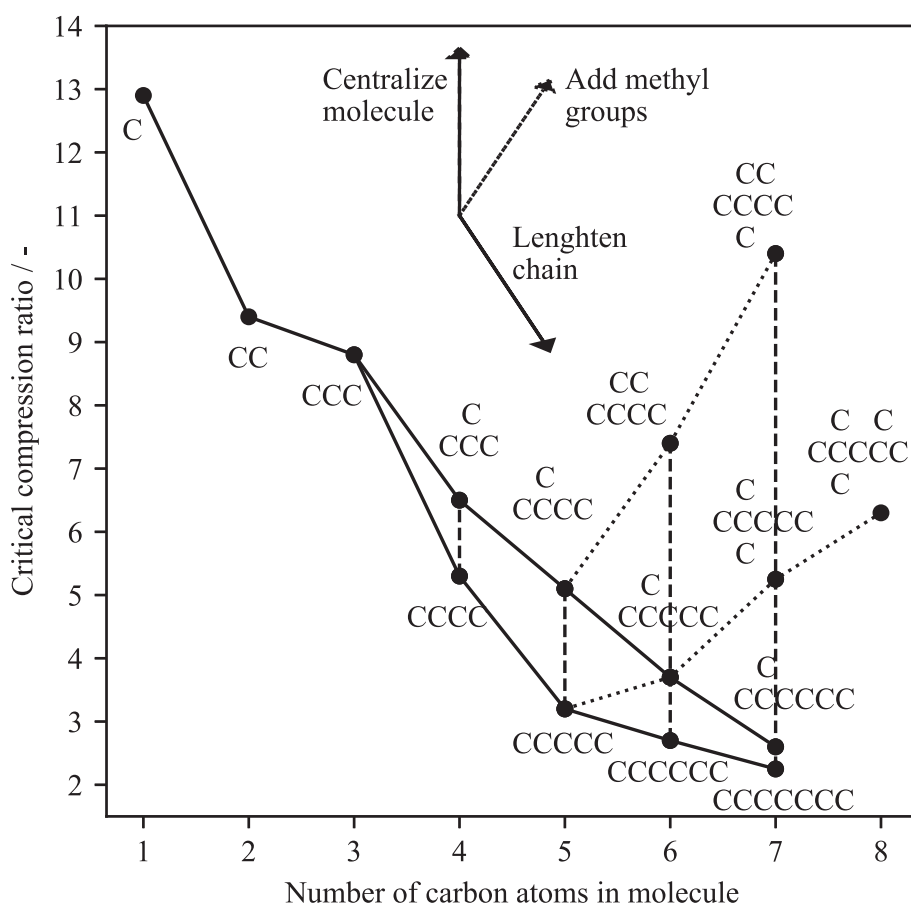


Figure 3.1.1: Critical compression ratios of various alkanes at 600 rpm and 450 K,  $\Phi = 1.0$ .

Adapted with permission from [114]. Copyright 1948 American Chemical Society.

of fuels has a large effect on the CCR and therefore the reactivity [114]. Based on these results, three trends for the CCR of alkanes were found:

1. When the main chain is shortened, the CCR increases.
2. When methyl groups are added, the CCR increases.
3. When the molecular structure is centralized, the CCR increases.

These trends are shown in Fig. 3.1.1 for several alkane isomers. In another study, these results were further analyzed theoretically [115]. It was found that the relative positions



of  $\text{CH}_3$ ,  $\text{CH}_2$  and  $\text{CH}$  groups to each other have a strong impact on reactivity at low temperatures through the important isomerization reaction  $\text{RO}_2 \rightleftharpoons \text{QOOH}$ .

Another method that is used in the determination of fuel reactivity, is the measurement and simulation of Ignition Delay Times (IDT) in shock tubes [84, 86, 87] (see section 1.3.1) as well as in rapid compression machines [84, 86, 90, 116–120] (see section 1.3.2). Two measures that are commonly used to describe a fuel's tendency to experience auto-ignition are the Research Octane Number (RON) and the Motor Octane Number (MON) (see section 1.3.3). The octane number of a given fuel is obtained by comparing the compression ratio at which auto-ignition occurs to that of Primary Reference Fuels (PRF), i. e., mixtures of *n*-heptane and *iso*-octane. As CCRs and IDTs are relatively easy to obtain, several trials were made to obtain the octane number of fuels from these measures [116–120]. The general problem, however, is that the conditions for the octane numbers are very specific and therefore no exact match has been obtained so far [117, 121]. Another proposed measure is the Octane Index (*OI*), which is a combination of the RON and MON that describes the anti-knock quality of fuels at various operation conditions of the engine.

In addition to these well established investigation methods for fuel reactivity, the Micro Flow Reactor with a controlled temperature profile (MFR) is a relatively recent method that was developed by our group [62, 63]. Spatially separated weak flames can be obtained at very low flow velocities inside the reactor. Weak flames of several fuels with different RONs were shown in Figure 1.7. For all investigated fuels, hot flames existed at regions of high wall temperatures and moved to higher wall temperatures for higher RON. Fuels with RON less or equal than 100 showed an additional blue flame at intermediate wall temperatures. Similar to the hot flames, the blue flames moved to higher wall temperatures for higher RON. For fuels with RON less or equal than 20, an additional cool flame appeared at low

### 3 A novel reactivity index for SI engine fuels by separated weak flames

wall temperatures, which did not show much response to changing octane number. These findings present a strong connection between the fuel reactivity as expressed by the octane number and the appearance and the locations of the separated weak flames. In addition to the weak flame locations, high fuel reactivity was associated with the production of formaldehyde ( $\text{CH}_2\text{O}$ ) and hydrogen peroxide ( $\text{H}_2\text{O}_2$ ) at low wall temperatures [74, 77, 91]. Other studies showed that at elevated pressures, all three weak flames (cool, blue and hot flame) moved to lower wall temperatures [68, 73, 75]. Furthermore, the heat release of the hot flame decreased while that of the blue flame and the cool flame increased. These findings show again the capability of the MFR to investigate fuel reactivity in high detail at various conditions.

Building upon the research of the MFR, this chapter aims to develop a novel index number for fuel reactivity by using separated weak flames. The pressure inside the reactor was chosen as 500 kPa as this is within the pressure range of practical ignition conditions. The equivalence ratio was set to  $\Phi = 1.0$ . As fuels, *iso*-octane, *iso*-pentane, *n*-pentane, *n*-heptane as well as PRF80 and PRF50 were chosen. These fuels cover a wide range of reactivity with RON between 0 and 100 (see Table 3.1.1). For the experiments, a vertical-type MFR was used [122] (see section 2.2.1). With this method, weak flames can be separated spatially and can be analyzed and compared to computational results. While computational results offer quantitative results for the heat release of the weak flames, the experiment only allows for qualitative optical observations. Therefore,  $\text{CH}_2\text{O}$  concentrations were measured in the experiment by Gas Chromatography (GC) as it is a marker species for fuel reactivity. This measurement could then be compared to computational results quantitatively. This method allows for a better understanding of low temperature chemistry and the connection between reactivity, weak flame response

Table 3.1.1: RON of selected fuels.

Fuel	RON
<i>iso</i> -Octane	100.0
<i>iso</i> -Pentane	92.3
PRF80	80.0
<i>n</i> -Pentane	61.7
PRF50	50.0
<i>n</i> -Heptane	0.0

and fuel-inherent properties such as molecular structure.

## 3.2 Method

### 3.2.1 Experimental method

The experimental setup of this study was based on that of the previous investigation of ultra-lean conditions (see section 2.2.1). It employed a vertical-type MFR consisting of a quartz tube with a length of 15 cm and an inner diameter of 2 mm. A pressure regulator was used at the outlet of the reactor to control the pressure up to 500 kPa. In a previous study, the pressure effect on the wall temperature was investigated and it was found to be negligible [73]. Similar to the previous study, the liquid fuels were inserted by a syringe into the heated (373 K) and vacuumed tank, where they evaporated. The partial pressure method was then used to add nitrogen at pressure of up to 600 kPa. Heated digital mass flow controllers were employed to mix the fuel/nitrogen mixture and oxygen before being

### 3 A novel reactivity index for SI engine fuels by separated weak flames

supplied to the quartz tube. The mixing of fuel,  $N_2$  and  $O_2$  was conducted in a manner so that the ratios of  $N_2$  and  $O_2$  in air as well as the equivalence ratio were satisfied. The mass flux into the reactor channel was kept constant at all pressure conditions. Therefore, the inlet flow velocity into the reactor was set to 2.0 cm/s at 100 kPa and to 0.4 cm/s at 500 kPa. These flow velocities ensured the appearance of weak flames. In a previous study, the variation of inlet flow velocity was shown to not influence the weak flame locations [77, 91]. This makes the results comparable at different pressures.

A Nikon D800 digital still camera was used to take weak flame images. The exposure time was set to 300 s and a band-pass filter with a transparent wave length of 432.2 nm and a half-band width of 6.4 nm was used. This allowed for capturing the chemiluminescence of excited  $CH^*$  radicals, which is a good marker for the location of the separated weak flames [69, 77]. Five flame images were taken at each experimental condition and background subtraction was performed. These images were then averaged to improve clarity and to decrease the influence of the luminosity of the external hydrogen flame. Flame locations and the respective wall temperatures could then be extracted from these averaged images. The measurement uncertainty was largest for the cool flame where it was less than 1.5 mm in the spatial dimension or 15 K on the temperature scale. For the blue flame, these values decreased to 1.0 mm and 10 K. These uncertainties were found to be almost independent of the fuel and pressure conditions. These uncertainties are caused by the low luminosity in these regions, which shows a rather high sensitivity to local changes. The uncertainty for the hot flame showed a pressure dependence that increased from less than 2 K and 0.2 mm at a pressure of 100 kPa to 10 K and 1.0 mm at 500 kPa. The reason is again the decreasing luminosity of the hot flame for increasing pressure.

To better investigate the separated weak flames,  $CH_2O$  concentrations were measured

using gas chromatography (GC). In order to measure the  $\text{CH}_2\text{O}$  concentration in the cool flame, the maximum wall temperature was decreased. This prevents the  $\text{CH}_2\text{O}$  to be oxidized in the blue flame and effectively freezes the chemical composition of the cool flame. To achieve the reduced maximum wall temperature, the flow of  $\text{O}_2$  and  $\text{H}_2$  of the external hydrogen burner was reduced while also replacing added air, which contains more  $\text{O}_2$  by pure  $\text{N}_2$ . Through this method, the maximum wall temperature was reduced to 600 K. Further downstream, the temperature rapidly decreased to 393 K, which was chosen to prevent condensation of water vapor at elevated pressure. The exhaust gas was then sampled by a GL Sciences AV-283 and sent to a Shimadzu GC-2014 gas chromatograph with a Thermal Conductivity Detector (TCD). A Porapak T50/80 column was chosen for species separation and helium was used as carrier gas.

### 3.2.2 Computational method

One-dimensional steady computations were performed by a modified Chemkin-Pro PREMIX as was explained in section 2.2.2. The temperature profile of Fig. 2.3 was chosen for computations with a maximum wall temperature of 1300 K. At this condition, the length of the computational domain was set to 15 cm. The pressure conditions were changed between atmospheric pressure of 100 kPa and elevated pressure of 500 kPa. The inlet flow velocity at 373 K was changed accordingly from 2.0 cm/s to 0.4 cm/s in order to assure a constant mass flux.  $\text{CH}_2\text{O}$  mole fractions of the cool flame were calculated by using a temperature profile with a maximum temperature less than 700 K. At this condition, the total length of the computational domain was increased to 17 cm. As the modified KUCRS+FFCM mechanism of the previous chapter (see section 2.3.3) showed good agreement with the experimental results, the KUCRS program [38] was used to generate

a separate reaction mechanism for each fuel. In these reaction mechanisms, the seven hydrogen-oxygen reactions that were discussed in the previous chapter (see section 2.3.3), were replaced by those of the FFCM mechanism [122] as these are important for all hydrocarbon fuels.

## 3.3 Results

### 3.3.1 Experimental weak flame locations

The weak flame images of *n*-heptane and *iso*-octane at  $\Phi = 1.0$  and at pressures between 100 kPa and 500 kPa are shown in Figure 3.3.1. The direction of the flow is from the left of the images to the right. To make comparison between the images easier, the luminosity along the center axis of the tube is given in Fig. 3.3.2. For both fuels and at all pressures, the hot flame was located at the right side, in the region of high wall temperatures. At atmospheric pressure, the hot flame had a circular shape and the center of the flame, i. e., the location of highest luminosity was at a wall temperature of 1085 K in the case of *iso*-octane and at 1046 K in the case of *n*-heptane. For increasing pressure, the shape of the hot flame elongated and the center shifted to lower wall temperatures while the luminosity decreased. For pressures of less than 200 kPa, the hot flame of *iso*-octane was located at higher wall temperatures than that of *n*-heptane. As the pressure was further increased, however, the hot flames of both fuels shifted towards the same position. At the highest pressure of 500 kPa, the hot flame of *n*-heptane was at a wall temperature of 1016 K while that of *iso*-octane was at 1015 K. The blue flame was located at lower wall temperatures than the hot flame for all conditions. As was the case for the hot flame, as the pressure increased, the blue flame was elongated and moved to lower wall temperatures.

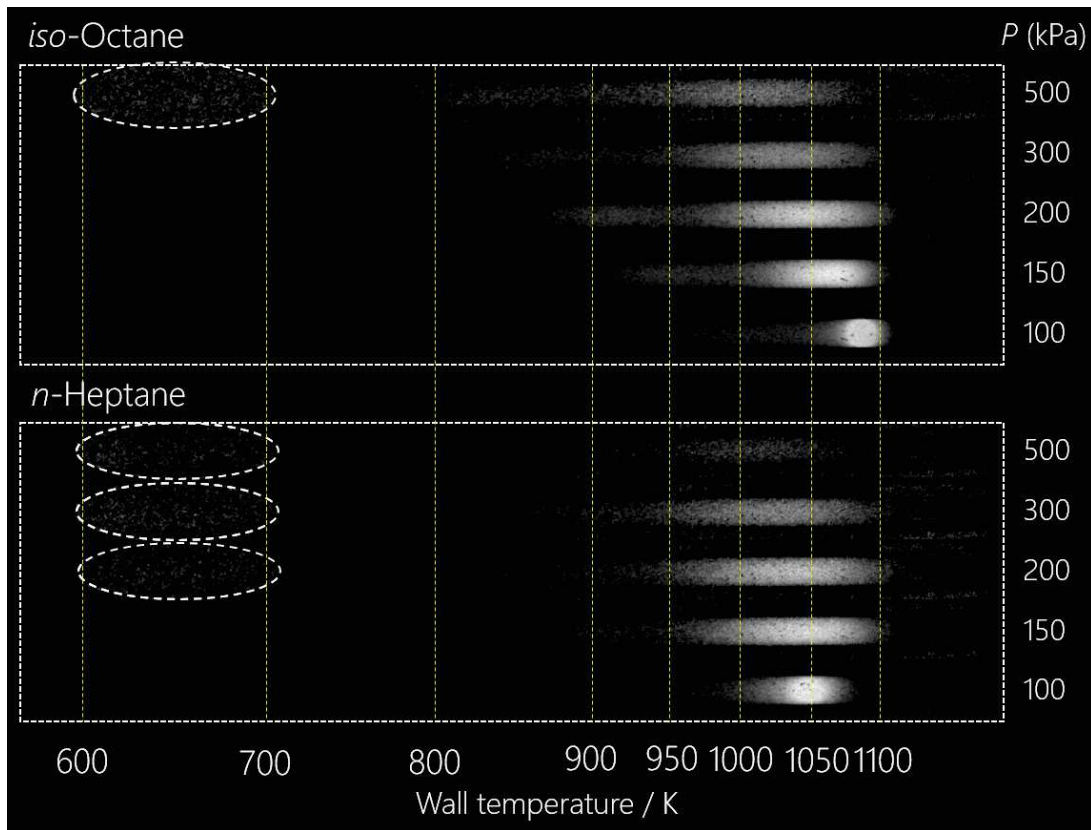


Figure 3.3.1: Weak flame images of *iso*-octane and *n*-heptane at  $\Phi = 1.0$  and pressures between 100 kPa and 500 kPa. These images show the intensity of the blue component of the RGB image after image processing. Note that the brightness of the weak flame region (dashed lines) was enhanced for better visibility.

The center of the luminosity of *iso*-octane moved from 1010 K at a pressure of 100 kPa to 856 K at 500 kPa. In the case of *n*-heptane, the blue flame moved from 911 K at 100 kPa to 838 K at 500 kPa. For both fuels, the shift of the blue flame was about twice as big as that of the hot flame. The cool flame was only visible at elevated pressures at the low temperature side. For *iso*-octane, the cool flame was only observed at 500 kPa with its center at a wall temperature of approximately 660 K. In the case of *n*-heptane, the cool flame appeared at a pressure of 200 kPa at a wall temperature of about 650 K and moved to 620 K at 500 kPa. The existence of cool flames and blue flames at lower wall

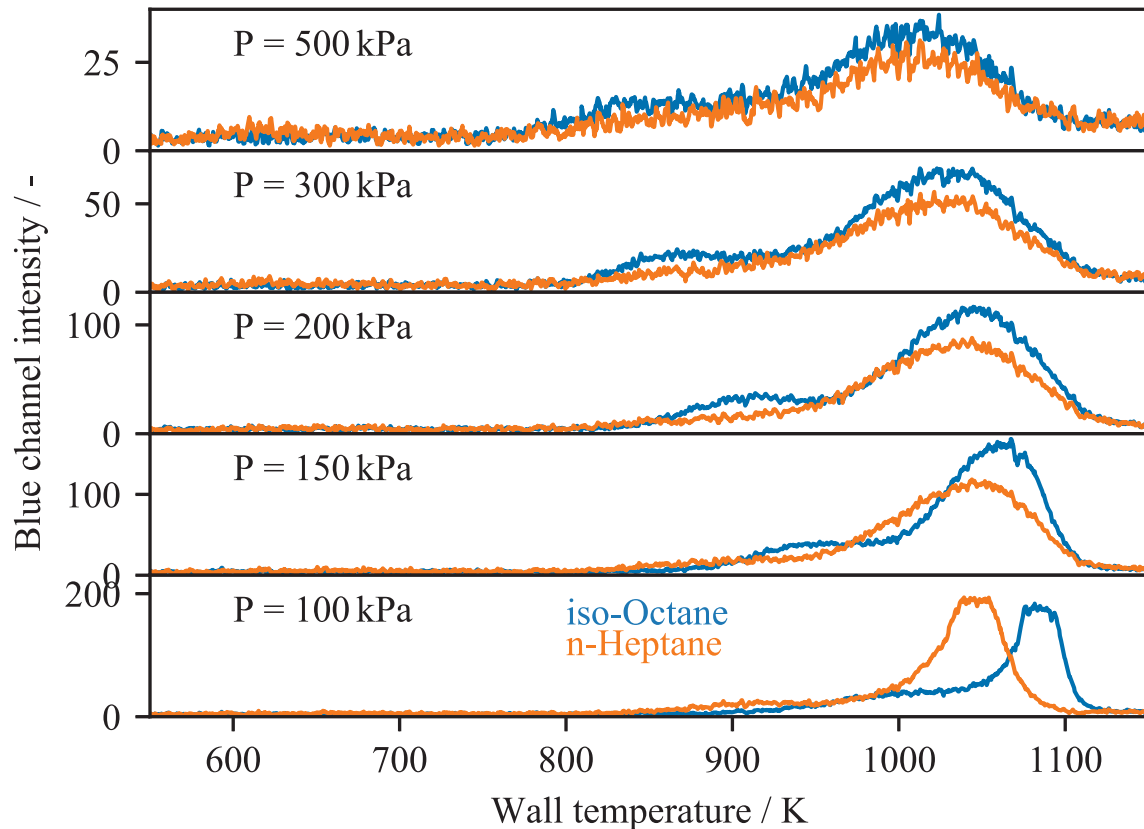


Figure 3.3.2: Intensity along the center of images in Fig. 3.3.1. Note that the scale of the  $y$ -axis changes.

temperatures for  $n$ -heptane indicates higher reactivity than that of  $iso$ -octane. This agrees with the results of previous studies that were shown in Fig. 1.7.

### 3.3.2 Computational weak flame locations

Previous studies showed that the locations of the Heat Release Rate (HRR) peaks corresponds to locations of the CH mole fraction peaks [77]. Based on this relation, the experimental chemiluminescence peaks that are caused by excited  $CH^*$  radicals can be compared to the computational weak flame locations that are based on the heat release rate peaks. It has to be noted, however, that only a comparison of the flame locations but



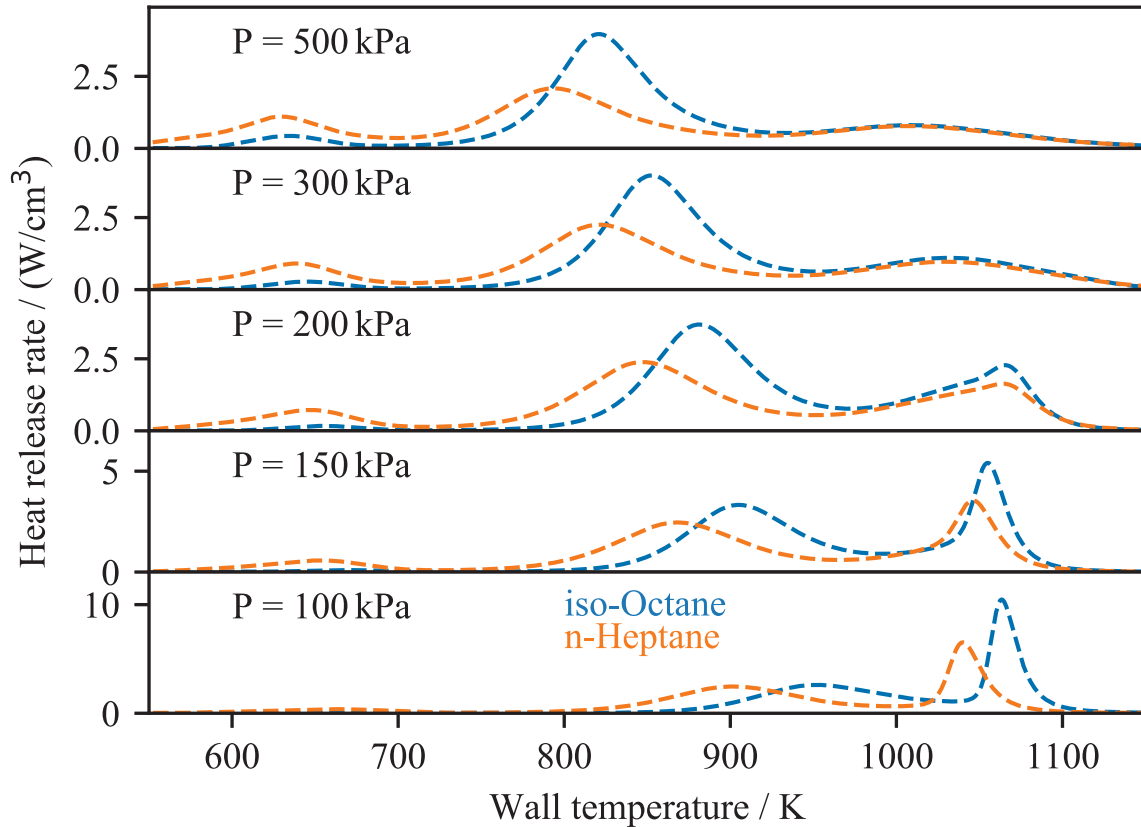


Figure 3.3.3: Computational heat release rate profiles by modified KUCRS of *iso*-octane and *n*-heptane at  $\Phi = 1.0$  and pressures between 100 kPa and 500 kPa. Note that the scale of the  $y$ -axis changes.

not the intensity of the flames is possible.

The computational HRR profiles by the KUCRS+FFCM mechanism for *iso*-octane and *n*-heptane at pressures between 100 kPa and 500 kPa are shown in Fig. 3.3.3. Both fuels show peaks for the cool flame, the blue flame and the hot flame. The peak value of the hot flames decreased for increasing pressure, while the width of the hot flames increased. For *iso*-octane, the peak of the HRR moved from a wall temperature of 1063 K at 100 kPa to 1008 K at 500 kPa. In the case of *n*-heptane, the shift was from 1040 K at 100 kPa to 1007 K at 500 kPa. At 500 kPa, the hot flames of both fuels are almost at the same wall

temperature, which agrees well with the experimental results.

For the blue flame, the peak value of both fuels increased slightly as the pressure increased while the width of the profile became broader. In the case of *iso*-octane, the blue flame moved from 953 K at 100 kPa to 821 K at 500 kPa. The blue flame of *n*-heptane moved from 911 K at 100 kPa to 793 K at 500 kPa. For both fuels, the shifts of the blue flames were larger than those of the other two weak flames, which shows a good agreement with the experiment. Additionally, the peak value of the blue flame of *iso*-octane was higher than that of *n*-heptane for all investigated pressures, which again shows good agreement with the experimental results.

Similar to the blue flame, the peak values of the cool flame increased for increasing pressure and moved to lower wall temperatures. At all pressures, the peaks of *n*-heptane were higher than those of *iso*-octane. For *iso*-octane, the cool flame shifted from 675 K at 100 kPa to 634 K at 500 kPa, while that of *n*-heptane shifted from 662 K at 100 kPa to 630 K at 500 kPa.

#### 3.3.3 Computational flame structure

For a better understanding of the flame structure, the HRR and mole fraction profiles of important species of *iso*-octane at pressures of 100 kPa and 500 kPa are shown in Fig. 3.3.4. With increasing pressure, large parts of the fuel consumption ( $iC_8H_{18}$ ) moved from the blue flame to the cool flame. At 100 kPa, only less than 10 % of the fuels was consumed in the blue flame as compared to more than 50 % at 500 kPa. This increase of fuel consumption in the cool flame led to a higher production of  $CH_2O$  and  $H_2O_2$  and peaks at about 100 K lower wall temperatures. For both pressures, these intermediate species were consumed in the blue flame and CO was produced. CO was then oxidized in the hot flame and  $CO_2$

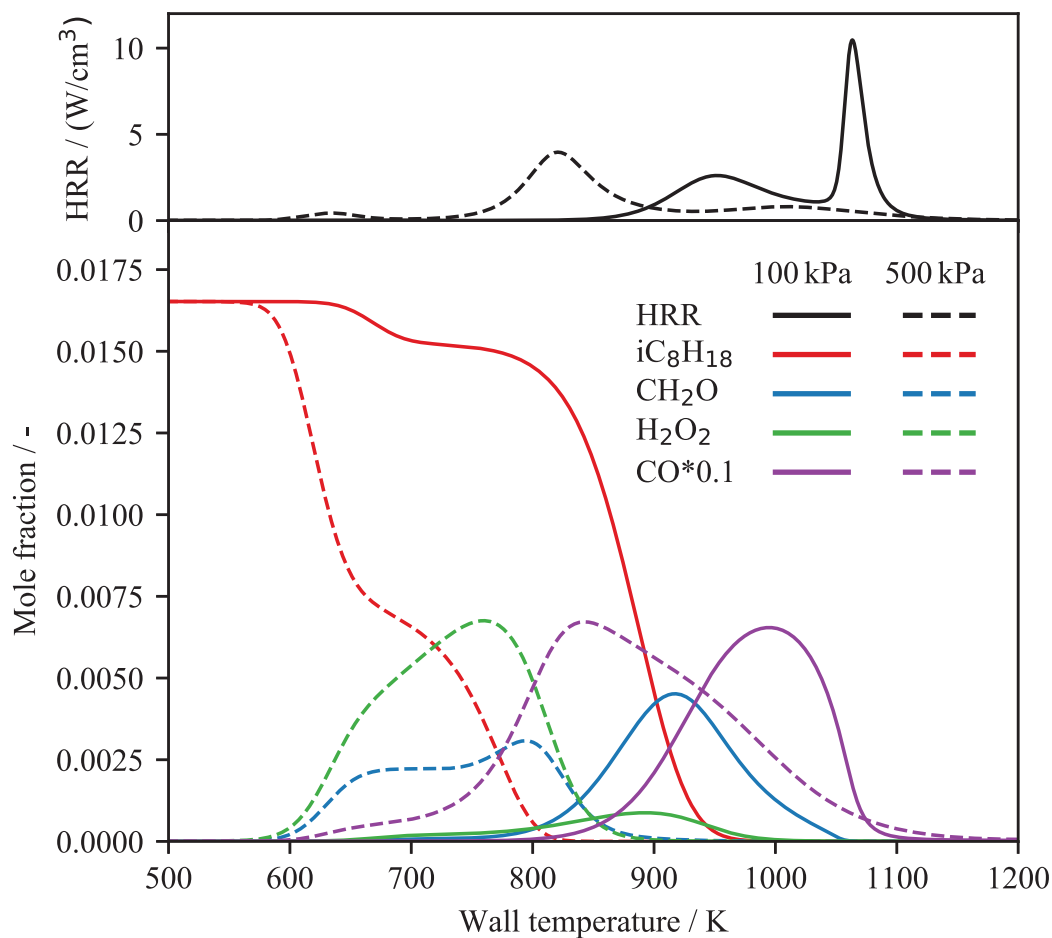


Figure 3.3.4: Computational species profiles by modified KUCRS of *iso*-octane at  $\Phi = 1.0$  and pressures of 100 kPa and 500 kPa.

was formed as the final combustion product. Results of our previous study showed that the oxidation of CO together with the third explosion limit of the H-O system control the hot flame [122]. As the pressure is increased, this causes the mixture to become more reactive, which in turn moves the hot flame to lower wall temperatures.

In the case of *n*-heptane, the species profiles show similar tendencies to those of *iso*-octane (see Fig.3.3.5). As the pressure was increased, the fuel consumption shifted to lower wall temperatures. At 500 kPa, almost all fuel reacted in the cool flame. This also led to higher production of CH<sub>2</sub>O and H<sub>2</sub>O<sub>2</sub> along with higher peak values at lower wall

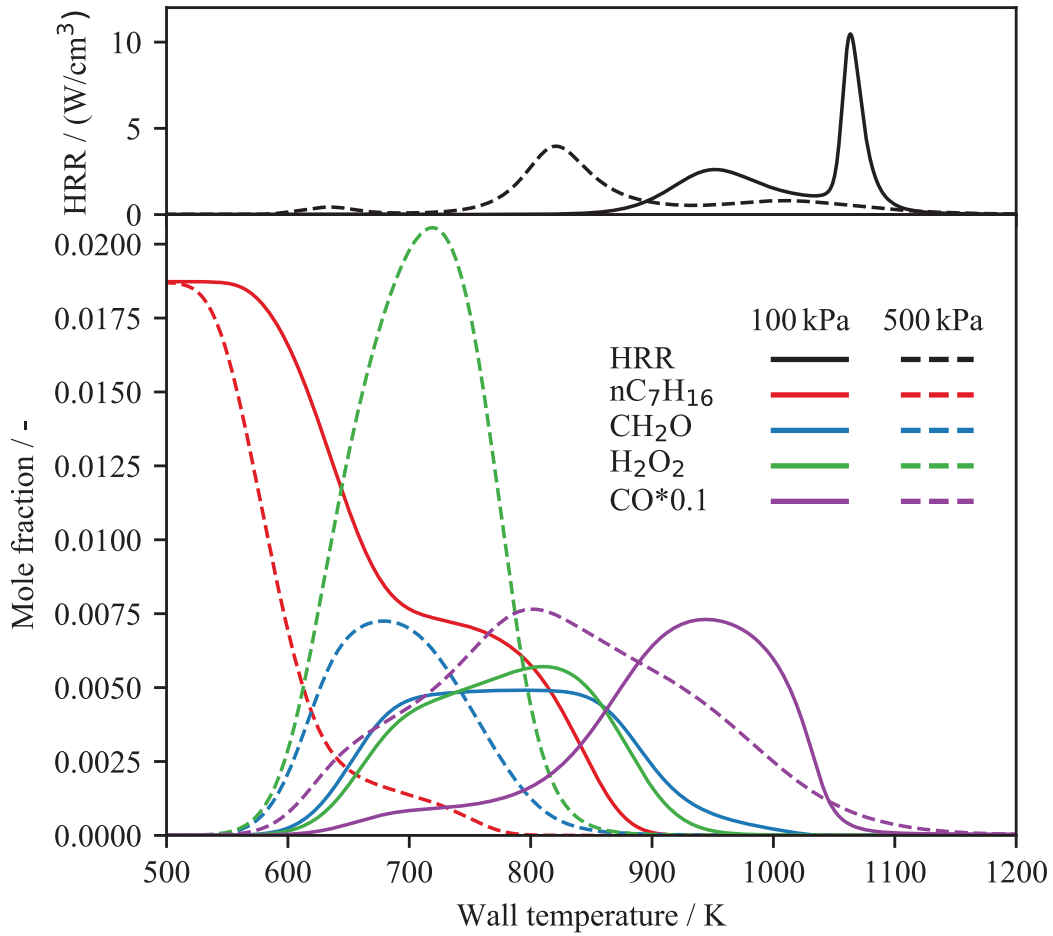


Figure 3.3.5: Computational species profiles by modified KUCRS of *n*-heptane at  $\Phi = 1.0$  and pressures of 100 kPa and 500 kPa.

temperatures of about 700 K. These species were then consumed in the blue flame and CO was formed. The hot flame was again controlled by the H-O system, which increased the reactivity at higher pressure and shifted the hot flame and the CO oxidation to lower wall temperatures.

In addition to the heat release rate profiles of *iso*-octane and *n*-heptane, those of PRF80, PRF50, *iso*-pentane and *n*-pentane are shown in Fig. 3.3.6. Depending on the fuel, the width and the peak value of the heat release rate profile changed significantly. For the cool flame, the peak location was almost independent of the fuel. Here, *n*-heptane and

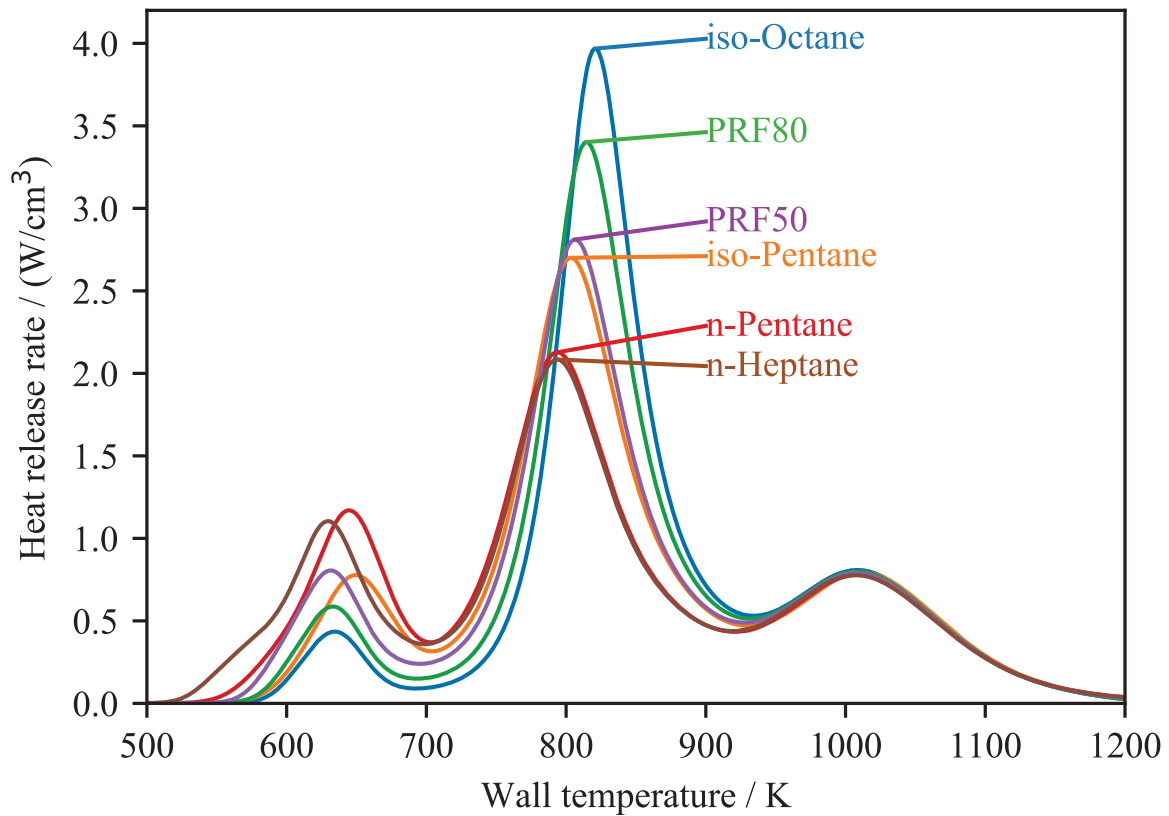


Figure 3.3.6: Heat release rate by modified KUCRS for different fuels at  $\Phi = 1.0$  and 500 kPa.

*n*-pentane experienced the strongest heat release. The other four fuels showed decreasing heat release from *iso*-pentane over PRF50 and PRF80 to *iso*-octane. With the exception of *iso*-pentane and *n*-pentane, this order of the heat release rate showed good agreement with the order of the RON of these fuels (see Table 3.1.1).

At a wall temperature of approximately 700 K, the heat release of all the fuels changed from the cool flame to the blue flame. Similar to the cool flame, the blue flame showed a large variation of the HRR depending on the fuel. Here, fuels that had a low HRR in the cool flame show high values in the blue flame and vice versa. Furthermore, fuels with lower peak values had their peaks located at lower wall temperatures. For *iso*-octane, the

peak was located at a wall temperatures of 821 K, while that of *n*-heptane was at 793 K.

The hot flame did not have evident differences between the fuels with regards to the location and the peak value of the heat release rate. This is caused by the dominance of the H-O system in the hot flame, which is practically independent of the used fuel.

### 3.3.4 Fuel reactivity by heat contribution index

The previous section showed that differences in the HRR profiles exist between fuels of different reactivity. These differences at low, intermediate and high wall temperatures can be quantified by introducing the separated weak flame Heat Contribution Index (HCI) as shown in Eq. 3.1.

$$HCI = \frac{\int_i HRR(x) A_{CS} dx}{\int_{WF} HRR(x) A_{CS} dx} \quad (3.1)$$

In this equation,  $A_{CS}$  refers to the cross section of the reactor channel,  $i$  is the counter of the separated weak flames from the cool flame over the blue flame to the hot flame and WF is summation of all three separated weak flames. The HCI is calculated by dividing the heat release of each weak flame by the total heat release of all three weak flames. The HCI of the cool flame, the blue flame and the hot flame for each fuel are plotted against their RON in Fig. 3.3.7. The Hot flame-HCI has a value of approximately 0.22, which is constant for all the investigated fuels. As was shown in the previous chapter, the hot flame is strongly governed by the H-O system and the oxidation of CO to CO<sub>2</sub> (see section 2.3). As these reactions are independent of the base fuel, the Hot flame-HCI takes the same constant value of 0.22 for all the fuels.

In case of the PRFs, the Blue flame-HCI increases almost linearly with increasing RON from 0.51 for *n*-heptane (RON = 0) to 0.71 for *iso*-octane (RON = 100). On the other hand, the Cool flame-HCI shows to opposite trend and decreases from 0.27 for *n*-heptane

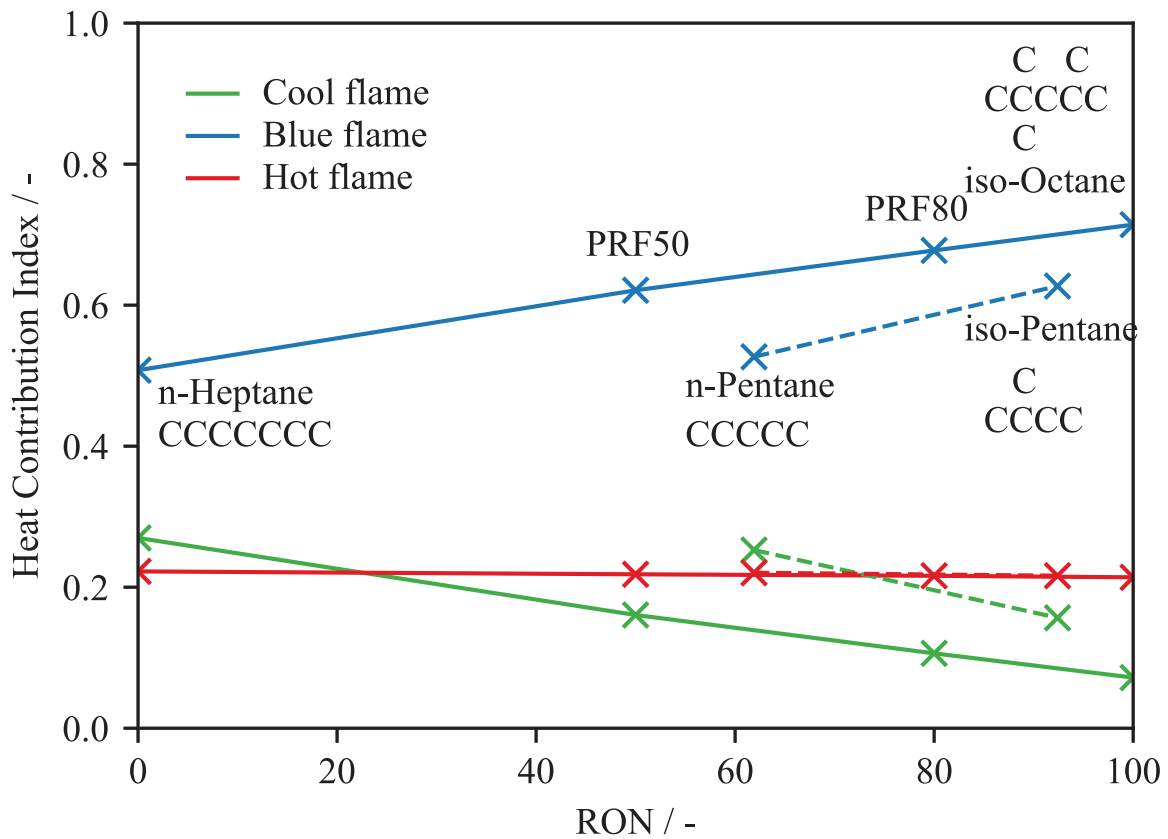


Figure 3.3.7: The heat contribution index of the cool flame, blue flame and hot flame at  $\Phi = 1.0$  and  $P = 500$  kPa plotted over the RON.

to 0.07 for *iso*-octane as the Hot flame-HCI is constant and the sum of all three HCIs for any given fuel is unity. The non-PRF fuels *iso*-pentane and *n*-pentane, however, have Blue flame-HCIs that are lower and Cool flame-HCIs that are higher than the PRFs of the corresponding RON would have. This suggests that the values of HCI do not correspond linearly to the RON. It depends, however, on the molecular structure of each fuel. The structure of *n*-pentane is similar to that of *n*-heptane in that it is a straight-chain alkane. This causes the values of the HCIs to be close to those of *n*-heptane. *iso*-Pentane, on the other hand, is a single branched molecule. This leads to values of the HCIs that are located between those of the straight chain *n*-heptane and triple branched *iso*-octane. As

### 3 A novel reactivity index for SI engine fuels by separated weak flames

the Blue flame-HCI and the Cool flame-HCI were shown to be inverse to each other, solely the Blue flame-HCI will be used to evaluate reactivity in the next part.

In the introduction (see section 3.1, Fig. 3.1.1) it was shown that the molecular structure of the fuel has a strong impact on its reactivity and the Critical Compression Ratio (CCR) [114]. Three main aspects of the fuel structure were found that decrease reactivity and increase the CCR. The first is a shorter main carbon chain of the molecule. The second is a more centralized molecule, i. e., a more highly branched isomer. The third is the addition of methyl groups to the main chain. The comparison of the CCR and the Blue flame-HCI plotted over the carbon atom number in the fuel molecule is shown in Fig. 3.3.8. In case of the CCR, the straight-chain alkanes *n*-heptane and *n*-pentane show the lowest values. The single branched *iso*-pentane shows an intermediate value while the triple branched *iso*-octane has the highest CCR of the investigated fuels. When comparing the CCR to the Blue flame-HCI it can be seen that the relationship to the fuel structure is very similar (see Fig. 3.3.8). Again, the straight-chain alkanes *n*-heptane and *n*-pentane show the lowest values. The single-branched *iso*-pentane is located at intermediate values. The tripe-branched *iso*-octane shows again the highest values. PRF50 and PRF80, which are mixtures of the straight chain *n*-heptane and tripe-branched *iso*-octane, have Blue flame-HCI values that are located between those of the two base fuels.

In the theoretical analysis of the connection between the molecular structure and the CCR it was found that the isomerization reaction  $\text{RO}_2 \rightleftharpoons \text{QOOH}$  (peroxyalkyl radical to alkyl-hydroperoxide radical) is the rate determining step of the ignition at low temperature. The QOOH can then further react with  $\text{O}_2$  to produce  $\text{OOQOOH}$ , which then decomposes to form KOOH (keto-hydroperoxide) and OH. In a following step, KOOH releases another OH. This formation of two OH radicals leads to chain branching at low temperature,



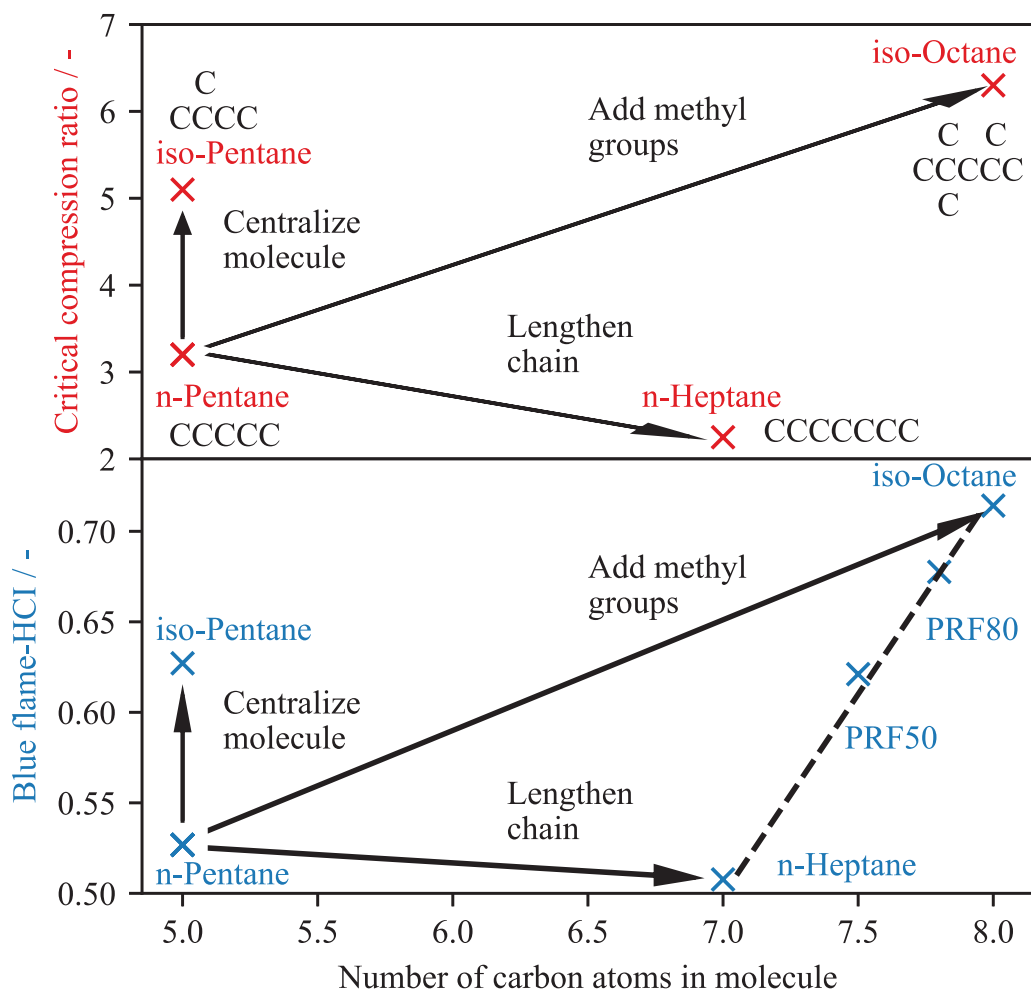


Figure 3.3.8: Critical compression ratio (taken from Lovell [114]) and blue flame index over number of C atoms in molecule.

which largely increases reactivity. The strongest influence on the propensity of the initial isomerization reaction to proceed is the location of OO group (peroxy group) relative to the location from where the H atom is transferred within the molecule. This location is said to be in  $\alpha$ -position if the H atom and the peroxy group are connected by two carbon atoms, in  $\beta$ -position if they are connected by three carbon atoms, in  $\gamma$ -position if they are connected by three carbon atoms and so on. In the transition state from RO to QOOH, the H atom, the carbon atoms in between and the peroxy group form a ring structure.

### 3 A novel reactivity index for SI engine fuels by separated weak flames

They form a five-membered ring if the H atom is in  $\alpha$  position, a six-membered ring if it is in  $\beta$  position, a seven-membered ring if it is in  $\gamma$  position and so on. With increasing ring size, the necessary strain energy that has to be overcome decreases, which enhances this reaction and leads to higher reactivity at lower temperatures. This phenomenon was also investigated by quantum chemistry, which is the basis for the KUCRS reaction mechanism that was used throughout this investigation [38]. This elementary behavior explains the higher reactivity of straight-chain alkanes and the corresponding lower CCR and lower Blue flame-HCI.

Another factor that influences the low-temperature reactivity is the type of bond between C and H atom that has to be broken for the internal H transfer. The highest required energy to break the C-H bond occurs for primary C atom, i. e., C atoms that have only one bond with another C atom and three bonds with H atoms. Lower abstraction energy is required for secondary C atoms, i. e., C atoms that have two bonds with other C atoms as well as two bonds with H atoms. The lowest abstraction energy is required for tertiary C atoms, i. e., C atoms with three bonds to other C atoms and only one bond to an H atom. These characteristics further improve the understanding of fuel reactivity. For long carbon chains, the number of secondary C atoms in the fuel increases, which enhances low-temperature isomerization. In the case of *n*-heptane, the five secondary sites can be in up to  $\delta$  position to each other. This configuration explains *n*-heptane's high reactivity. The other straight chain alkane, *n*-pentane has only three secondary sites that can be in up to  $\beta$  position to each other. This configuration still enables high reactivity but is lower than in the case of *n*-heptane. The effect of centralization can be seen in *iso*-pentane, which is a more centralized isomer of *n*-pentane. Through this isomerization, only one secondary and one tertiary site are available, which are in  $\alpha$  position to each other. On

the one hand, tertiary C atoms have lower abstraction energy of the H atom. On the other hand, only one H atom is available for abstraction. As the tertiary site is in  $\alpha$  position to the secondary site, the strain energy that has to be overcome is high. This leads to higher CCR and Blue flame-HCI of *iso*-pentane as compared to *n*-pentane. The same effects occur for *iso*-octane. It has three methyl groups added to the main chain and, consequently, has the highest values for Blue flame-HCI and CCR of all the fuels.

In the simulations, the Blue flame-HCI can measure the fuel reactivity very well. In the experiment, however, it is not possible to calculate the Blue flame-HCI as the HRR can not be measured directly. In order to make simulations and experiments comparable, another measure was developed. This measure was based on formaldehyde ( $\text{CH}_2\text{O}$ ), as it is an important species at low temperatures and was shown to be a good indicator of reactivity. The  $\text{CH}_2\text{O}$  mole fraction profiles of the computations by the modified KUCRS mechanism at 500 kPa are shown in Fig. 3.3.9 for all investigated fuels. At a wall temperature of 670 K, large differences appear between the peaks of the fuels. This temperature range was shown to be the location of transition from the cool flame to the blue flame (see Fig. 3.3.6).

The HCI was calculated by the integration of HRR over each of the separated weak flames. The  $\text{CH}_2\text{O}$  mole fraction can be viewed as the integration of the production of  $\text{CH}_2\text{O}$ . By taking the  $\text{CH}_2\text{O}$  mole fraction at the end of the cool flame, the FormAldehyde Index (FAI) can be calculated that is similar to the HCI. To make the FAI comparable to the HCI, it has to have values between 0 and 1. This can be achieved by dividing the  $\text{CH}_2\text{O}$  mole fraction of a given fuel by that of *n*-heptane as it shows the highest value of all. As the mole fraction in the cool flame corresponds to the Cool flame-HCI and as the Cool flame-HCI and the Blue flame-HCI are inverse to each other, the  $\text{CH}_2\text{O}$  mole fraction is

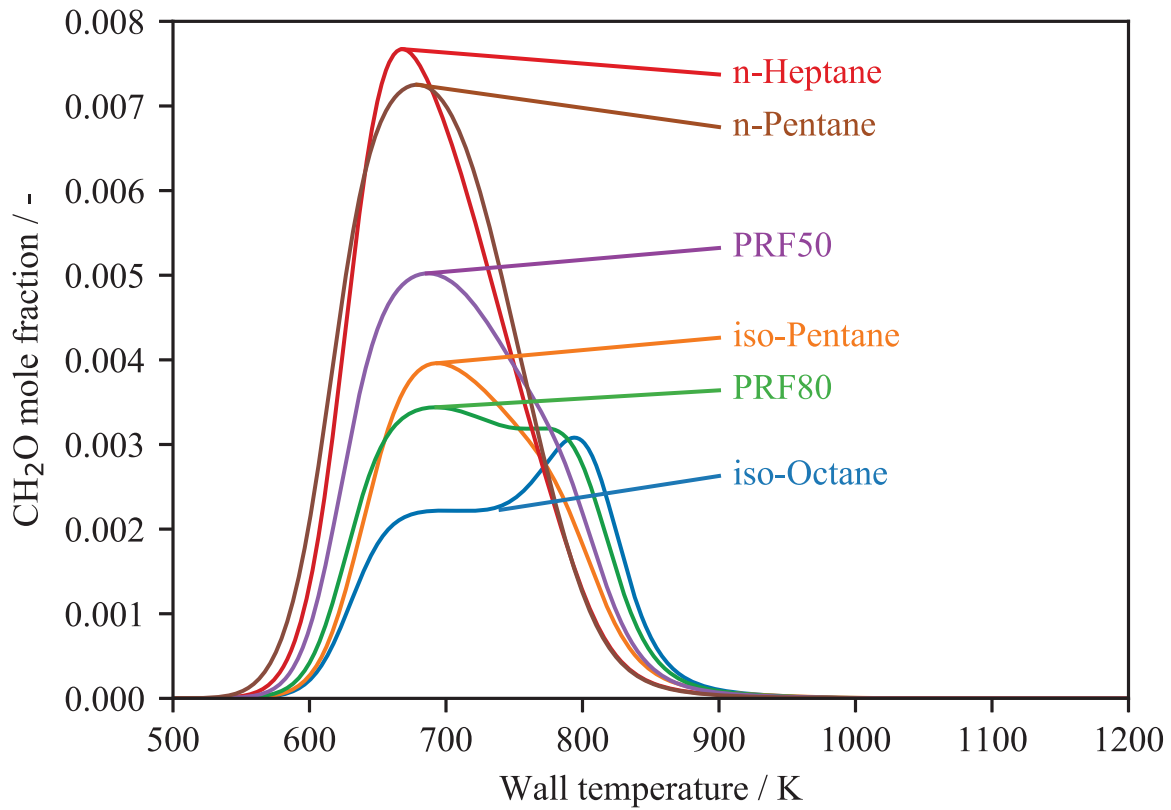


Figure 3.3.9: CH<sub>2</sub>O mole fraction profiles as obtained by modified KUCRS at  $\Phi = 1.0$  and  $P = 500$  kPa.

subtracted from 1 to make it correspond to the Blue flame-HCI. The FAI can then be calculated by Eq. (3.2).

$$FAI = 1 - \frac{x_{\text{CH}_2\text{O}}}{x_{\text{CH}_2\text{O}, n\text{-heptane}}} \quad (3.2)$$

The FAI and the Blue flame-HCI of the six investigated fuels as calculated by the modified KUCRS mechanism are shown in Fig. 3.3.10 (the experimental values will be discussed later). *n*-Heptane has the lowest FAI that is per definition zero. The other straight chain alkane, *n*-pentane, has a FAI that is only slightly higher. This agrees well with the trend of the CCR and the Blue flame-HCI. Its single branched isomer *iso*-pentane has an intermediate FAI, while that of *iso*-octane is the highest. This trend again agrees

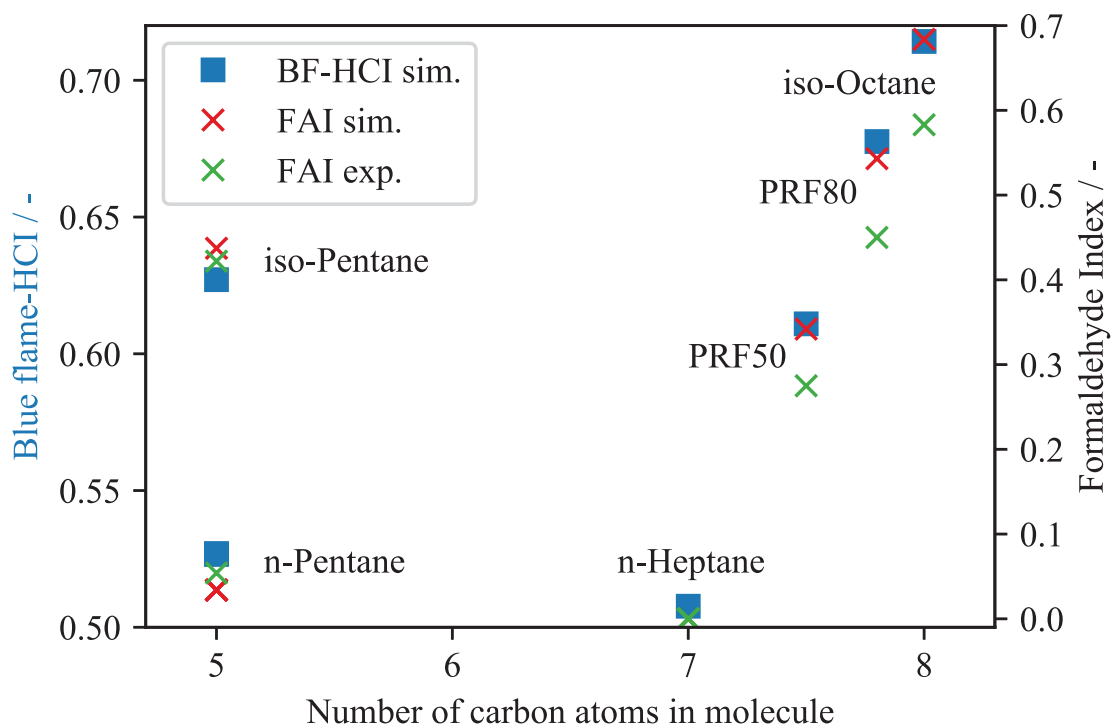


Figure 3.3.10: Blue flame index and formaldehyde index for simulation and experiment over number of carbon atoms in molecule.

very well with the CCR and the Blue flame-HCI. The mixtures of *iso*-octane and *n*-heptane, PRF 80 and PRF50, show FAIs that are located between those of the base components. For all investigated fuels, FAI shows a very good agreement with the Blue flame-HCI as well as with the CCR. It was therefore decided, to calculate FAI by measuring  $\text{CH}_2\text{O}$  experimentally.

The GC measurements of  $\text{CH}_2\text{O}$  were conducted by using a wall temperature profile of the MFR with a lower maximum wall temperature. The measured  $\text{CH}_2\text{O}$  areas for *n*-heptane at a pressure of 500 kPa are shown in Fig. 3.3.11 for maximum wall temperatures between 615 K and 650 K. For each maximum wall temperature, the values of five measurements were averaged. The peak value was found at 630 K and showed a low measurement uncertainty of less than 5%. Therefore, the measurement of the  $\text{CH}_2\text{O}$  area

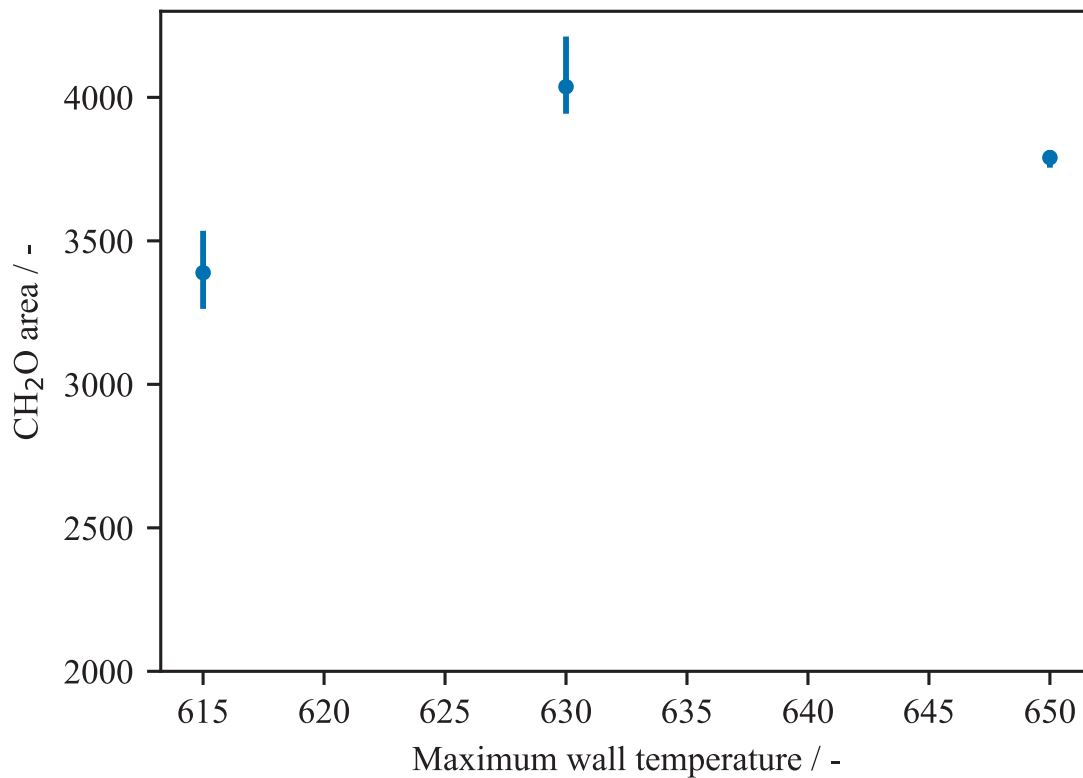


Figure 3.3.11: Measured CH<sub>2</sub>O area and error bars of *n*-heptane over maximum wall temperature at 500 kPa.

of all investigated fuels was conducted with a maximum wall temperature of 630 K.

Along with the computational values of the Blue flame-HCI and the FAI, the experimental FAI is shown in Fig. 3.3.10. As the FAI of *n*-heptane is per definition zero, it is the same in the experiment and in the simulation. The two pentane isomers also show very good agreement between the experimental and the computational values. The experimental value of FAI for *iso*-octane is the highest among all the fuels but is lower than the computational value. This indicates that the KUCRS mechanism slightly under-predicts the *iso*-octane reactivity. As PRF80 and PRF50 contain *iso*-octane, this under-prediction also applies for them. In general, the agreement between the results of the experiment and those of the simulation are in good agreement.

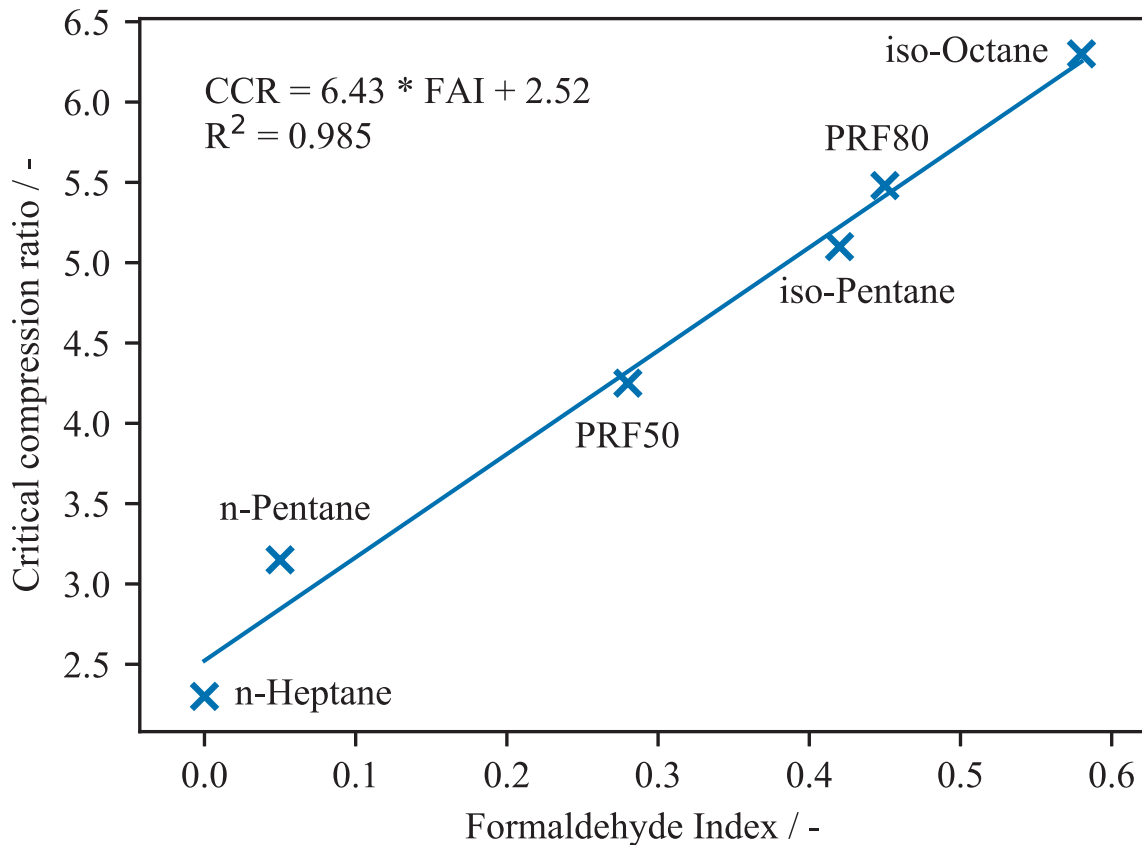


Figure 3.3.12: Estimation of the linear relationship between experimental formaldehyde index and critical compression ratio as taken from Lovell [114].

In Fig. 3.3.7, no clear correlation was found between the RON and the HCl. For FAI, however, a correlation exists with the CRR and is shown in Fig. 3.3.12. The correlation is linear and with low variation. Both measures are controlled by the same low-temperature isomerization reaction  $\text{RO}_2 \rightleftharpoons \text{QOOH}$  and the following chain branching mechanism, which leads to the good agreement between them. These results show the potential of the MFR in the measurement of fuel reactivity in an easy to use and comprehensive way.

## 3.4 Conclusions

In this chapter, a vertical-type Micro Flow Reactor with a controlled temperature profile (MFR) was employed to study the reactivity of *iso*-octane, PRF80, PRF50, *iso*-pentane, *n*-pentane and *n*-heptane by spatially separated weak flames. Investigations were carried out at stoichiometry and at a constant pressure of 500 kPa. Under these conditions, low-temperature reactions were enhanced, while reactions at high temperatures were independent of the base fuel. By analyzing the heat release rate, the Blue flame Heat Contribution Index (Blue flame-HCI) was created. It is the ratio of heat release in the blue flame to the total heat release throughout the MFR. This Blue flame-HCI was found to well describe the reactivity of the investigated fuels. It is strongly dependent on the molecular structure of the fuel. This dependency on the fuel structure is governed by low-temperature chain branching reactions that strongly depend on the initial isomerization reaction  $\text{RO}_2 \rightleftharpoons \text{QOOH}$ . This reaction is stronger for long straight-chain alkanes than for shorter and branched isomers. This can be seen in the higher reactivity of the straight-chain *n*-heptane and *n*-pentane as compared to the single-branched *iso*-pentane and the triple-branched *iso*-octane. The Blue flame-HCI showed good agreement with the critical compression ratio (CCR) of the investigated fuels. This agreement is based on the same low-temperature isomerization and chain branching. As the heat release of the hot flame was constant for all fuels, the Cool flame-HCI and the Blue flame-HCI were inverse to each other. Therefore, the  $\text{CH}_2\text{O}$  concentrations in the cool flame were measured in the experiment by gas chromatography and the FormAldehyde Index (FAI) was developed. The FAI was again dependent on the molecular structure of the fuel and its trends agreed well with those of the Blue flame-HCI. Furthermore, while no direct correlation with the



RON was found, the FAI showed a linear correlation with the CCR. Based on these results, the MFR offers the possibility to investigate fuels reactivity in an easy to use way by using separated weak flames.



# Appendix

## 3.A Cool flame temperature profile

Figure 3.A.1 shows the measured temperature profile with  $T_{\max} = 723$  K at 500 kPa and  $\Phi = 1.0$  together with the corresponding cool flame image. The beginning of the

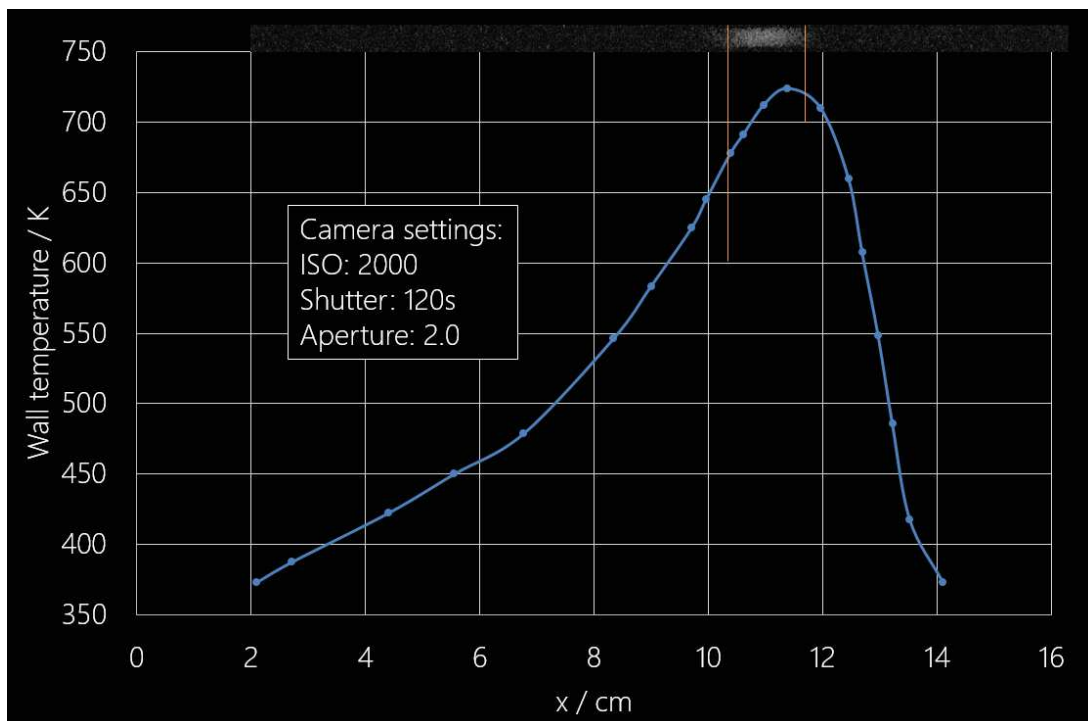


Figure 3.A.1: Wall temperature profile with  $T_{\max} = 723$  K and image of *iso*-octane cool flame at 500 kPa and  $\Phi = 1.0$ .

### 3 A novel reactivity index for SI engine fuels by separated weak flames

temperature profile is very similar to that of  $T_{\max} = 1300$  K. Contrary to the larger profile, however, the decreasing part behind the maximum is important too. As the cool flame produces intermediate products, these can still react even if the temperature is decreasing. In the presented case of  $T_{\max} = 723$  K, the temperature was still too high and the  $\text{CH}_2\text{O}$  concentration decreased as it reacted behind the cool flame. Therefore, in the main part of this chapter, the maximum wall temperature was reduced to 630 K.

## 3.B Fuel structure and HCl

Figure 3.B.1 shows the relationship between molecular structure and the Blue flame-HCl in more detail. The fuels are separated into three groups. In all groups, the first H atom

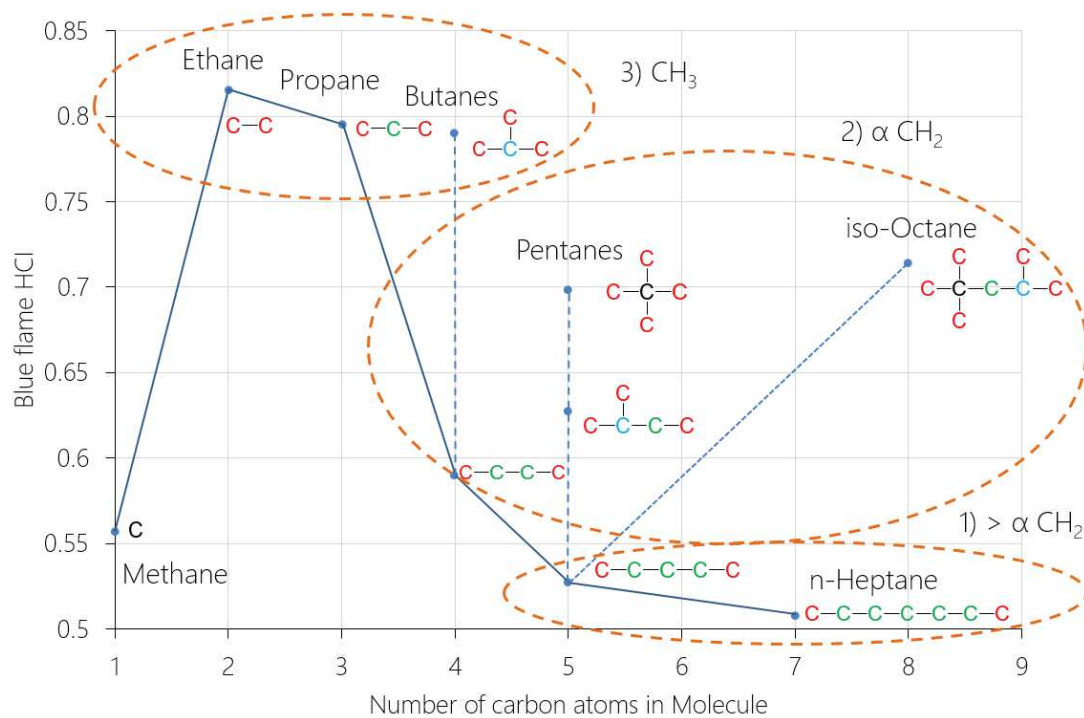


Figure 3.B.1: Relationship between fuel structure and Blue flame-HCl. Primary carbon atoms are colored red, secondary carbon atoms are colored green and tertiary carbon atoms are colored blue.

abstraction is most likely to happen at a tertiary site (blue), then at a secondary site (green) and lastly on a primary site (red). The most reactive fuels have a Blue flame-HCI between 0.5 and 0.55. These fuels have in common that after the first H atom is abstracted from a secondary site, another H atom at another secondary site is likely to be in  $\beta$  position or higher, i. e., separated by more than one carbon atom. This results in a low energy barrier for internal H transfer of the isomerization reaction  $RO_2 \rightleftharpoons QOOH$ , which leads to subsequent chain branching and higher reactivity.

Fuels in the intermediate group, however, have only have secondary C atoms in  $\alpha$  position, i. e., as direct neighbors. This makes isomerization more difficult and reduces reactivity.

The last group does not have secondary C atoms but only primary C atoms in  $\alpha$  position to the site, where the first H abstraction is most likely to occur. This, in turn, reduces the reactivity even more as the strain energy that has to be overcome is greatly increased. These results show a clear relationship between chemical structure on an elementary level to a macro phenomenon such as the blue flame.

### 3.C HCI of lean mixtures

The comparison of the HCIs for stoichiometric and ultra-lean conditions is shown in Fig. 3.C.1 for PRF0 to PRF100, S3R (RON=90) and Toluene (RON=120). The equivalence ratio has the biggest effect for fuels with low RON, i. e., fuels with high reactivity. While the changes are less than 0.04, the biggest effect occurs for the blue flame, which gets enhanced. The cool flame and the hot flame, however, reduce their HCI. For fuels with higher RON, the trend is the same while the absolute changes are smaller. These results

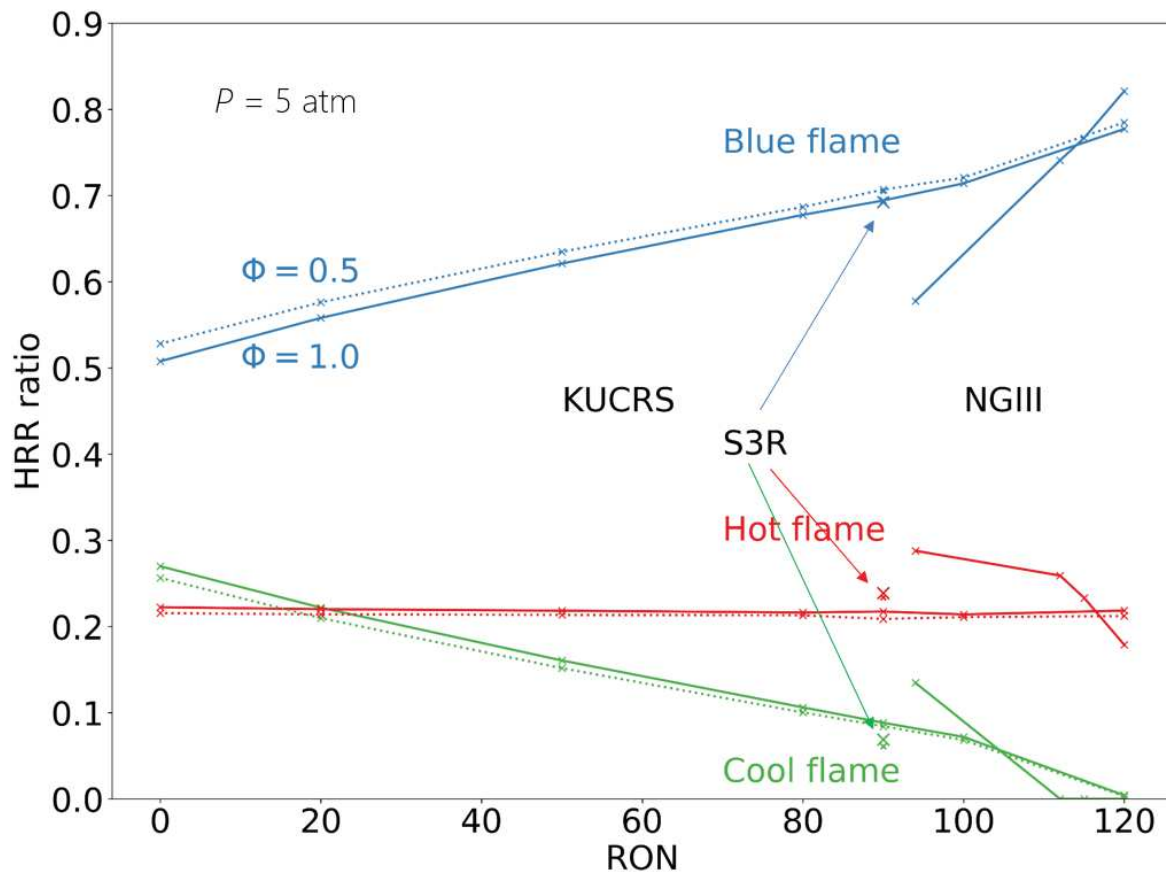


Figure 3.C.1: Heat contribution indexes of PRF0-100, S3R and Toluene at  $P = 500$  kPa and  $\Phi = 1.0$  and  $0.5$ .

shows that ultra-lean conditions reduce reactivity by shifting heat release from the cool flame to the blue flame.

### 3.D HCI of other fuels

Fig. 3.D.1 shows an extended comparison of the critical compression ratio and Blue flame-HCI of various alkanes. Similar to the results that were presented in the main part, the agreement between these two measures is very high. As the main carbon chain gets longer, low temperature isomerization is enhanced and the fuels become more reactive. This is shown by their lower CCR and Blue flame-HCI. On the other hand, as the molecules

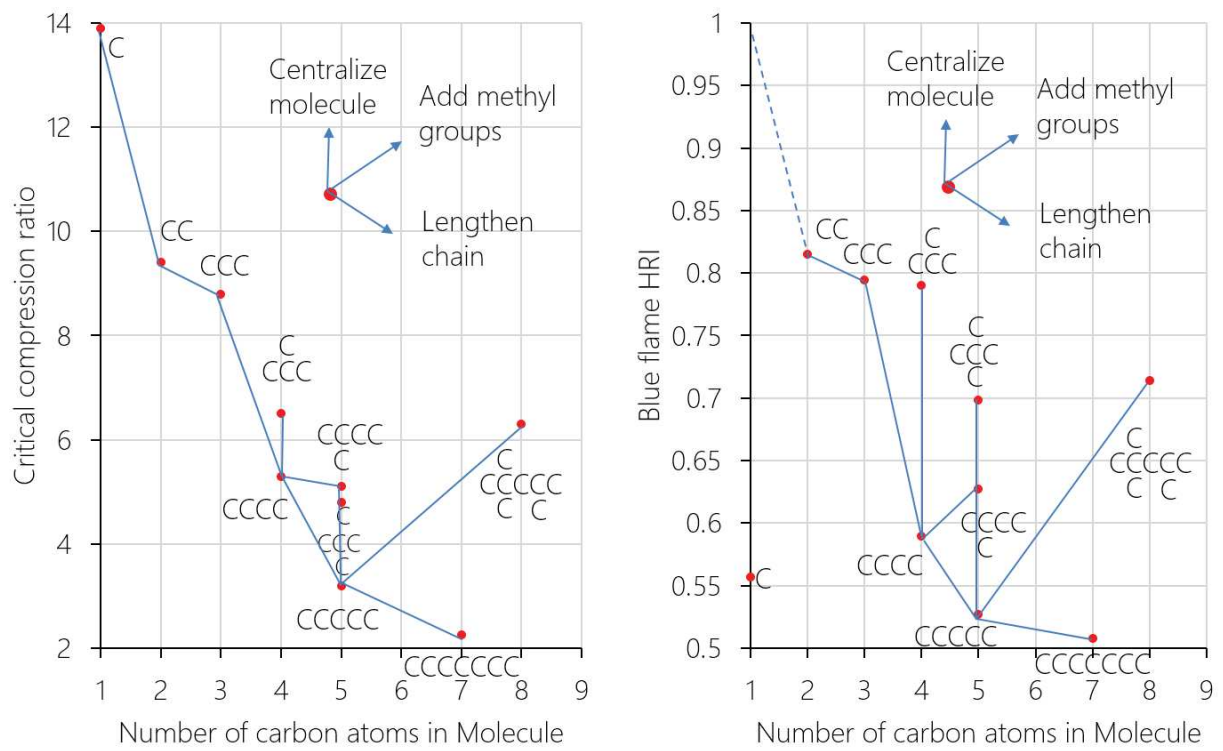


Figure 3.D.1: Comparison of critical compression ratio [114] on the left side and Blue flame-HCl by modified KUCRS for various fuels at 500 kPa and  $\Phi = 1.0$  on the right side.

become more centralized or as methyl groups are added, low temperature isomerization is limited and the reactivity decreases.





# **4 Investigation of the chemical and dilution effects of major EGR constituents on the reactivity of PRF by weak flames in a micro flow reactor with a controlled temperature profile**

## **4.1 Introduction**

Exhaust gas recirculation (EGR) is a measure that can decrease the maximum combustion temperature in internal combustion engines (see section 1.2.2). Lower maximum combustion temperatures decrease  $\text{NO}_x$  emissions, decrease thermal losses and thereby increase thermal efficiency and decrease fuel consumption and  $\text{CO}_2$  emissions. EGR has three main effects, namely the thermal effect, the dilution effect and the chemical effect (see section 1.2.2).

#### 4 The chemical and dilution effects of EGR on the reactivity of PRF

The first effect, the thermal effect is due to the higher heat capacity of chemical species that are recirculated, e. g., CO<sub>2</sub> and H<sub>2</sub>O, than that of air. This decreases the maximum combustion temperature, which in turn decreases thermal losses and NO<sub>x</sub> emissions. The second effect, the dilution effect is based on reduced O<sub>2</sub> and fuel concentrations as they are partly replaced by exhaust gas. This concentration reduction was shown to cause increased Ignition Delay Times (IDTs) [20, 26, 27]. The third effect, the chemical effect, on the other hand, is caused by increased concentrations of exhaust gas species, such as CO<sub>2</sub> and H<sub>2</sub>O. These species have high third body efficiencies and can act as collision partners in three-body reactions, which they then enhance. Furthermore, their increased concentrations can lead to shifts of the chemical equilibrium of important reactions, i. e.,

$$\text{CO} + \text{OH} \rightleftharpoons \text{CO}_2 + \text{H}.$$

Our group previously performed a study, in which the effect of the EGR species CO<sub>2</sub>, H<sub>2</sub>O and N<sub>2</sub> on the reactivity of syngas/air mixtures was investigated by using a horizontal-type Micro Flow Reactor with a controlled temperature (MFR) [76]. Here, it was found that H<sub>2</sub>O has the strongest inhibiting effect on the hot flame through the promotion of the chain-termination reaction  $\text{H} + \text{O}_2 (+ \text{M}) \rightleftharpoons \text{HO}_2 (+ \text{M})$ . Despite cool flames and blue flames being absent for syngas/air weak flames at atmospheric pressure, the results for the hot flame showed that the MFR allows for a clear separation of the dilution effect and the chemical effect from the thermal effect.

In order to examine the effect of the EGR constituents N<sub>2</sub>, CO<sub>2</sub> and H<sub>2</sub>O not only on the hot flame but also on the cool flame and the blue flame, the two components of Primary Reference Fuels (PRF), *iso*-octane (PRF100) and *n*-heptane (PRF0), were used in this study. The pressure was increased up to 500 kPa, as this is in the range of the pressure at ignition timing in SIP gasoline engines. The equivalence ratio was set to

$\Phi = 1.0$ . Experiments and steady one-dimensional computations were conducted for the given conditions. As the pressure inside the MFR is increased, the separated weak flames shift to lower wall temperatures. The agreement between experiments and simulations for these high-EGR conditions are discussed. Furthermore, as the pressure is increased, larger portions of the heat release shift from the hot flame to the blue flame and the cool flame [73, 75, 123]. This effect was used in our previous study to introduce a novel reactivity index, the Heat Contribution Index (HCI), which is based on the heat release rate [123]. In the current study, the HCI will be used to quantify the effect of EGR-like dilution on the reactivity of PRF/air mixtures.

## 4.2 Method

### 4.2.1 Experimental method

Similar to the previous chapters, a vertical-type micro flow reactor with a controlled temperature profile (MFR) was used in the experiment to investigate spatially separated weak flames. The MFR was discussed in more detail in section 2.2.1 and a scheme can be seen in Fig. 2.2. Similar to the previous chapters, the reactor channel had a length of 15.0 cm and an inner diameter of 2.0 mm. The wall temperature profile had values between 373 K and 1300 K and was shown in Fig. 2.3. A pressure regulator was used to control the pressure inside the tube between 100 kPa and 500 kPa. The fuel/air/EGR mixture preparation was done in a heated tank at a temperature of 373 K. A syringe was used to insert the liquid fuels into the tank. The tank was then filled by the partial pressure method with  $N_2$ ,  $CO_2$  and/or  $H_2O$  according to the EGR dilution conditions. Partial

#### 4 The chemical and dilution effects of EGR on the reactivity of PRF

pressures were used to calculate the dilution ratio of the EGR conditions by Eq. (4.1).

$$x_{\text{dil}} = \frac{P_{\text{dil}}}{P_{\text{fuel}} + P_{\text{air}} + P_{\text{dil}}} \quad (4.1)$$

The dilution ratios were set as 0 %, 20 % and 50 %. The maximum pressure of the tank was set to 600 kPa. Only in the case of H<sub>2</sub>O dilution, it was set to 300 kPa and H<sub>2</sub>O was only added up to 20 % to prevent condensation. Digital mass flow controllers were then used to combine the fuel/N<sub>2</sub>/EGR mixture with O<sub>2</sub> in accordance with the equivalence ratio, the dilution ratio and the O<sub>2</sub> to N<sub>2</sub> ratio in air. This combined mixture was then inserted into the MFR at a temperature of 373 K to prevent condensation. For all pressure conditions, the mass flux was kept constant, with an inlet flow velocity of 2.0 cm/s at 100 kPa and 0.4 cm/s at 500 kPa. For weak flames, changes of the inlet flow velocity only have a negligible effect on the flame locations [69, 77]. A Nikon D800 digital still camera with an attached CH-filter was used to capture images of the weak flames. The average of five images was calculated for each case with additional background subtraction. In the analysis of the images, only the blue channel of the RGB images was used as the images were taken through a 431 nm band-pass filter, which only lets light of the blue spectrum pass. In these weak flame images, the locations and luminosity of the cool flame, the blue flame and the hot flame were extracted. Especially at elevated pressures and high dilution ratios, the noise-to-signal ratio gets high. Therefore, low-pass filtering was used to better extract the locations of the luminosity peaks that correspond to the separated weak flames. After all these steps, the uncertainty with regards to the wall temperature at the location of the weak flames was within ±15 K in case of the cool flame, ±10 K in case of the blue flame and ±2 K in case of the hot flame. Previous MFR studies assumed that the chemiluminescence was primarily caused by excited CH\* radical. The photon emission

from  $\text{CH}^*$  radical, however, overlaps with the broad-band emission of excited  $\text{CO}_2^*$  [124]. To account for this additional source of chemiluminescence, both sources were considered in this chapter.

### 4.2.2 Computational method

The one-dimensional, steady simulations of the MFR were conducted by a modified Chemkin-Pro PREMIX [92] (see section 2.2.2 for more details). The wall temperature profile was taken from Eq. (2.1). Adaptive grid spacing was used on a total domain of 15 cm with a minimum grid size of 50  $\mu\text{m}$  in the region of the hot flame. Values of other conditions, such as the inlet flow velocity and the pressure, were taken from experiment. The modified KUCRS mechanism was used for both fuels [38, 122]. Additionally, computations were done by the LLNL PRF mechanism for comparison [32]. The results by LLNL, however, did not show good agreement with the experiment and were therefore moved to the appendix 4.A. Previous MFR studies used the peak locations of the Heat Release Rate (HRR) as an indicator of the locations of the separated weak flames. At atmospheric pressure, the locations of the HRR peaks agreed well with the peaks of the concentration of CH radicals [77]. These chemiluminescence was assumed to be mainly dependent on this concentration. The actual photon emission, however, does not directly originate from the CH radicals but rather from the quenching of excited  $\text{CH}^*$  radicals. Furthermore, chemiluminescence with a wavelength of approximately 431 nm can also originate from excited  $\text{CO}_2^*$ . Therefore, the HRR-based approach will be evaluated again and the chemiluminescence from the quenching of excited  $\text{CH}^*$  and  $\text{CO}_2^*$  will be investigated. The reactions that govern the formation and quenching of excited  $\text{CH}^*$  are given in Table 4.2.1. When a local steady-state is assumed, the  $\text{CH}^*$  concentration can be calculated by Eq. (4.2),

Table 4.2.1: Chemiluminescence reactions used to model CH\* formation and quenching.

	Reaction	$A$	$b$	$E$	Ref
R6	$\text{C}_2\text{H} + \text{O} \rightleftharpoons \text{CH}^* + \text{CO}$	6.023E+12	0.0	457.0	[125]
R7	$\text{C}_2\text{H} + \text{O}_2 \rightleftharpoons \text{CH}^* + \text{CO}_2$	6.023E-04	4.4	-2285.1	[125]
Q1	$\text{CH}^* + \text{H}_2\text{O} \rightleftharpoons \text{CH} + \text{H}_2\text{O}$	5.3E+13	0.0	0.0	[126]
Q2	$\text{CH}^* + \text{CO}_2 \rightleftharpoons \text{CH} + \text{CO}_2$	2.41E-01	4.3	-1694.0	[126]
Q3	$\text{CH}^* + \text{CO} \rightleftharpoons \text{CH} + \text{CO}$	2.44E+12	0.5	0.0	[126]
Q4	$\text{CH}^* + \text{H}_2 \rightleftharpoons \text{CH} + \text{H}_2$	1.47E+14	0.0	1361.0	[126]
Q5	$\text{CH}^* + \text{O}_2 \rightleftharpoons \text{CH} + \text{O}_2$	2.48E+06	2.14	-1720.0	[126]
Q6	$\text{CH}^* + \text{N}_2 \rightleftharpoons \text{CH} + \text{N}_2$	3.03E+02	3.4	-381.0	[126]
Q7	$\text{CH}^* + \text{CH}_4 \rightleftharpoons \text{CH} + \text{CH}_4$	1.73E+13	0.0	167.0	[126]

with  $A$  being the Einstein coefficient of  $1.85 \times 10^{-6} \text{ s}^{-1}$  [124, 125]. The photon emission rate of the chemiluminescence can be calculated as  $i_{\text{CH}^*}$  (mole photons/cm<sup>3</sup>/s) by Eq. (4.3).

$$[\text{CH}^*] = \frac{k_6[\text{C}_2\text{H}][\text{O}] + k_7[\text{C}_2\text{H}][\text{O}_2]}{\sum_j k_j[\text{M}_j] + A} \quad (4.2)$$

$$i_{\text{CH}^*} = A[\text{CH}^*] \quad (4.3)$$

For the excited  $\text{CO}_2^*$ , the global formation reaction is given by Eq. (4.4) [127]. Based on this, the emission rate of photons from quenching  $\text{CO}_2^*$  is directly proportional to the concentrations of CO and O ( $[\text{CO}]$  and  $[\text{O}]$ ) and can be calculated by Eq. (4.5) [128].



$$i_{\text{CO}_2^*} = 3.3(\pm 0.3) \times 10^3 \exp(-2300 \text{ K}/T)[\text{CO}][\text{O}] \quad (4.5)$$

The concentrations of the species in the excited state is much smaller than the non-excited state and, therefore, the calculations of these species can be done in a post-processing step [125].

In the previous chapter, the Heat Contribution Index HCI was introduced as a measure to evaluate fuel reactivity by separated weak flames (see section 3.3.4) [123]. The HCI method will be used in this chapter for the evaluation of the effect of EGR on the reactivity of the separated weak flames.

## 4.3 Results

In the following sections, experimental results are presented and compared to computational results. Based on this, the effect of EGR-like dilution on the reactivity in the MFR is investigated. To this end, the weak flames of *iso*-octane are analyzed first. As *iso*-octane is a fuel with low reactivity, the focus will be on the hot flame and the blue flame. In a next step, a fuel of high reactivity, *n*-heptane, will be examined with an additional focus on the cool flame.

### 4.3.1 Experimental results

The images of the separated weak flames of *iso*-octane at a pressure of 200 kPa with dilution rates of 0 %, 20 % and 50 % by N<sub>2</sub>, CO<sub>2</sub> and H<sub>2</sub>O are shown in Fig. 4.3.1 The blue flame and the hot flame are visible from left to right as two bright zones at all conditions. Chemiluminescence of the cool flame was not observed due to the low reactivity of *iso*-octane, decreased chemiluminescence at higher pressures [122] and the high dilution ratios. For the dilution by N<sub>2</sub>, the length of the blue flame decreased, it moved to higher wall

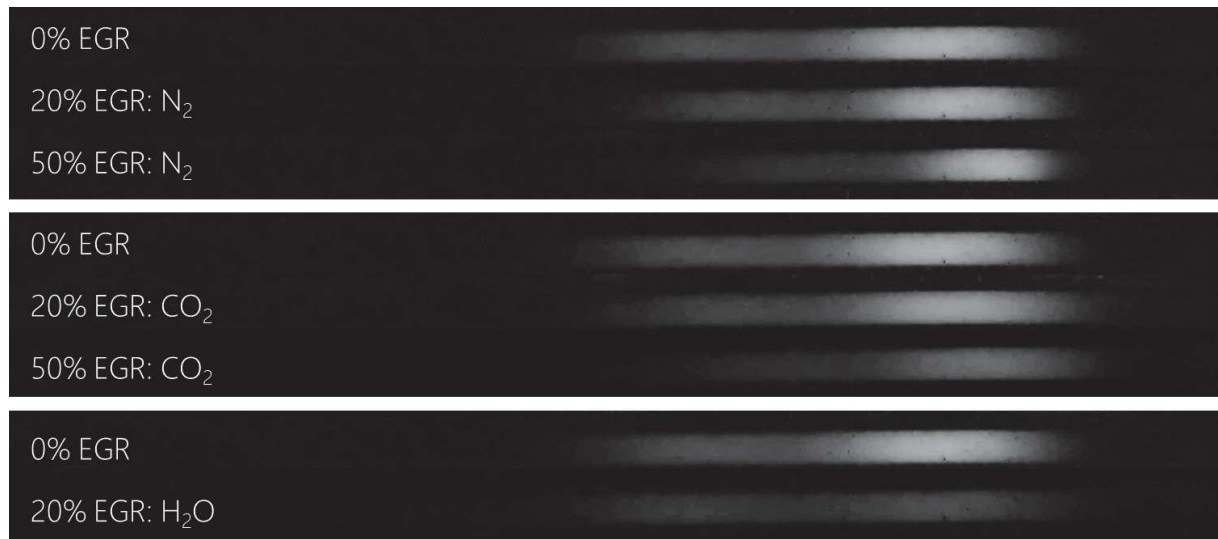


Figure 4.3.1: Weak flame images of *iso*-octane at  $P = 200$  kPa and  $\Phi = 1.0$  for dilution ratios of 0%, 20% and 50% of N<sub>2</sub>, CO<sub>2</sub> and H<sub>2</sub>O (only 20%).

temperatures and its luminosity decreased. The hot flame also decreased in length and moved to higher wall temperatures. For dilution by CO<sub>2</sub>, the response of the blue flame was similar to the case of N<sub>2</sub>, while the hot flame showed lower luminosity but over a wider region. The dilution by H<sub>2</sub>O had no evident effect on the length or the location of the blue flame or the hot flame. It, however, led to a decrease of the luminosity that was stronger than for the dilution by N<sub>2</sub> or CO<sub>2</sub>.

For the dilution by CO<sub>2</sub>, the luminosity profiles along the center axis of the reactor channel as seen in Fig. 4.3.1 are shown in Fig. 4.3.2. For an increase of dilution ratio by CO<sub>2</sub> to 50%, the luminosity decreased by about 50%. Furthermore, the beginning of the blue flame and the hot flame as well as their peak locations shifted to higher wall temperatures. For the blue flame, the shift of its peak was 50 K, while that of the hot flame was 23 K.

The effect of increasing pressure on the weak flames of *iso*-octane for a dilution of 20% by CO<sub>2</sub> is shown in Fig. 4.3.3. For increasing pressure, the blue flame decreased in luminosity



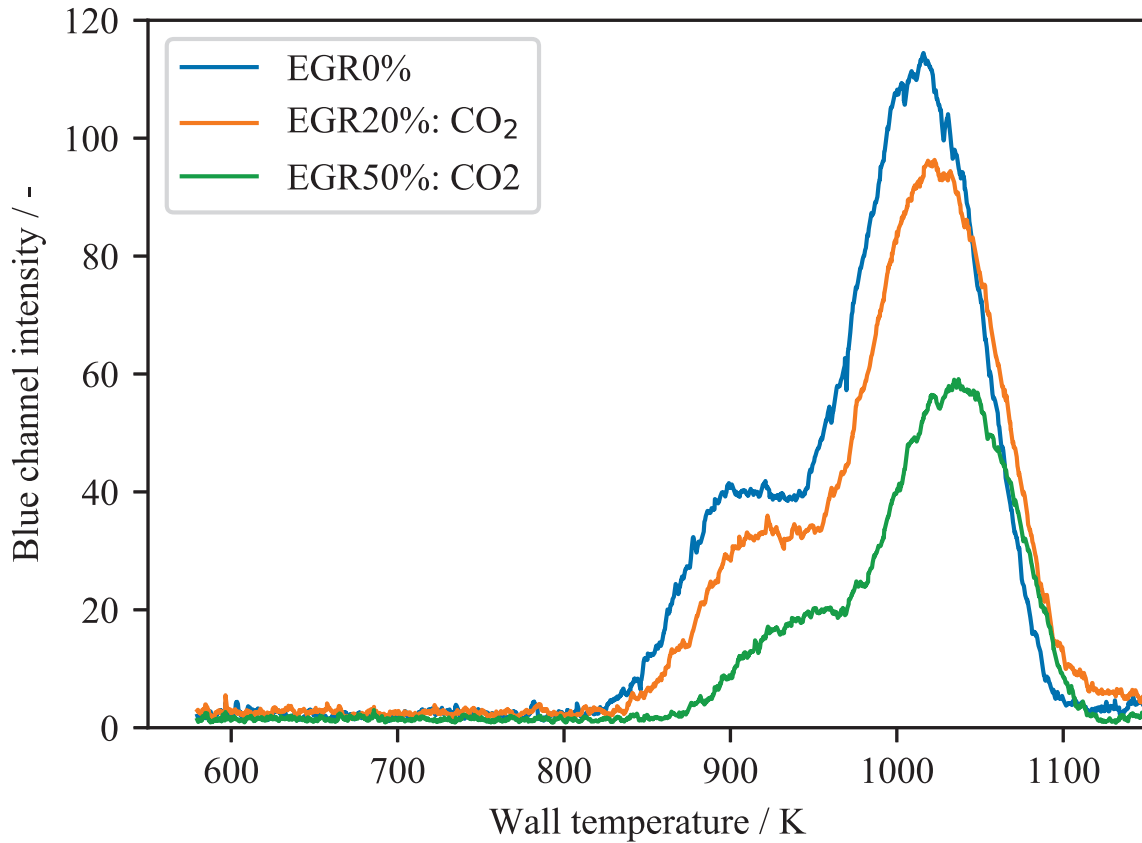


Figure 4.3.2: Luminosity profiles (intensity of blue color channel of RGB image) of *iso*-octane at  $P = 200$  kPa and  $\Phi = 1.0$  for  $\text{CO}_2$  dilution ratios of 0%, 20% and 50%.

while it moved to regions of lower wall temperature. The hot flame also decreased in luminosity, while it broadened and moved to lower wall temperatures. The luminosity profiles of Fig. 4.3.3 along the central axis are shown in Fig. 4.3.4. For an increase of the pressure from 100 kPa to 500 kPa, the peak value of the hot flame decreased by almost 90 %, while it moved to lower wall temperatures by 62 K. As the pressure was increased from 100 kPa to 200 kPa, the blue flame peak luminosity only changed slightly, while its location moved to lower wall temperatures by 60 K. For a further pressure increase to 500 kPa, its peak value decreased by about 75 %, while the location moved 60 K more to lower wall temperatures.



Figure 4.3.3: Weak flame images of *iso*-octane for a dilution ratio of 20% CO<sub>2</sub> at  $\Phi = 1.0$  and pressures between 100 kPa and 500 kPa.

### 4.3.2 Computational results

The computational HRR profiles by the modified KUCRS mechanism for *iso*-octane at a pressure of 200 kPa with dilution by CO<sub>2</sub> of 0 %, 20 % and 50 %, i. e., the conditions of Fig. 4.3.2, are shown in Fig. 4.3.5. For all three dilution rates, three peaks that represent the cool flame, blue flame and hot flame are visible. In all cases, only a small fraction of the heat is released in the cool flame, while the majority of the heat is released throughout the blue flame. Here, the peak HRR decreased by a little more than 50 % as the dilution ratio was increased from 0 % to 50 %. At the same time, the peak location moved to higher wall temperatures by 14 K. The peak value of the hot flame decreased by about 40 % for an increase of the dilution ratio to 50 % and moved to higher wall temperatures by 19 K.

The effect of pressure on the HRR profiles of *iso*-octane with 20 % dilution by CO<sub>2</sub> by the modified KUCRS mechanism is shown in Fig. 4.3.6. For a pressure increase from 100 kPa to 500 kPa, the HRR of the cool flame increased and its peak shifted to lower wall temperatures. Its share of the total HRR, however, stayed small. For the blue flame, the peak HRR increased by about 50 %, while the peak location moved to lower wall temperatures by 141 K. The blue flame behavior with regard to the flame location shows a

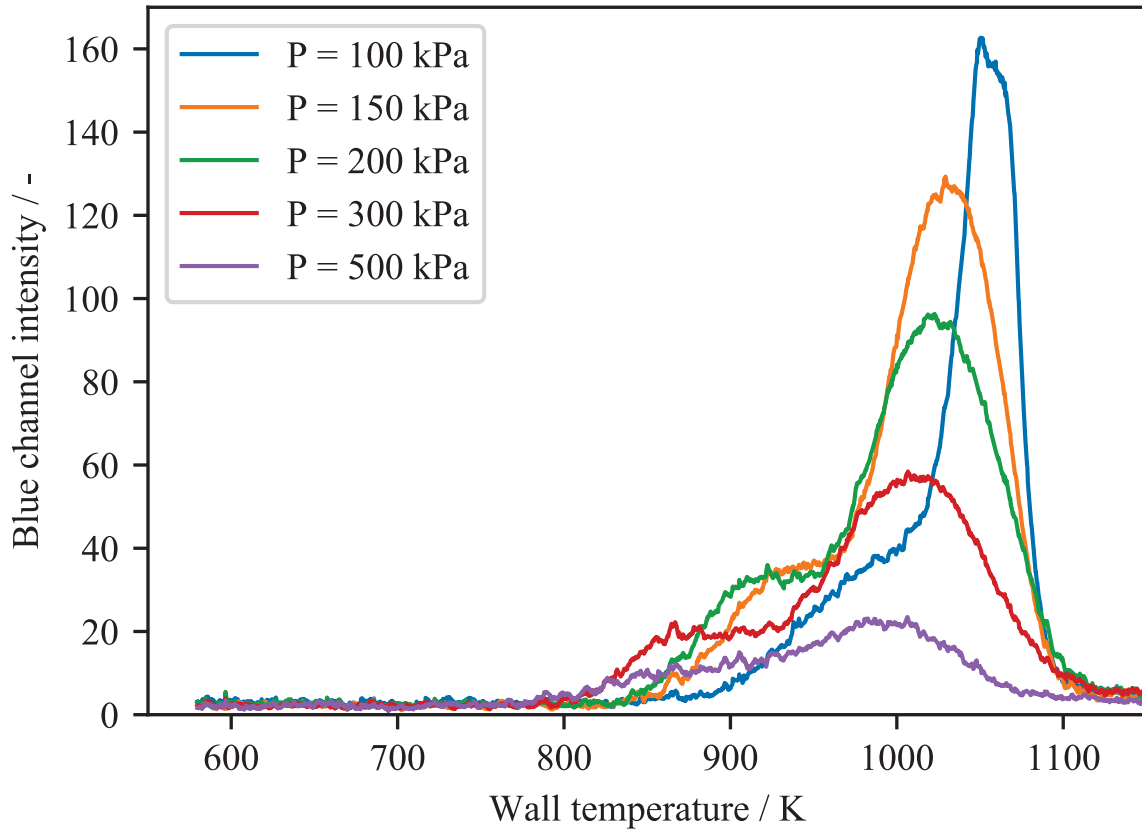


Figure 4.3.4: Luminosity profiles (intensity of blue color channel of RGB image) of *iso*-octane for a dilution ratio of 20% CO<sub>2</sub> at  $\Phi = 1.0$  and pressures between 100 kPa and 500 kPa.

good agreement with the experiment for increasing pressure with a difference of less than 35 K. For the hot flame, the peak HRR showed a strong reduction by more than 90 % as the pressure was increased to 500 kPa. The peak locations, however, moved irregularly for increasing pressure. The first increase of the pressure from 100 kPa to 150 kPa moved the peak location to lower wall temperatures by 12 K. The next pressure increase to 200 kPa shifted the peak to higher wall temperatures by 8 K before moving to lower wall temperatures again by 57 K for an increase of the pressure to 500 kPa. In the experiments, the hot flame moved steadily to lower wall temperatures as the pressure was increased

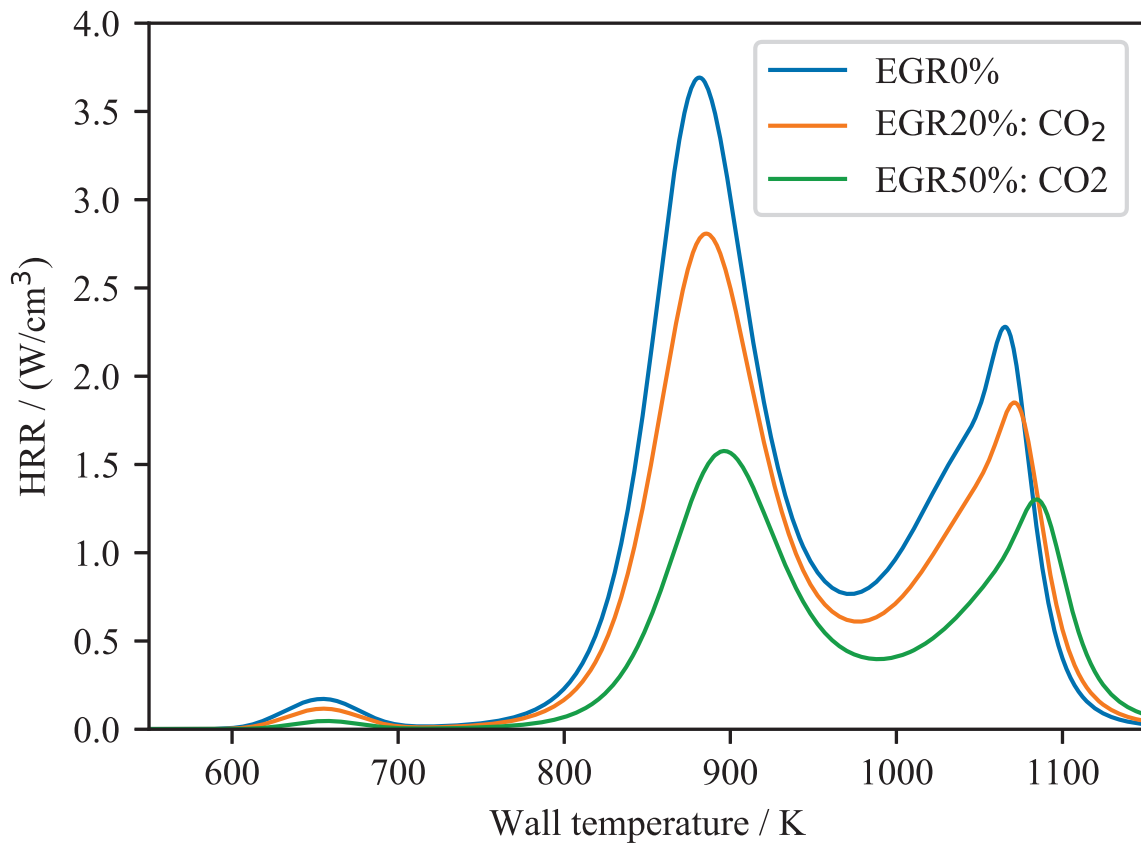


Figure 4.3.5: Heat release rate profiles of *iso*-octane at  $P = 200$  kPa and  $\Phi = 1.0$  for  $\text{CO}_2$ -dilution ratios of 0%, 20% and 50%, as obtained by the modified KUCRS mechanism.

and did not show any irregularities. Based on this behavior, it was concluded that the current definition of the flame location based on HRR is not sufficient. Therefore, a new method for the determination of the flame location in the computations was developed. This will be discussed in the next section.

### 4.3.3 Determination of flame location

One of the main sources of the experimental chemiluminescence comes from excited  $\text{CH}^*$ -radicals. These release light at two peak wavelengths of 390 nm and 431 nm. Here, the dominant peak is usually the second one [129]. In the experiment, images of the weak

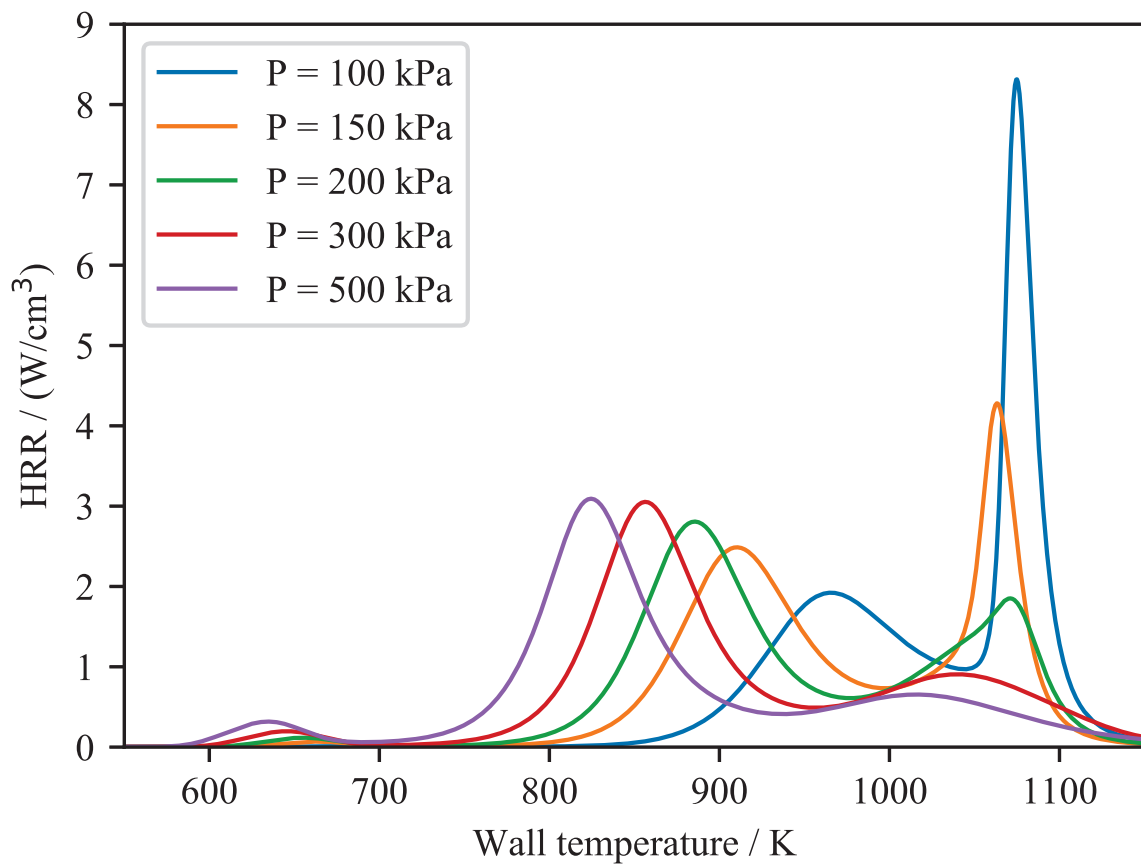


Figure 4.3.6: Luminosity profiles of *iso*-octane for a dilution ratio of 20% CO<sub>2</sub> at  $\Phi = 1.0$  and pressures between 100 kPa and 500 kPa, as obtained by the modified KUCRS mechanism.

flames were taken through a band-pass filter with a transparent wavelength of 431 nm. Previous studies at 100 kPa, with  $\Phi = 1.0$  and without dilution show a good agreement between the computed peak position of non-excited CH radicals and the HRR peaks [77]. One drawback of this comparison, however, was that non-excited CH radicals were used, while the actual photon emission is caused by quenching of excited CH\* radicals. The formation and quenching of excited CH\* radicals is not included in the current KUCRS mechanism. A mechanism for these reactions is, however, provided in [124, 130] and is based on [125, 126]. For the Arrhenius parameters of these reactions see Table 4.2.1.

#### 4 The chemical and dilution effects of EGR on the reactivity of PRF

Another source of chemiluminescence in the range of 431 nm is excited  $\text{CO}_2^*$ . As the quenching of  $\text{CO}_2^*$  emits a broad-band spectrum, only a fraction of its total chemiluminescence is captured by taking images through the band-pass filter. Reactions including  $\text{CO}_2^*$  are also included in [124, 130]. The formation, the quenching and the following photon emission from the excited  $\text{CH}^*$  (see Eq. (4.3)) and  $\text{CO}_2^*$  (see Eq. (4.5)) were calculated in a post processing step. This was possible as the concentration of excited species was assumed to be orders of magnitude smaller than that of the non-excited species [125]. In order to make the experimental chemiluminescence and the calculated photon emissions from  $\text{CH}^*$  and  $\text{CO}_2^*$  comparable, their values were normalized by their respective peak values. A comparison between these normalized values for *iso*-octane at a pressure of 200 kPa with a dilution rate of 20 % by  $\text{CO}_2$  is shown in Fig. 4.3.7. As  $\text{CO}_2^*$  emits a broad-band emission that is filtered through the band-pass filter, only a fraction is registered in the weak flame images. Therefore, a calibration factor was introduced that is multiplied by the  $\text{CO}_2^*$  emission and added to the photon emission of  $\text{CH}^*$  (see Eq. (4.6)). The best calibration results were achieved for a factor of  $5 \times 10^{-5}$ .

$$i_{\text{total}} = i_{\text{CH}^*} + 5 \times 10^{-5} i_{\text{CO}_2^*} \quad (4.6)$$

The total photon emission as calculated by the equation is given in Fig. 4.3.7. It can be seen that by using the HRR definition of the flame location, the blue flame is predicted at lower wall temperatures than the peak of the luminosity in the experiment, while the hot flame is predicted at higher wall temperatures than in the experiment. Additionally, it predicts the intensity of hot flame to be lower than that of the blue flame, which is the opposite trend of the experiment. On the other hand, by using the photon emission from the quenching of the excited  $\text{CH}^*$  radical, very good agreement with regard to the flame

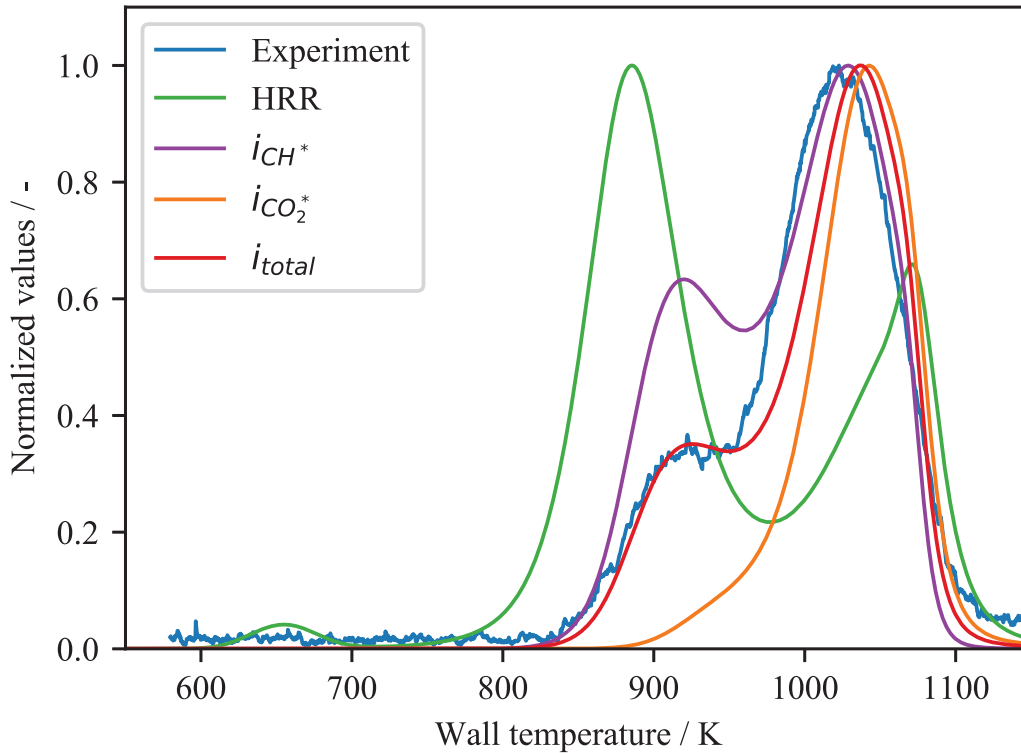


Figure 4.3.7: Comparison of experimental luminosity profile of *iso*-octane for a dilution ratio of 20% CO<sub>2</sub> at  $\Phi = 1.0$  and  $P = 200$  kPa with computational results by modified KUCRS for heat release rate, CH\* chemiluminescence, CO<sub>2</sub>\* chemiluminescence and a combination of CH\* and CO<sub>2</sub>\* chemiluminescence. Note that the values were normalized for easier comparison.

locations of the blue flame and the hot flame was achieved. However, the ratio of the peak value of the blue flame to that of the hot flame was still too large. By looking at the photon emission profile of CO<sub>2</sub>\*, it can be seen that it does not have a peak for the blue flame and that the peak for the hot flame is very close to that of CH\*. By combining the photon emission by CH\* and CO<sub>2</sub>\* through the calibration factor, the best agreement for both the flame locations as well as the peak values was obtained. For the other cases, i. e., for *n*-heptane, different diluents and dilution ratios and different pressures, similar

agreement was found between the experiment and the newly calculated photon emissions. Therefore, the newly developed method for the determination of the flame location will be used in the following section.

#### 4.3.4 Effect of pressure and EGR-like dilution on stoichiometric flame locations

Figure 4.3.8 shows the comparison between the experiment and the simulation of the blue flame and hot flame locations of *iso*-octane at pressures between 100 kPa and 500 kPa, with dilution ratios of 0 %, 20 % and 50 % by N<sub>2</sub>, CO<sub>2</sub> and H<sub>2</sub>O. As the pressure was increased from 100 kPa to 500 kPa in the experiment, the blue flame of the case without dilution (base case, solid black line) moved by 145 K from a wall temperature of 995 K to 850 K. As the dilution ratio was increased to 20 % by N<sub>2</sub> and CO<sub>2</sub>, the blue flame moved to locations that are within the measurement uncertainty of the base case of  $\pm 20$  K. For the dilution by 20 % H<sub>2</sub>O, however, a different trend was seen. For pressures up to 150 kPa, the flame location was within the measurement uncertainty of the base case and those of the other two diluents. As the pressure reached 200 kPa, however, it started to separate from the other flame locations and moved to lower wall temperatures. The separation became even stronger for a pressure of 300 kPa. Here, the blue flame location of the H<sub>2</sub>O case was at a wall temperature that was 35 K lower than that of non-diluted case. An increase of the dilution ratio to 50 % for N<sub>2</sub> and CO<sub>2</sub> moved the blue flame in the other direction, i. e., by 35 K to higher wall temperatures than that of the base-case.

For the hot flame, the change of pressure and dilution had smaller effects than for the blue flame. In case of no dilution (base-case), the pressure increase to 500 kPa moved



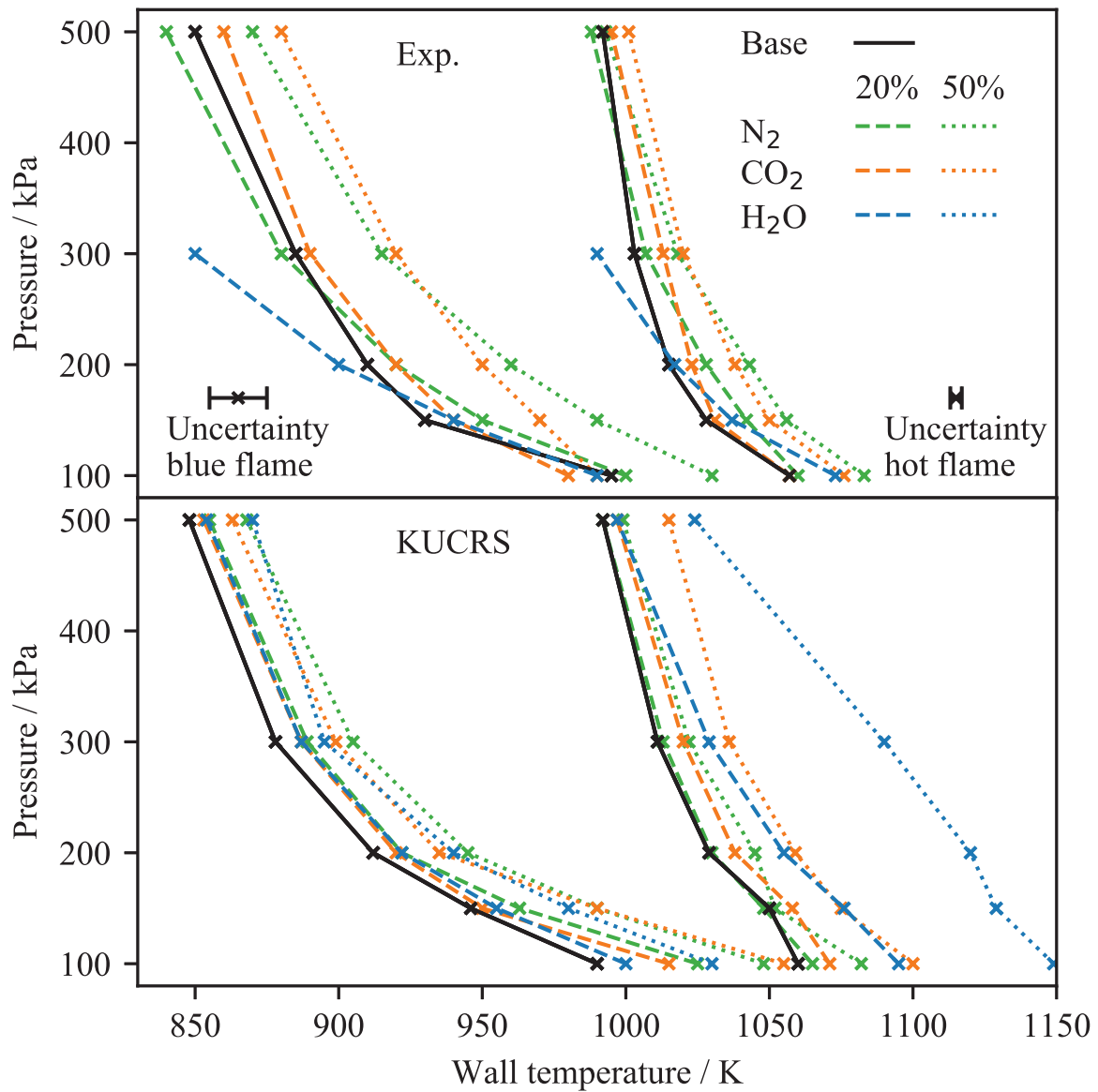


Figure 4.3.8: Wall temperature at the blue flame (left side) and hot flame positions (right side) of *iso*-octane at  $\Phi = 1.0$  and pressures between 100 kPa and 500 kPa as obtained by the experiment and computations by the modified KUCRS mechanism, based on  $i_{\text{total}}$ . Diluents and dilution ratio are indicated by color and line style, black line represents the base case without dilution.

#### 4 The chemical and dilution effects of EGR on the reactivity of PRF

the hot flame by 65 K to lower wall temperatures, which is less than half of the shift of the blue flame. For the cases of 20 % dilution by  $\text{N}_2$  and  $\text{CO}_2$ , the hot flame locations shifted to higher wall temperatures by up to 13 K. Towards the maximum pressure of 500 kPa, the locations of the hot flames converged towards the base case and were within its measurement uncertainty. When  $\text{H}_2\text{O}$  was used as a diluent, the trend was different from the other two diluents but similar to the trend of the blue flame. Up to 200 kPa, the hot flame of the  $\text{H}_2\text{O}$  dilution case was close to or at slightly higher wall temperatures than the base case. For a further increase of the pressure to 300 kPa, however, it was at 13 K lower wall temperature than the base case. As the dilution ratio for  $\text{N}_2$  and  $\text{CO}_2$  was further increased to 50 %, the hot flames moved to higher wall temperatures between 9 K for  $\text{CO}_2$  at 500 kPa and 26 K for  $\text{N}_2$  at 100 kPa. For increasing pressure, the hot flames converged again towards the flame location of the base case.

The lower part of Fig. 4.3.8 shows the flame locations as obtained by the modified KUCRS mechanism, based on the calculated total photon emission. In general, with the exception of the  $\text{H}_2\text{O}$  cases, the trends are similar to those of the experiment. Without dilution (base case), the agreement of the position of the blue flames with the experiment is within 5 K. They moved to lower wall temperatures by 142 K for increasing pressure to 500 kPa. The effect on the blue flame of dilution by 20 % of  $\text{N}_2$  and  $\text{CO}_2$  was small and only moved the flame locations by less than 10 K to higher wall temperatures with the exception of 100 kPa, where the flame was moved by 35 K for dilution by  $\text{N}_2$ . The effect of dilution by  $\text{H}_2\text{O}$  was similar to the other two diluents, which, however, is different from the experiment. As the dilution ratio was increased to 50 %, the blue flames moved further to higher wall temperatures. The largest shift again occurred at 100 kPa and was 65 K for dilution by  $\text{CO}_2$ . On the other hand, dilution by  $\text{H}_2\text{O}$  showed the smallest shift

of only 40 K. For increasing pressure, the flame locations of all diluents converged and were within 10 K.

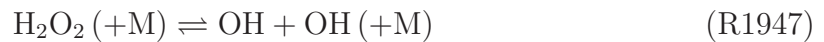
For the hot flame, the effect of the diluents was similar to that of the blue flame with the exception of H<sub>2</sub>O. For an increase of pressure, the hot flame of the base case shifted to lower wall temperatures by 68 K, which agreed well with the experimental results. For a dilution of 20 % by N<sub>2</sub> and CO<sub>2</sub>, the hot flames were located closely to the base case within 11 K. Dilution by H<sub>2</sub>O had a larger effect and shifted the hot flame by 35 K to higher wall temperatures at 100 kPa. For an increase of the pressure to 500 kPa, all hot flame locations converged towards the base case. When the dilution ratio was increased to 50 %, the hot flames shifted further to higher wall temperatures. For dilution by N<sub>2</sub>, the hot flame moved by 22 K at a pressure of 100 kPa, while for CO<sub>2</sub> it moved by 40 K and by 89 K for H<sub>2</sub>O. For increasing pressure, the flame locations of all diluents converged again towards the base case. Overall, a good agreement was found between the results by the modified KUCRS mechanism and the experiment. The exception, however, is the case of dilution by 20 % H<sub>2</sub>O, where in the experiment the blue flame and the hot flame moved to lower wall temperatures but in the simulation they moved in the opposite direction.

#### 4.3.5 Effect of EGR diluents on *iso*-octane weak flames

In order to investigate the role of each diluent on the reactivity of the weak flames, a reaction path analysis was performed for the computational results. The best agreement between the experiment and the simulation was found for the hot flame. Therefore, important reactions of the hot flame will be investigated first. The previous chapters showed that the hot flame reactivity is strongly controlled by H-O reactions [76, 122]. Important reactions that will be investigated in this section are R1932, R1938, R1940,

#### 4 The chemical and dilution effects of EGR on the reactivity of PRF

R1945/1946 and R1947.



All these reactions are part of a system that converts H radicals to OH radicals. The OH radicals, in turn, are important for the oxidation of CO through R1959, which produces another H radical that can restart the cycle. The reaction path analysis for *iso*-octane was conducted at 500 kPa as this is in the range of the pressure at ignition in a gasoline engine. The analysis was conducted at a wall temperature of 970 K, which is at the beginning of the hot flame in all cases. A graphic representation of the reaction path analysis is given in Fig. 4.3.9. In order to make comparison between the different cases easier, all rate of progress variables were normalized by that of the important chain branching reaction R1932. The value of the rate of progress variable of R1932 was largest for the no-dilution case. For the dilution by 20% and 50% N<sub>2</sub>, the rate of progress variable reduced by only 5% and 23%, respectively. This shows that the reduction does not linearly correlate with the dilution ratio. When CO<sub>2</sub> was used as the diluent, the reduction was by 24% and 60%, which is higher than the dilution rate would suggest. For the usage of H<sub>2</sub>O, the rate of progress variable decreases by 54% and 85%, respectively.

A reaction that is in direct competition with the chain branching reaction R1932 is the three-body chain termination reaction R1938. In all dilution cases, the rate of progress

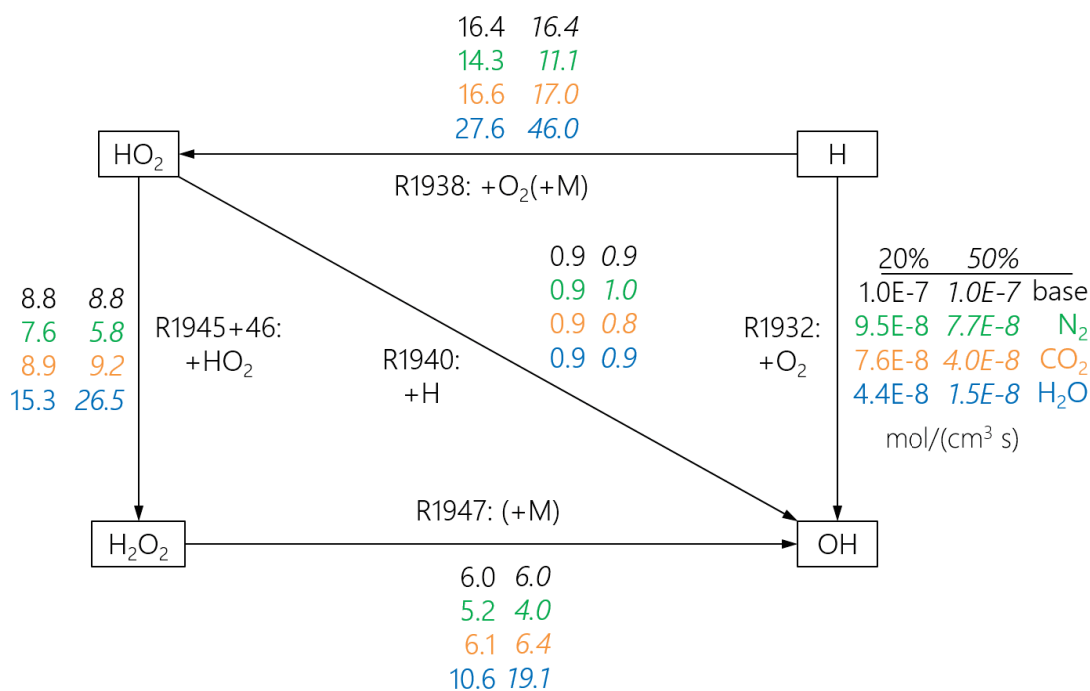


Figure 4.3.9: Main reaction pathways of hydrogen-oxygen reactions at  $T_w = 970$  K for *iso*-octane at 500 Pa as obtained by the modified KUCRS mechanism. Dilution ratios of 0% (indicated as base), 20% and 50% of  $\text{N}_2$ ,  $\text{CO}_2$  and  $\text{H}_2\text{O}$ . Rate of progress of reaction R1932 (right side) shown as absolute values for each dilution case. Rate of progress of remaining reactions shown as normalized values by the corresponding rate of progress of R1932 for each dilution case.

variable of R1938 is significantly larger than that of R1932. A strong factor in this higher rate of progress variable is the elevated pressure of 500 kPa that enhances this three-body reaction. In the no-dilution case, the rate of progress variable of R1938 is approximately 16 times larger than that of R1932. When  $\text{N}_2$  is added as a diluent, this factor decreases by 13% for a dilution ratio of 20% and by 32% for a dilution ratio of 50%. When  $\text{N}_2$  is added as a diluent, it decreases the concentration of chemical species with high enhanced third body efficiencies. Among these are  $\text{CO}_2$  with an enhanced third body efficiency that 3.6 times larger than that of  $\text{N}_2$  and  $\text{H}_2\text{O}$  with an enhanced third body efficiency that

#### 4 The chemical and dilution effects of EGR on the reactivity of PRF

is 16.5 times larger than that of  $N_2$ . This decrease of enhanced third body efficiency by increasing  $N_2$  concentration weakens R1938. When  $CO_2$  is used as a diluent, the effect on R1938 is small. Compared to  $N_2$ , it has a higher enhanced third body efficiency and would enhance this reaction. At the same time, however, it reduces the concentration of  $H_2O$  with its higher enhanced third body efficiency. Therefore, these two effects cancel each other out and only change R1938 little. In the case of  $H_2O$  addition, its high enhanced third body efficiency is dominant and increases R1938 compared to R1932 by 68 % in the case of 20 % dilution and by 180 % in the case of 50 % dilution.

R1938 produces  $HO_2$ , which can react in R1940 with an H radical to form two OH radicals. In this reaction, there is only little difference between the diluents and the rate of progress variable is only slightly smaller than that of R1932. Most of the  $HO_2$ , however, is converted by R1945 and R1946 to form  $H_2O_2$ . The rate of progress variable is approximately half of that of R1938, which is based on the fact that these reactions consume two  $HO_2$  radicals, while R1938 produces only one. Here, again,  $N_2$  shows a decreasing effect on the reaction rate, while  $CO_2$  shows only little change and  $H_2O$  increases the reaction rate, which is based on the effect of these species on R1938. This trend further propagates to R1947, which produces two OH radicals from the dissociation of  $H_2O_2$ . Overall, the three diluents have different effects on the consumption of H and the formation of OH radicals. When  $N_2$  is used as a diluent, it decreases conversion of H by R1938 and shifts it more towards the direct OH production by R1932. In the case of  $CO_2$ , its enhanced third body efficiency is higher than that of  $N_2$  but not as high as that of  $H_2O$ . This leads to  $CO_2$  not having a big effect on the ratio of H conversion between R1932 and R1938. As  $H_2O$  is added as a diluent, its large enhanced third body efficiency strengthens R1938. As the conversion of H to OH progresses through the intermediate formation of

$\text{HO}_2$  and  $\text{H}_2\text{O}_2$ , it decreases the overall reactivity. This decrease is responsible for the shift of the hot flame to higher wall temperatures for the addition of  $\text{H}_2\text{O}$ . This shift was seen in Fig. 4.3.8, where the hot flames of dilution by  $\text{H}_2\text{O}$  were located at the highest wall temperatures.

The results of the effect of the different diluents on the hot flame show good agreement with those of a previous study on syngas [76]. Here,  $\text{H}_2\text{O}$  showed the strongest retarding effect in the experiment and simulation. In the current study, however,  $\text{H}_2\text{O}$  only had a retarding effect in the simulation, while it shifted the hot flame to lower wall temperatures in the experiment. This hints at  $\text{H}_2\text{O}$  having an effect on the reactivity that is not included in the simulation. While syngas only shows a single hot flame, *iso*-octane has an additional blue flame that is also influenced by the added third bodies. An important reaction in the blue flame is the chain branching reaction R1947 [131, 132]. This reaction also has enhanced third body efficiencies and is therefore expected to be sensitive to the diluents. The values of the enhanced third body efficiencies of R1947 are similar to those of R1938. The difference between these reactions, however, is that R1947 is a chain branching reaction while R1938 is a chain termination reaction. When the mixture was diluted by  $\text{N}_2$  and  $\text{CO}_2$ , the chain branching of R1947 was decreased, which led to the blue flame being located at higher wall temperatures in both the experiment and the simulation.  $\text{H}_2\text{O}$ , however, has the highest enhanced third body efficiency, which is expected to increase chain branching and reactivity. This is observed in the experiment, where the blue flame shifted to lower wall temperatures as  $\text{H}_2\text{O}$  was added. This effect, however, was not observed in the simulation. This missing promoting effect of  $\text{H}_2\text{O}$  on the blue flame is assumed to further influence the hot flame in the same manner. These observed differences between the simulation and the experiment show that further investigations of three-body

reactions and the enhanced third body efficiencies of diluents are necessary.

### 4.3.6 Effect of EGR diluents on *n*-heptane weak flames

For *n*-heptane, the locations of its separated weak flames as obtained by the experiment and the modified KUCRS mechanism are shown in Fig. 4.3.10. The trends for the experimental flame locations of the blue flame and the hot flame are similar to those of *iso*-octane. In the experiment, the trends of the blue flame and the hot flame were similar to those of *iso*-octane. For pressures above 100 kPa, an additional cool flame appeared, which was not observed for *iso*-octane. For the hot flame of the case without dilution (base case), as the pressure was increased from 100 kPa to 500 kPa, its location shifted to lower wall temperatures by 40 K. Compared to *iso*-octane, it was at up to 29 K lower wall temperatures. As diluents were added with a dilution ratio of 20 %, it had only little effect on the location of the hot flame, which was within 10 K of the base case. Furthermore, differences between the three diluents were small. As the dilution ratio by CO<sub>2</sub> was increased to 50 %, the hot flame moved to higher wall temperatures. For the addition of 50 % N<sub>2</sub>, a slightly different trend was observed. As the pressure was increased to 150 kPa, the hot flame shifted slightly to higher wall temperatures. For a further increase of the pressure, however, it shifted to lower wall temperatures and moved towards the base case. This behavior was not observed for *iso*-octane.

The flame location of the experimental blue flame (base case) moved to lower wall temperatures by 60 K as the pressure was increased to 500 kPa. This shift is less than half of that of *iso*-octane. As N<sub>2</sub> and CO<sub>2</sub> were added at dilution ratios of 20 %, the locations of the blue flames were within 10 K of the base case, which is within the measurement uncertainty. For a dilution ratio of 50 %, a stronger effect was observed. In the case of



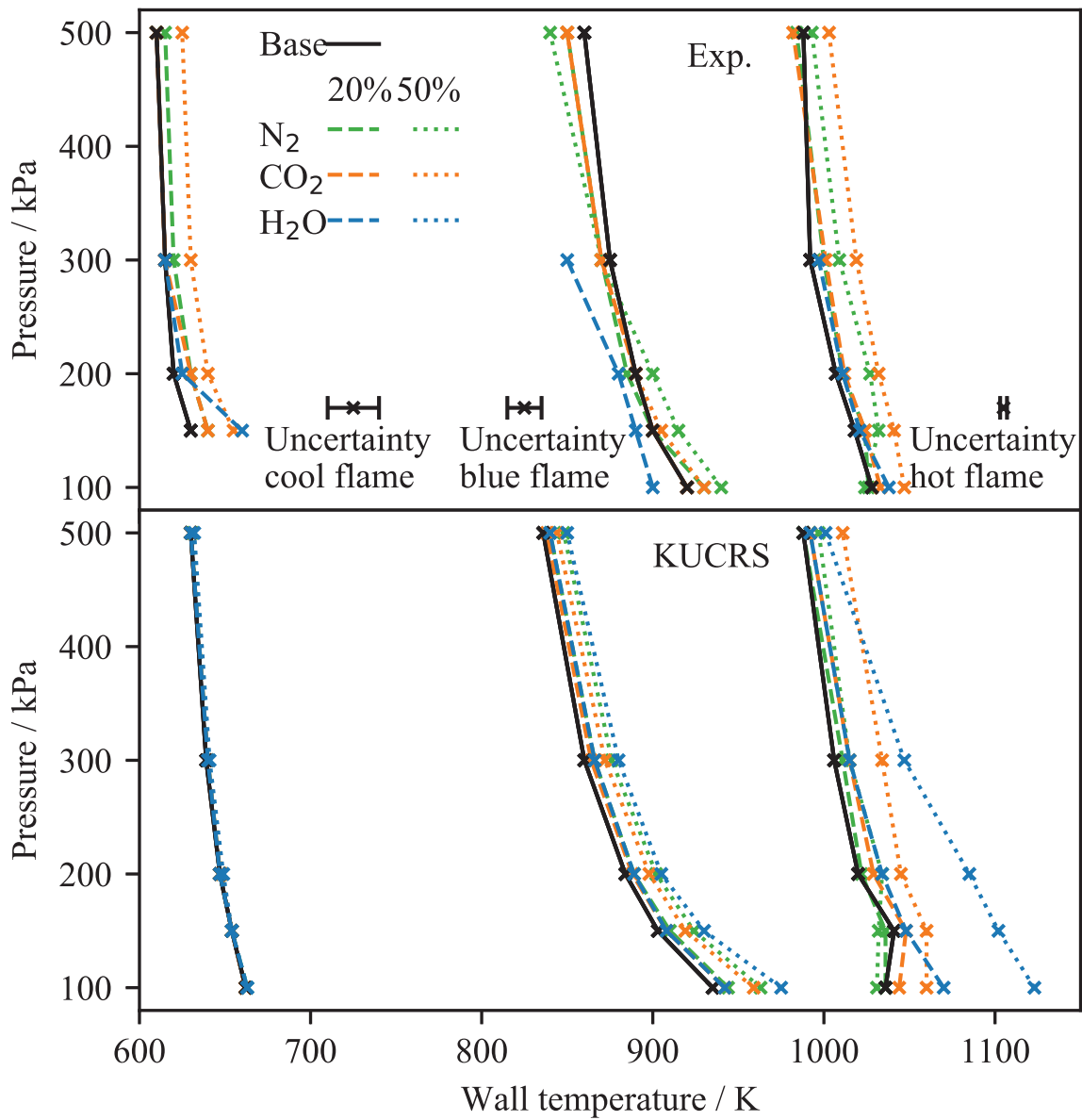


Figure 4.3.10: Wall temperature at the cool flame (left side), blue flame (middle) and hot flame positions (right side) of *n*-heptane at  $\Phi = 1.0$  and pressures between 100 kPa and 500 kPa as obtained by the experiment and computations by the modified KUCRS mechanism, based on  $i_{total}$ . Diluents and dilution ratio are indicated by color and line style, black line represents the base case without dilution.

#### 4 The chemical and dilution effects of EGR on the reactivity of PRF

$\text{N}_2$  addition, the blue flame was located at 20 K higher wall temperature than the base case at 100 kPa and at 20 K lower wall temperature at 500 kPa. For the dilution by  $\text{H}_2\text{O}$  of 20 %, the blue flame moved up to 25 K to lower wall temperatures than the base case, which is similar to the results of *iso*-octane.

The cool flame only appeared for pressures above 100 kPa. It, however, showed only little response to increasing pressure and the addition of diluents. Without dilution (base-case), the location of the cool flame moved to lower wall temperatures by 20 K for increasing pressure, which is half of that of the hot flame and one third of that of the blue flame. For dilution by 20 %  $\text{N}_2$  and  $\text{CO}_2$ , the flame moved to higher wall temperatures by less than 10 K, which is within the measurement uncertainty of 15 K.

As  $\text{H}_2\text{O}$  was used as a diluent, it showed the largest shift at 150 kPa, where the cool flame moved by 20 K to higher wall temperatures. For higher pressures, however, the wall temperatures at the cool flame location were similar to those of  $\text{N}_2$  and  $\text{CO}_2$ . By increasing the dilution rate of  $\text{N}_2$  to 50 %, the cool flame was only visible at 500 kPa. In this case, the wall temperature at the flame location was the same as in the base case. For 50 % of  $\text{CO}_2$ , cool flames were visible for pressures between 150 kPa and 500 kPa and were located at up to 15 K higher wall temperatures than in the base case.

The flame locations of the simulations for *n*-heptane are shown in the lower half of Fig. 4.3.10. For the base case, the trend of the hot flame as the pressure was increased to 500 kPa shows a similar behavior as that of 50 % dilution by  $\text{N}_2$  in the experiment. For an increase of the pressure to 150 kPa, the hot flame shifted slightly to higher wall temperatures. As the pressure was further increased to 500 kPa, it moved to lower wall temperatures again. This trend was also observed for dilution by 20 % of  $\text{N}_2$  and  $\text{CO}_2$  and dilution by 50 % of  $\text{N}_2$ . In the case of  $\text{H}_2\text{O}$ , this trend was not observed. At 100 kPa, the

hot flame was located at 34 K higher wall temperatures than the base case. For increasing pressure, the flame location converged towards the base case and was similar to those of the other two diluents. For  $N_2$ , as the dilution ratio was increased to 50 %, the flame location changed only little, while it showed the same turning for increasing pressure as the dilution by 20 %.  $CO_2$  had a stronger effect as the dilution ratio was increased to 50 %. Here, the location of the hot flame shifted by up to 28 K to higher wall temperatures. Dilution by 50 % of  $H_2O$  showed the largest effect and moved the hot flame to up to 87 K higher wall temperatures (100 kPa). For increasing pressure, the hot flame locations of all cases converged towards the base case. This behavior is similar to that of *iso*-octane.

The base case blue flame of the modified KUCRS mechanism moved to lower wall temperatures by 99 K for an increase of the pressure from 100 kPa to 500 kPa. Here, the flame locations were within 24 K of the experimental results. For the dilution by 20 % of all diluents, the change of the flame location was small, which is in good agreement with the experiment. A further increase of the dilution ratio to 50 % led to a shift of the hot flame to higher wall temperatures by up to 41 K in the case of  $H_2O$  dilution. For  $N_2$  and  $CO_2$ , this shift is slightly less. Overall, these results show good agreement with the experimental results. Only  $H_2O$  shows different trends between the simulation and the experiment, which is similar to the results by *iso*-octane. Compared to *iso*-octane, increasing pressure and dilution had smaller influence on the blue flame locations.

In the base case, the cool flame as obtained by the modified KUCRS mechanism moved to lower wall temperatures by 32 K for an increase of the pressure to 500 kPa. Compared to the experiment, it is located at up to 24 K higher wall temperatures. For dilution by  $N_2$ ,  $CO_2$  and  $H_2O$  at both dilution ratios, the effect was small and the flames moved less than 2 K to higher wall temperatures, which is much smaller than the effect on the hot

#### 4 The chemical and dilution effects of EGR on the reactivity of PRF

flame and the blue flame.

For *iso*-octane, the chemical effect of N<sub>2</sub>, CO<sub>2</sub> and H<sub>2</sub>O on the hot flame and the blue flame was discussed in the previous section and applies to *n*-heptane as well. A big difference between the experimental results of *iso*-octane and those of *n*-heptane, however, was found for the dilution by N<sub>2</sub>. Here, for an increase of the pressure to 150 kPa, the hot flame shifted to higher wall temperatures, which is opposite to the results for *iso*-octane. As the pressure was further increased, the flame moved to lower wall temperatures again. For the higher dilution ratio of 50 % by N<sub>2</sub>, this trend was further intensified. For dilution by CO<sub>2</sub> and H<sub>2</sub>O, however, this trend was not observed. In the simulations, this trend occurred for the base case, for dilution by N<sub>2</sub> and for dilution by CO<sub>2</sub>. For dilution by H<sub>2</sub>O, however, this trend did not occur. As was shown in chapter 2, reactions of the hydrogen-oxygen system strongly control the reactivity of the hot flame. For the H-O system, as the pressure is increased, the explosion limit shows a transition from the second to the third limit (see Fig. 4.3.11). This behavior is similar to that of the hot flames that first moved to higher and then to lower wall temperatures for increasing pressure. In the H-O system, the competition between the chain branching reaction R1932 (corresponds to R1 in Fig. 4.3.11) and the chain termination reaction R1938 (corresponds to R9 in Fig. 4.3.11) controls the second explosion limit. The line of transition from the non-explosive to the explosive regime is given by Eq. (4.7) in KUCRS reaction numbers. Here,  $k$  is each reaction's rate constant and  $[M]$  is the concentration of the mixture (including enhanced third body efficiencies).

$$2k_{1932} = k_{1938}[M] \quad (4.7)$$

As was shown before, R1938 (R9) strongly depends on the composition of the mixture as

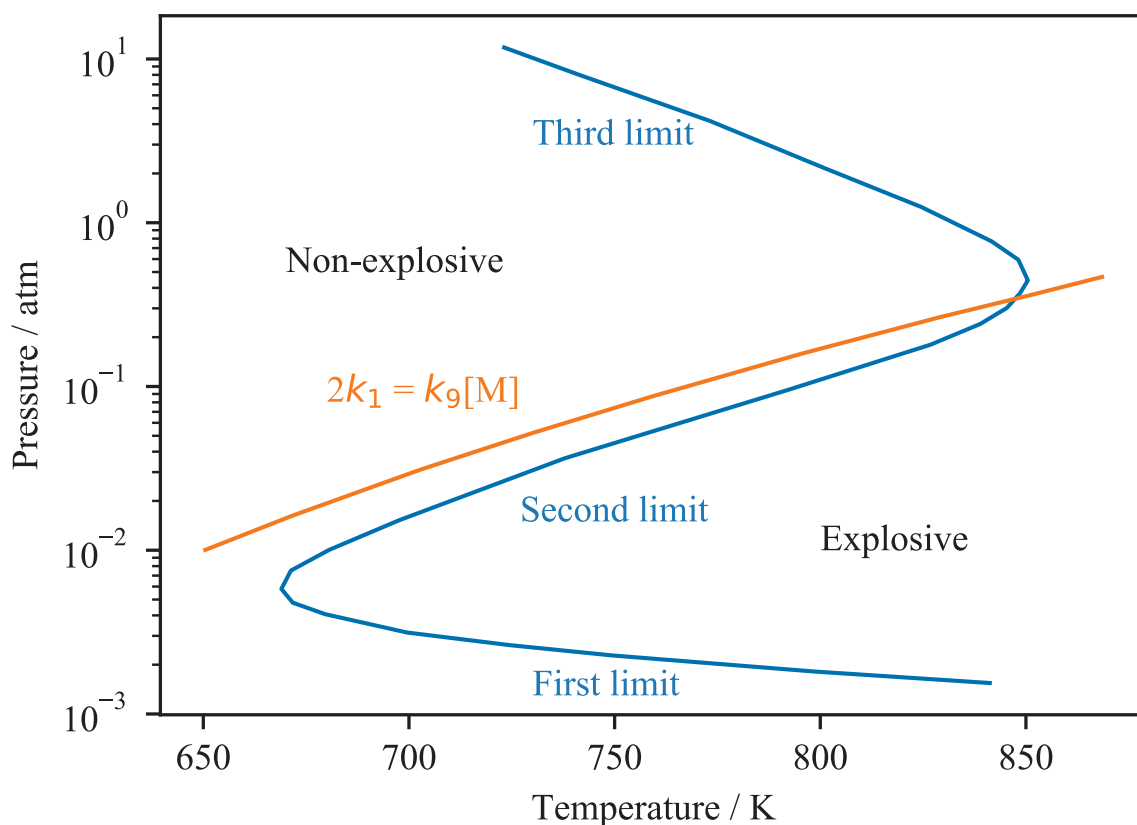


Figure 4.3.11: Explosion limits of stoichiometric  $\text{H}_2\text{-O}_2$  mixture. Data obtained from [15].

it is a three body reaction with enhanced third body efficiencies. Fig. 4.3.12 shows the rate constant of R1932 (multiplied by 2 as in Eq. (4.7)) and the rate constant of R1938 multiplied by  $[\text{M}]$  for different diluents at 100 kPa. The intersection of the curves shows the transition point from the non-explosive to the explosive regime. In the case without dilution, this point is located at 1005 K. For dilution by 50%  $\text{N}_2$ , this point moves to 985 K. On the other hand, when  $\text{H}_2\text{O}$  is used as a diluent, this point moves to 1145 K. These shifts take place at constant pressure and therefore shift the line of transition in Fig. 4.3.11 to the right (higher temperatures) for addition of  $\text{H}_2\text{O}$  or to the left (lower temperatures) for the addition of  $\text{N}_2$ . In case of  $\text{N}_2$  addition, this moves the point of transition from the second explosion limit to the third explosion limit to higher pressures.

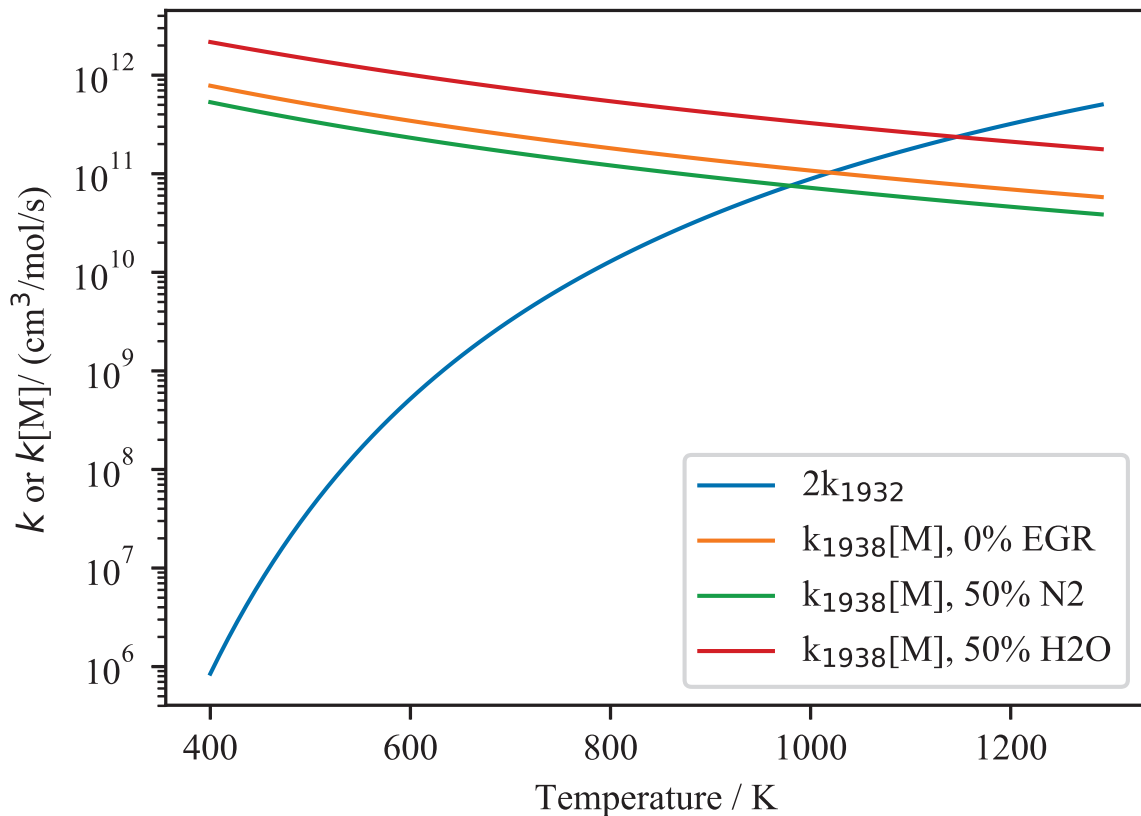


Figure 4.3.12: Comparison of the rate constants of R1932 and R1938 for different dilution conditions at 100 kPa as obtained by the modified KUCRS mechanism.

This shift to higher pressures was shown for the experiment in Fig. 4.3.10, where higher N<sub>2</sub> concentrations shifted the transition point to pressures higher than 100 kPa. The same trend for N<sub>2</sub> addition was found in the computational results by the modified KUCRS mechanism. When H<sub>2</sub>O is added, however, the transition point moves to lower pressures. For the computations, this trend can be seen in Fig. 4.3.10 as this transition is absent. This indicates that the transition point is at a pressure below 100 kPa.

### 4.3.7 Heat contribution index

At low pressures, the locations of the separated weak flames are good indicators for the reactivity [72–74, 122]. At elevated pressures, however, another method exists for the evaluation of reactivity, the Heat Contribution Index (HCI) (see section 3.3.4) [123]. The HCI is determined by the ratio of the heat release in each of the three separated weak flames to the total heat release throughout the MFR (see Eq. (3.1)). Based on this definition, the sum of the Cool flame-HCI, Blue flame-HCI and Hot flame-HCI is unity. Without dilution, the value of the Hot flame-HCI was constant and independent of the base fuel. This was explained by the governing role of the H-O system and the oxidation of CO, which were the same for all cases. On the other hand, the Cool flame-HCI and the Blue flame-HCI showed large differences between the fuels. High-reactivity fuels, such as *n*-heptane, showed high values for the Cool flame-HCI and low values for the Blue flame-HCI. Low-reactivity fuels, e. g., *iso*-octane, on the other hand, showed low values for the Cool flame-HCI and high values for the Blue flame-HCI.

The HCIs of *iso*-octane for the dilution by N<sub>2</sub>, CO<sub>2</sub> and H<sub>2</sub>O at 500 kPa as obtained by the modified KUCRS mechanism are plotted in Fig. 4.3.13. The Cool flame-HCI decreases with increasing dilution ratio from 0.072 (no dilution) to 0.049 (50 % dilution), while it does not show significant differences between the diluents. This shows that the dilution effect is dominant over the chemical effect for the cool flame. Furthermore, as the dilution ratio is increased, the lower Cool flame-HCI indicates lower reactivity at low temperatures of the cool flame. When compared to PRF cases without dilution of the previous chapter, the decreasing Cool flame-HCI can be regarded as an increase of the RON by 12.

Among the three HCIs, the Blue flame-HCI shows the largest values. This agrees with

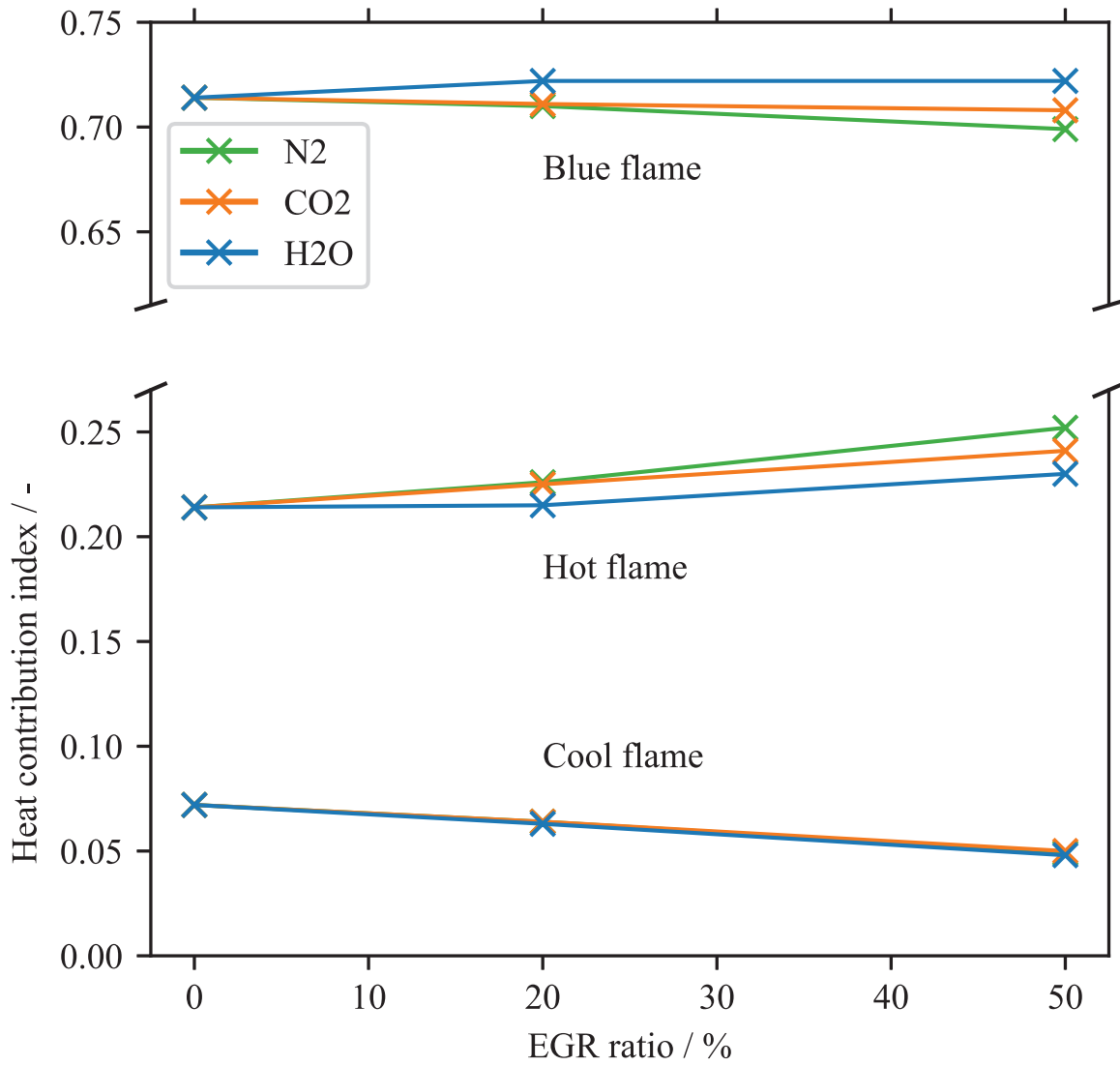


Figure 4.3.13: Heat contribution index of the cool flame, blue flame and hot flame of *iso*-octane at  $\Phi = 1.0$  and  $P = 500$  kPa for different diluents and dilution ratios as obtained by KUCRS.



the results of the previous chapter. For the addition of  $N_2$  and  $CO_2$ , the Blue flame-HCI decreases slightly with increasing dilution ratio, while the differences between these two diluents is small. As the sum of all three HCIs is unity, the Hot flame-HCI increases accordingly. This shift of the heat release from the blue flame to the hot flame shows a reduction of the reactivity when dilution is performed by  $N_2$  and  $CO_2$ . When  $H_2O$  is used as a diluent, the Blue flame-HCI increases slightly with increasing dilution ratio, while the Hot flame-HCI increases less than for  $N_2$  and  $CO_2$ . This shows that  $H_2O$  promotes reactivity at intermediate temperatures, which was already shown by experimental results in the previous section. There, this effect was explained by the enhancing effect of  $H_2O$  on the chain branching reaction R1947. Overall, however, the addition of  $H_2O$  leads to a slight reduction of reactivity compared to the base case, as less heat is released in the cool flame and more heat is left to be released in the hot flame. The differences between  $H_2O$  and the other two diluents agrees well with the experimental results, where the addition of  $H_2O$  moved the blue flame and the hot flame to lower wall temperatures than for  $N_2$  and  $CO_2$ .

The corresponding HCIs of *n*-heptane are shown in Fig. 4.3.14. The values of the Cool flame-HCI are about five times larger than those of *iso*-octane. For increasing dilution ratios, the Cool flame-HCI decreases, which is similar to *iso*-octane. The values for dilution by  $N_2$  and  $CO_2$  are similar and decrease from 0.270 without dilution to 0.233 for 50 % dilution by  $CO_2$ . When this decrease is compared to Cool flame-HCIs of PRF without dilution, it represents an increase of the RON by 24. When  $H_2O$  is used as a diluent, the reduction of the Cool flame-HCI is larger. This can be explained by its influence on the equilibrium of the important low-temperature reaction  $nC_7H_{16} + OH \rightleftharpoons nC_7H_{15} + H_2O$  as the concentration of  $H_2O$  is increased. For dilution by  $H_2O$ , the Cool flame-HCI decreases

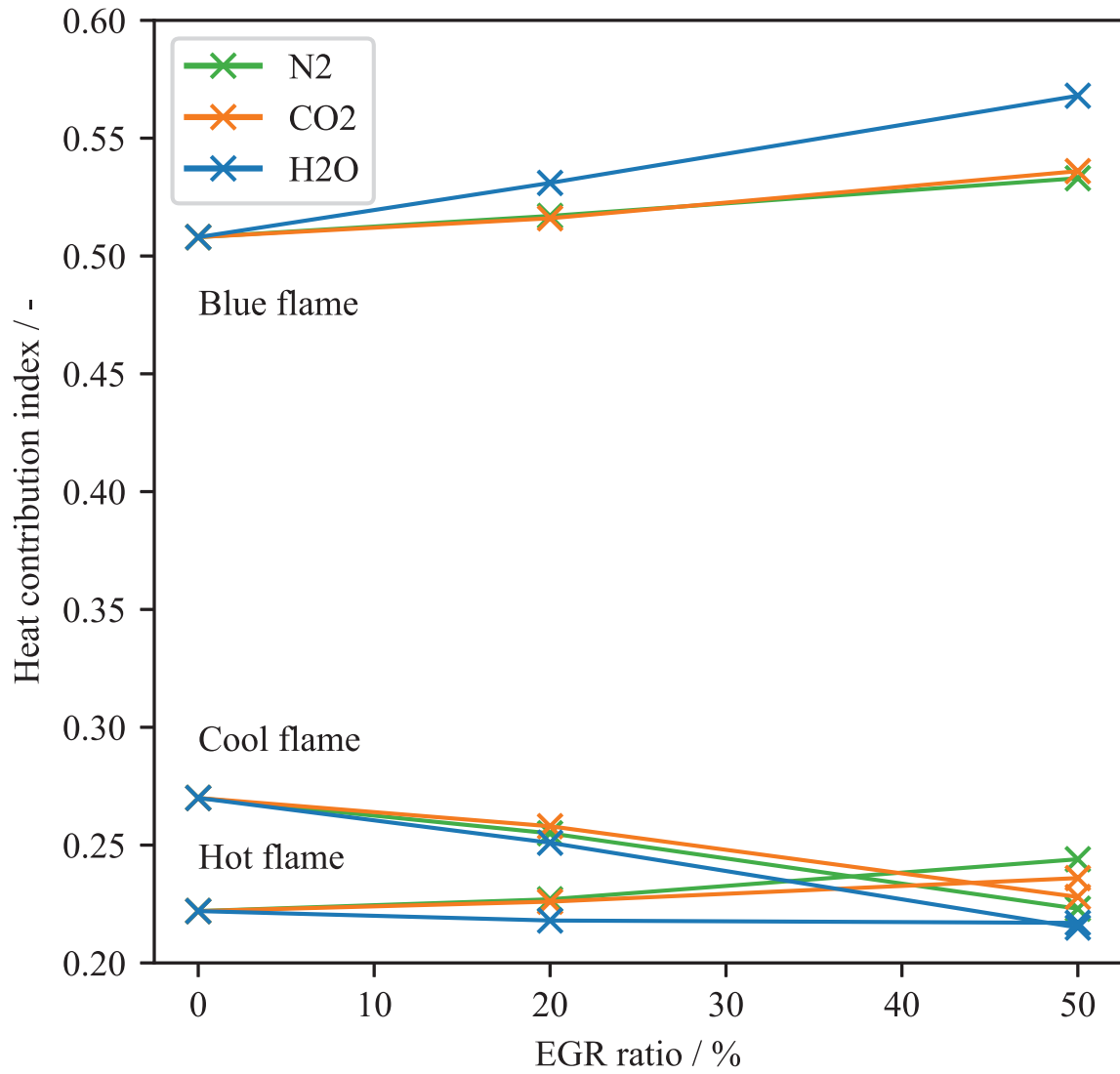


Figure 4.3.14: Heat contribution index of the cool flame, blue flame and hot flame of *n*-heptane at  $\Phi = 1.0$  and  $P = 500$  kPa for different diluents and dilution ratios as obtained by KUCRS.

from 0.270 without dilution to 0.215 with 50 % dilution. This change represents an increase of the RON by 28. The results for all diluents indicate lower reactivity of the cool flame as dilution ratios are increased. The relatively large reduction of the Cool flame-HCI shows good agreement with previous studies [28], which found a stronger dilution effect for fuels with multi-stage ignition, such as *n*-heptane.

For the blue flame, the HCI increases for the addition of all three diluents, which is different from the results of *iso*-octane. Similar to *iso*-octane, H<sub>2</sub>O shows the biggest effect on the blue flame, which is inverse to that of the cool flame. Again, this can be explained by the enhancing effect of H<sub>2</sub>O on the three-body chain branching reaction R1947. For N<sub>2</sub> and CO<sub>2</sub>, the increase of the Blue flame-HCI is approximately half of that of H<sub>2</sub>O, which is less than the decrease of the Cool flame-HCI.

For the hot flame, the addition of H<sub>2</sub>O does not show an effect on its HCI as the decrease of the Cool flame-HCI is compensated by the increase of the Blue flame-HCI. On the other hand, the addition of N<sub>2</sub> and CO<sub>2</sub> increases the Hot flame-HCI. Overall, these results show that H<sub>2</sub>O reduces reactivity at low temperatures, increases reactivity at intermediate temperatures and does not influence reactivity at high temperatures. For N<sub>2</sub> and CO<sub>2</sub>, the inhibiting effect at low temperatures is weaker, the promoting effect at intermediate temperatures is weaker too, while the reactivity at high temperatures is increased.

The results of this chapter show that the weak flame locations as well as the HCI can be used to eliminate the thermal effect and to separate the chemical and the dilution effects for different diluents at low, intermediate and high temperatures. *n*-Heptane, a fuels with strong multi-stage ignition, is strongly influenced by EGR-like dilution. Here, H<sub>2</sub>O, a species with a large enhanced third body efficiency, has the largest effect on reactivity. It decreases low temperature reactivity, while it increases reactivity at intermediate and

high temperatures. The same trends were found for investigations of *iso*-octane. For the hot flame, however, H<sub>2</sub>O has an inhibiting effect due to its large enhanced third body efficiency that enhances chain termination.

## 4.4 Conclusions

In this chapter, separated weak flames in a vertical-type micro flow reactor with a controlled temperature profile were used to investigate the chemical and the dilution effects of N<sub>2</sub>, CO<sub>2</sub> and H<sub>2</sub>O on *n*-heptane and *iso*-octane. To further analyze their impact chemical reactions and the heat release rate, one-dimensional steady computations were performed. In the experiments, as the pressure was increased, the cool flames, blue flames and hot flames of both fuels moved to lower wall temperatures. For N<sub>2</sub> and CO<sub>2</sub>, the dilution by 20 % had only little effect on the flame positions. As this dilution ratio was further increased to 50 %, however, the blue flame and the hot flame moved to higher wall temperatures. For both fuels, when H<sub>2</sub>O was added as a diluent, however, the blue flame and the hot flame moved to lower wall temperatures.

In order to make flame locations between the experiment and the simulation more comparable, a new method for the determination of the flame locations based on photon emission by excited CH\* and CO<sub>2</sub>\* was developed. By using this new method, good agreement between the simulation and the experiment was found. Furthermore, reaction path analysis was performed and showed that the enhanced third body efficiency of the dilution species had a strong effect on three body chain branching and chain termination reactions. At intermediate temperatures, the addition of H<sub>2</sub>O promotes reactivity while at high temperatures it has an inhibiting effect. For N<sub>2</sub>, the effect is opposite, while CO<sub>2</sub>

only had a weak influence. For *n*-heptane it was furthermore found that the addition of N<sub>2</sub> shifts the point of transition from the second explosion limit of the hydrogen-oxygen system to the third limit to higher pressures.

As an additional measure, the heat contribution indexes for the addition of diluents were calculated for all three separated weak flames. For both fuels, the heat release of the cool flame was decreased and shifted to the blue and the hot flame as the dilution ratio was increased. For the addition of 50% H<sub>2</sub>O, this shift corresponded to an increase of the RON by 28 for *n*-heptane and to an increase by 12 for *iso*-octane. Overall, these results show that separated weak flames in the MFR offer great potential to investigate the influence of EGR species on fuel reactivity at low, intermediate and high temperatures.



# Appendix

## 4.A Results for LLNL

Figure 4.A.1 shows the comparison of the experimental luminosity profile for *iso*-octane with a dilution by 20% CO<sub>2</sub> at a pressure of 200 kPa as well as the computational heat release rate and calculated photon emission by Eq. (4.6) for the LLNL PRF mechanism. Compared to the results of the modified KUCRS mechanism in Fig. 4.3.7, the heat release rate in the cool flame is much stronger, while the blue flame is weaker. The calculation of the total photon emission by CH\* and CO<sub>2</sub>\* showed a good agreement for the location of the blue flame with the experiment. However, the location of the hot flame was located at a wall temperature that is 75 K higher than in the experiment.

Figure 4.A.2 shows the flame locations of the blue flame and the hot flame of *iso*-octane for the experiment and the simulations by LLNL. The locations of the blue flames by LLNL showed similar results to those of KUCRS (see Fig. 4.3.8). For the base case, the blue flame shifted upstream by 161 K as the pressure was increased to 500 kPa. The agreement with the experiment was within 10 K. Here, again, the 20% dilution conditions shifted the blue flame only slightly to higher wall temperatures. The addition of 50% diluents showed a larger shift, which was up to 45 K for H<sub>2</sub>O at 100 kPa. For an increase of the pressure,

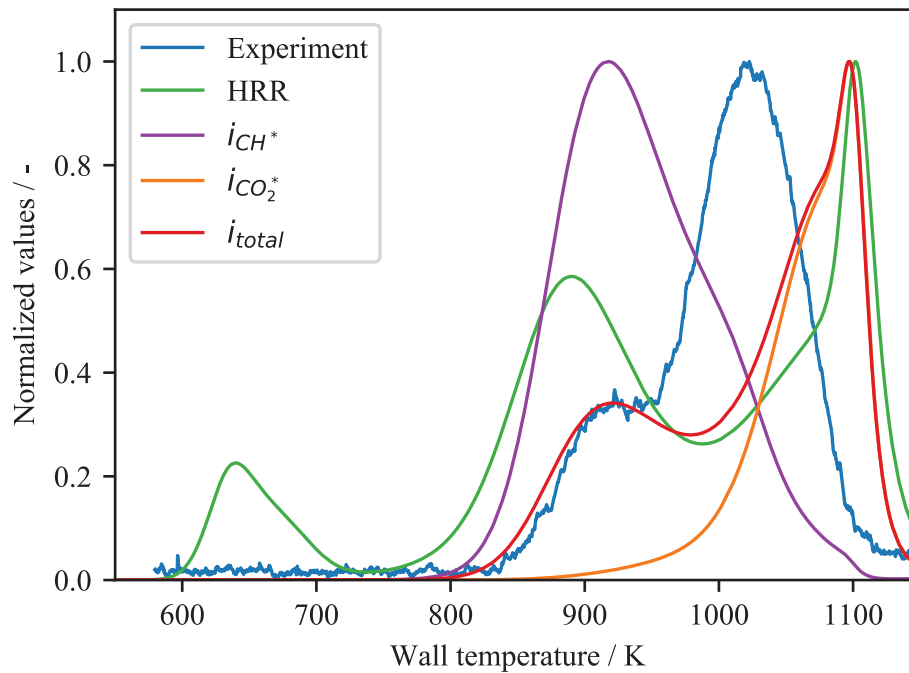


Figure 4.A.1: Comparison of experimental luminosity profile of *iso*-octane for a dilution ratio of 20% CO<sub>2</sub> at 200 kPa with computational results by LLNL for heat release rate, CH\* chemiluminescence, CO<sub>2</sub>\* chemiluminescence and a combination of CH\* and CO<sub>2</sub>\* chemiluminescence. Note that the values were normalized for easier comparison.

the flame locations converged towards the base case. In general, the results for the blue flame agreed well with the experimental results.

The wall temperature at the location of the hot flame, however, showed rather large differences as compared to the experiment and KUCRS. For the base case, as the pressure was increased from 100 kPa to 150 kPa, the flame shifted to lower wall temperatures. As the pressure was further increased to 200 kPa, the flame shifted to higher wall temperatures again. At higher pressures, the flame changed direction another time and moved to lower wall temperatures. The overall change was 38 K for increasing pressure, with flame locations up to 46 K higher than in the experiment. The same behavior occurred when



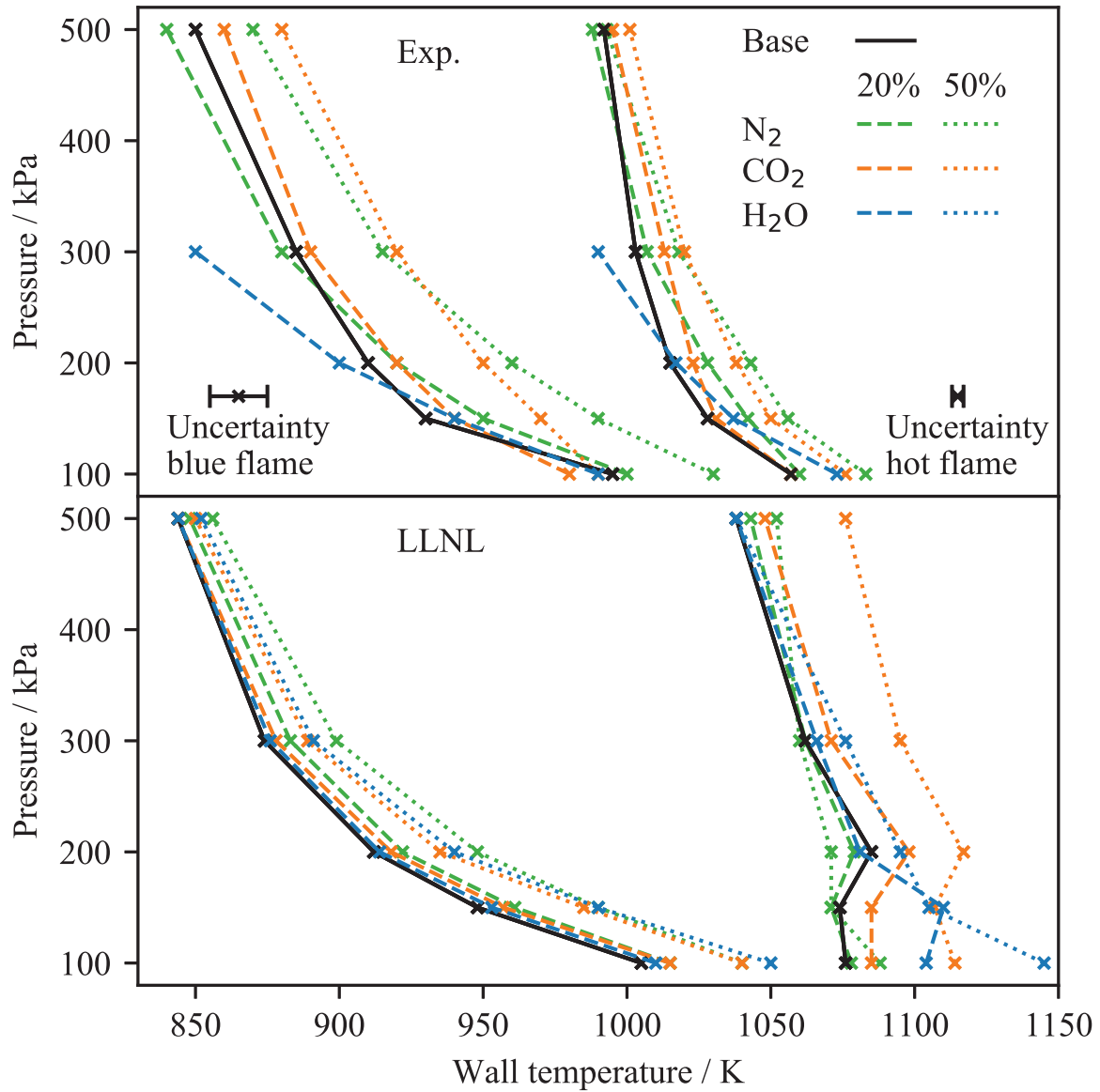


Figure 4.A.2: Wall temperature at the blue flame (left side) and hot flame positions (right side) of *iso*-octane at pressures between 100 kPa and 500 kPa as obtained by the experiment and computations by the LLNL mechanism, based on  $i_{\text{total}}$ . Diluents and dilution ratio are indicated by color and line style, black line represents the base case without dilution.

#### 4 The chemical and dilution effects of EGR on the reactivity of PRF

the peak of the heat release rate was used as the flame location and lead to even larger differences with the experiment, which was up to 65 K at 500 kPa. The cases with dilution showed similar trends of changing flame direction for increasing pressure, except for the 50% H<sub>2</sub>O case, which showed a shift of up to 69 K at 100 kPa as compared to the base case.

Overall, the results by LLNL showed good agreement with the experiment for the blue flame, while the locations of the hot flames only had poor agreement. This was caused by their changing direction as the pressure was increased and their locations being at higher wall temperatures than the experiment and the results by the modified KUCRS mechanism.

Figure 4.A.3 shows the flame locations of the cool flame, the blue flame and the hot flame of *n*-heptane for the experiment and the simulations by LLNL. Similar to the results for *iso*-octane, the results for the blue flame show good agreement except for dilution by H<sub>2</sub>O. Furthermore, the hot flames are located at up to 100 K higher wall temperatures than in the experiment. Additionally, the transition from the second to the third explosion limit is seen for all conditions except for the dilution by 50% H<sub>2</sub>O at pressures up to 300 kPa for the dilution by 50% N<sub>2</sub>. Similar to the results by the modified KUCRS mechanism (see Fig. 4.3.10), the cool flame is not affected by the addition of diluents. Again, LLNL shows agreeable results for lower temperatures but large discrepancies for the hot flame.

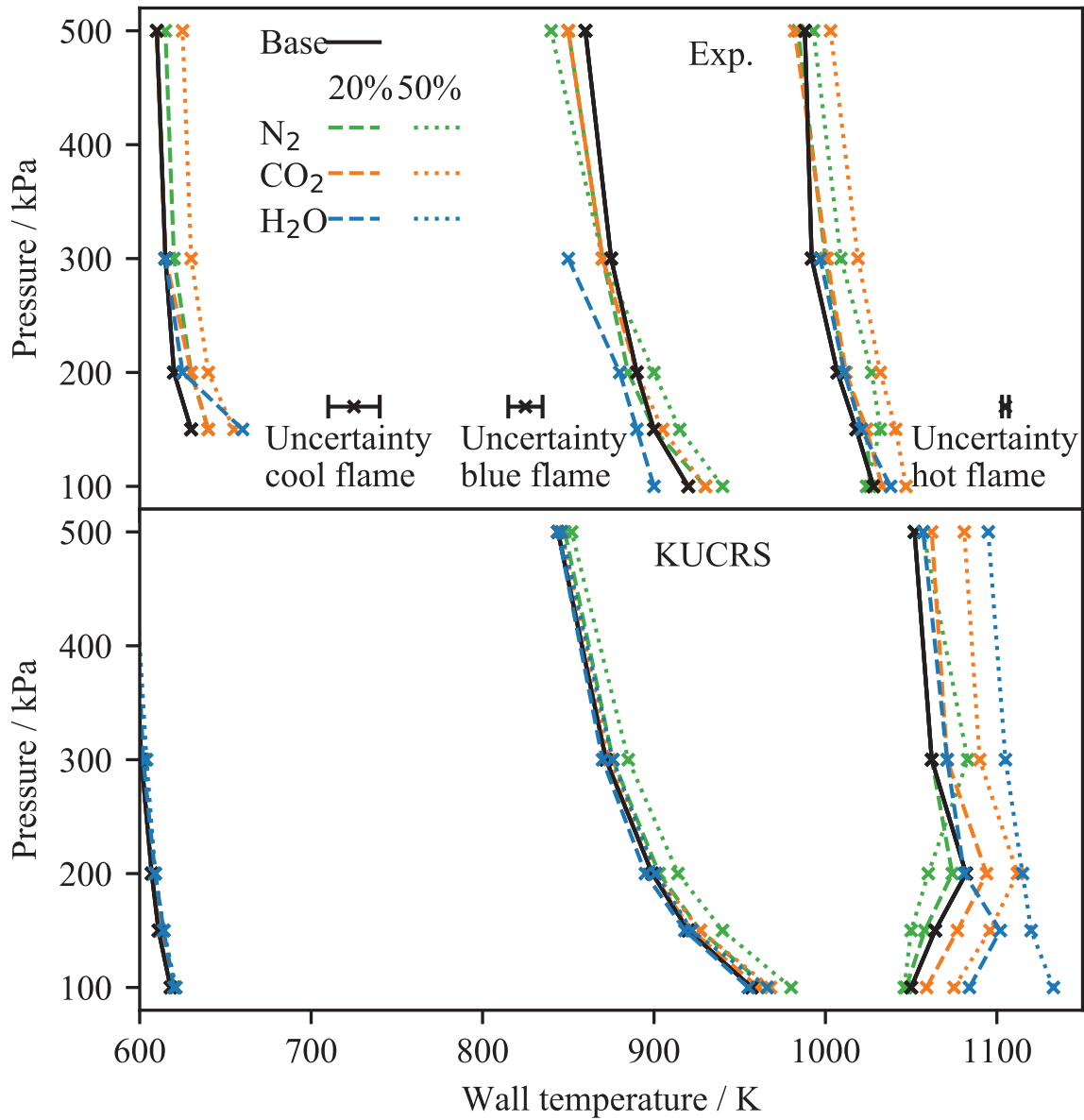


Figure 4.A.3: Wall temperature at the cool flame (left side), blue flame (middle) and hot flame positions (right side) of *n*-heptane at pressures between 100 kPa and 500 kPa as obtained by the experiment and computations by the LLNL mechanism, based on  $i_{\text{total}}$ . Diluents and dilution ratio are indicated by color and line style, black line represents the base case without dilution.



# 5 Conclusions and outlook

## 5.1 Conclusions

In this thesis, a novel method for the determination of fuel reactivity was developed based on separated weak flame in a micro flow reactor with a controlled temperature profile (MFR). To achieve higher resolution with regard to weak flame locations, a vertical-type MFR was constructed. Experimental results were complemented by one-dimensional steady computations by Chemkin-Pro. The capability of the vertical-type MFR was first tested on stoichiometric and ultra-lean ( $\Phi = 1.0, 0.75$  and  $0.5$ ) PRF/air (PRF100, 90, 80) weak flames at atmospheric pressure. The following conclusions were made:

- The new MFR allowed for a clear spatial separation of hot flames of fuels with differences in RON of 10.
- The new MFR allowed for a clear spatial separation of flames for difference in equivalence ratio of 0.25.
- It was found that computations by the KUCRS PRF mechanism showed the opposite trend for decreasing equivalence ratio as compared to the experiment and computations by the LLNL PRF mechanism.

## 5 Conclusions and outlook

- By analyzing the reactions and replacing seven hydrogen-oxygen reactions of the KUCRS mechanisms by those of FFCM, the trend for decreasing  $\Phi$  was inverted and very good agreement between the modified KUCRS mechanism and experimental results was achieved.
- This change of hydrogen-oxygen reactions did not show any effect on simulations of ignition delay times and laminar flame speed. Therefore, the MFR method offers a unique way to analyze chemical reactions and reaction mechanisms that is not possible by other approaches.

After it was shown that the MFR is capable of separating even small difference in reactivity, a reactivity index was developed that is based on separated weak flames. For this, the pressure inside the MFR was increased to 500 kPa, as this pressure is close to that at ignition in a spark-ignited gasoline engine. Investigations were conducted for fuels of RON between 0 and 100 and the following results were obtained:

- At elevated pressure, the fraction of heat that is released in the hot flame becomes independent of the base fuel as it mainly consists of hydrogen-oxygen reactions on CO oxidation, which are the same for all investigated hydrocarbon fuels.
- The fraction of heat release in the cool flame and the blue flame are inverse to each other and well describe fuel reactivity. Based on this finding, the heat contribution index (HCI) was developed.
- It was found the HCI does not directly correlate with the RON of the investigated fuels but that it was tied to the molecular structure of the fuel. Here, straight-chain molecules showed high reactivity whereas branched molecules showed low reactivity. These results agree well with previous investigations of critical compression ratios.

- To measure reactivity experimentally, formaldehyde concentrations were measured and the formaldehyde index was introduced. Experimental and computational results showed good agreement with each other as well as with the heat contribution index.

The final part of this thesis was the investigation of the chemical and dilution effects of the EGR constituents  $N_2$ ,  $CO_2$  and  $H_2O$  on the reactivity of PRF by separated weak flames. Here, elevated pressure of 500 kPa as well as dilution ratios of up to 50 % were chosen in order to investigate the effect on low, intermediate and high temperature reactivity. The following observations were made:

- The agreement of the computations by the modified KUCRS mechanism and the experiment with regard to blue flame and hot flame locations was poor. Up to this point, computational flame locations were defined as the points of maximum heat release rate. As experiments capture chemiluminescence, however, this comparison was not accurate.
- As chemiluminescence was filtered through a 431 nm band-pass filter, the captured photons were emitted by excited  $CH^*$  and  $CO_2^*$  radicals. Their photon emissions were calculated based on the computational results and a very good qualitative agreement with the experiment was found.
- Using this new method, it was found that while  $N_2$  and  $CO_2$  move blue flames and hot flames to higher wall temperatures,  $H_2O$  shifted to flames to lower wall temperatures.
- By analyzing reaction paths it was found that  $H_2O$  enhances the three-body chain branching reaction  $H_2O_2(+M) \rightleftharpoons OH + OH(+M)$ , which is especially important in the blue flame, where it increases reactivity.

- By analyzing the HCIs for EGR-like dilution it was found that these conditions have the strongest effect on high-reactivity fuels, such as *n*-heptane. Here, the decrease of reactivity corresponded to an increase of the RON by 28, whereas for *iso*-octane it was only 12.

## 5.2 Outlook

Based on this work, further investigations of fuel reactivity can be pursued. Future work on weak flames should employ the vertical-type MFR as it provides an improved resolution needed for reactivity measurement. The modifications to the KUCRS reaction mechanism that were done in this work make it applicable for a wide range of fuels and conditions, including ultra-lean and EGR conditions. Furthermore, comparison of flame locations should be based on the newly proposed photon emission calculations. The usage of the heat contribution index makes for an inexpensive investigation method as fuel consumption is minimal. Furthermore, it allows for separate investigation of low, intermediate and high temperature reactions. Future work might include investigations on more complex surrogates as well as investigate elementary reactions such as the three body reactions  $\text{H}_2\text{O}_2(+\text{M}) \rightleftharpoons \text{OH} + \text{OH}(+\text{M})$  and  $\text{H} + \text{O}_2(+\text{M}) \rightleftharpoons \text{HO}_2(+\text{M})$ .



## 6 Bibliography

- [1] S. Petit, World Vehicle Population Rose 4.6% in 2016 (2017).

URL <https://subscribers.wardsintelligence.com/analysis/world-vehicle-population-rose-46-2016>

- [2] International Energy Agency, Transport, Energy, and CO<sub>2</sub> (2009).

URL <https://www.iea.org/publications/freepublications/publication/transport2009.pdf>

- [3] International Energy Agency, CO<sub>2</sub> emissions from transport (% of total fuel combustion) (2014).

URL [iea.org/stats/index.asp](http://iea.org/stats/index.asp)

- [4] R. Sims, R. Schaeffer, F. Creutzig, X. Cruz-Núñez, M. D'Agosto, D. Dimitriu, M. J. Figueroa Meza, L. Fulton, S. Kobayashi, O. Lah, A. McKinnon, P. Newman, M. Ouyang, J. J. Schauer, D. Sperling, G. Tiwari, Climate Change 2014: Mitigation of Climate Change. Contribution of Working Group III to the Fifth Assessment Report of the Intergovernmental Panel on Climate Change, Cambridge University Press, Cambridge, United Kingdom and New York, NY, USA, 2014.

## 6 Bibliography

- [5] A. Bandivadekar, K. Bodek, L. Cheah, C. Evans, T. Groode, J. Heywood, E. Kasseris, M. Kromer, M. Weiss, On the road in 2035, Tech. Rep. July (2008).
- [6] G. Eads, 50by50 Prospects and Progress, Tech. rep. (2010).
- [7] J. B. Heywood, Internal Combustion Engine Fundamentals, McGraw-Hill Inc., 1988.
- [8] D. R. Lancaster, R. B. Krieger, J. H. Lienesch, Measurement and Analysis of Engine Pressure Data, SAE Technical Paper 750026 (1975).
- [9] Toyota, New 2.5-liter Direct-injection, Inline 4-cylinder Gasoline Engine (2016).  
URL <https://global.toyota/en/powertrain/engine/>
- [10] H. Mizuno, Nissan gasoline engine strategy for higher thermal efficiency, Combustion Engines 169 (2) (2017) 141–145.
- [11] SIP, SIP "Pioneering the Future: Japanese Science, Technology and Innovation 2015".  
URL [http://www8.cao.go.jp/cstp/panhu/sip\\_english/sip\\_en.html](http://www8.cao.go.jp/cstp/panhu/sip_english/sip_en.html)
- [12] Japan Science and Technology Agency, About SIP (2019).  
URL [http://www.jst.go.jp/sip/about\\_SIP.html](http://www.jst.go.jp/sip/about_SIP.html)
- [13] N. Iida, Research and development of super-lean burn for high efficiency SI engine challenge for innovative combustion technology to achieve 50% thermal efficiency, in: COMODIA 2017 - 9th International Conference on Modeling and Diagnostics for Advanced Engine Systems 2017, 2017, p. Code 129802.
- [14] J. Stokes, T. Lake, R. Osborne, A Gasoline Engine Concept for Improved Fuel Economy -The Lean Boost System, SAE Technical Paper 2000-01-29 (2000).

- [15] C. K. Law, *Combustion Physics*, Cambridge University Press, Cambridge, 2006.
- [16] N. Ladommatos, S. Abdelhalim, H. Zhao, Z. Hu, The dilution, chemical, and thermal effects of Exhaust Gas Recirculation on diesel engine emissions – Part 1: Effect of reducing inlet charge oxygen, SAE Technical Paper 961165 (1996).
- [17] N. Ladommatos, S. Abdelhalim, H. Zhao, Z. Hu, The dilution, chemical, and thermal effects of Exhaust Gas Recirculation on diesel engine emissions – Part 2: Effects of carbon dioxide, SAE Technical Paper 961167 (1996).
- [18] N. Ladommatos, S. Abdelhalim, H. Zhao, Z. Hu, The dilution, chemical, and thermal effects of Exhaust Gas Recirculation on diesel engine emissions – Part 3: Effects of water vapour, SAE Technical Paper 971659 (1997).
- [19] N. Ladommatos, S. Abdelhalim, H. Zhao, Z. Hu, The dilution, chemical, and thermal effects of Exhaust Gas Recirculation on diesel engine emissions – Part 4: Effects of carbon dioxide and water vapour, SAE Technical Paper 971660 (1997).
- [20] R. Chen, N. Milovanovic, A computational study into the effect of exhaust gas recycling on homogeneous charge compression ignition combustion in internal combustion engines fuelled with methane, *International Journal of Thermal Sciences* 41 (9) (2002) 805–813.
- [21] Y. Zeldovich, The oxidation of nitrogen in combustion and explosions, *Acta Physicochim USSR* 21 (1946) 557–560.
- [22] T. Li, D. Wu, M. Xu, Thermodynamic analysis of EGR effects on the first and second law efficiencies of a boosted spark-ignited direct-injection gasoline engine, *Energy Conversion and Management* 70 (2013) 130–138.

## 6 Bibliography

- [23] E. Galloni, G. Fontana, R. Palmaccio, Effects of exhaust gas recycle in a downsized gasoline engine, *Applied Energy* 105 (2013) 99–107.
- [24] F. Bozza, V. De Bellis, L. Teodosio, Potentials of cooled EGR and water injection for knock resistance and fuel consumption improvements of gasoline engines, *Applied Energy* 169 (2016) 112–125.
- [25] H. Wei, D. Feng, J. Pan, A. Shao, M. Pan, Knock characteristics of SI engine fueled with n-butanol in combination with different EGR rate, *Energy* 118 (2017) 190–196.
- [26] H. Zhao, Z. Peng, J. Williams, L. N., Understanding the effects of recycled burnt gases on the Controlled Autoignition (CAI) combustion in four-stroke gasoline engines, *SAE Technical Paper 2001-01-36* (2001).
- [27] H. Di, X. He, P. Zhang, Z. Wang, M. S. Wooldridge, C. K. Law, C. Wang, S. Shuai, J. Wang, Effects of buffer gas composition on low temperature ignition of iso-octane and n-heptane, *Combustion and Flame* 161 (10) (2014) 2531–2538.
- [28] M. Sjöberg, J. E. Dec, Effects of EGR and its constituents on HCCI autoignition of ethanol, *Proceedings of the Combustion Institute* 33 (2) (2011) 3031–3038.
- [29] M. Sjöberg, J. Dec, W. Hwang, Thermodynamic and chemical effects of EGR and its constituents on HCCI autoignition, *SAE Technical Paper 2007-01-0207* (2007).
- [30] J. Herzler, C. Naumann, Shock tube study of the influence of NO<sub>x</sub> on the ignition delay times of natural gas at high pressure, *Combustion Science and Technology* 184 (10-11) (2012) 1635–1650.
- [31] T. Le Cong, P. Dagaut, G. Dayma, Oxidation of Natural Gas, *Natural Gas/Syngas*

- Mixtures, and Effect of Burnt Gas Recirculation: Experimental and Detailed Kinetic Modeling, *Journal of Engineering for Gas Turbines and Power* 130 (4) (2008) 041502.
- [32] H. Curran, P. Gaffuri, W. Pitz, C. Westbrook, A comprehensive modeling study of iso-octane oxidation, *Combustion and Flame* 129 (3) (2002) 253–280.
- [33] M. Mehl, W. J. Pitz, C. K. Westbrook, H. J. Curran, Kinetic modeling of gasoline surrogate components and mixtures under engine conditions, *Proceedings of the Combustion Institute* 33 (1) (2011) 193–200.
- [34] E. Ranzi, A. Frassoldati, R. Grana, A. Cuoci, T. Faravelli, A. P. Kelley, C. K. Law, Hierarchical and comparative kinetic modeling of laminar flame speeds of hydrocarbon and oxygenated fuels, *Progress in Energy and Combustion Science* 38 (4) (2012) 468–501.
- [35] E. Ranzi, A. Frassoldati, A. Stagni, M. Pelucchi, A. Cuoci, T. Faravelli, Reduced kinetic schemes of complex reaction systems: Fossil and biomass-derived transportation fuels, *International Journal of Chemical Kinetics* 46 (9) (2014) 512–542.
- [36] A. Stagni, A. Cuoci, A. Frassoldati, T. Faravelli, E. Ranzi, Lumping and Reduction of Detailed Kinetic Schemes: an Effective Coupling, *Industrial & Engineering Chemistry Research* 53 (22) (2014) 9004–9016.
- [37] A. Cuoci, E. Ranzi, A. Frassoldati, T. Faravelli, A. Stagni, Skeletal mechanism reduction through species-targeted sensitivity analysis, *Combustion and Flame* 163 (2015) 382–393.
- [38] A. Miyoshi, Systematic Computational Study on the Unimolecular Reactions of Alkylperoxy ( $\text{RO}_2$ ), Hydroperoxyalkyl ( $\text{QOOH}$ ), and Hydroperoxyalkylperoxy

## 6 Bibliography

- (O<sub>2</sub>QOOH) Radicals, *The Journal of Physical Chemistry A* 115 (15) (2011) 3301–3325.
- [39] S. W. Benson, *Thermochemical Kinetics: Methods for the Estimation of Thermochemical Data and Rate Parameters*, 2nd Edition, Wiley, New York, 1976.
- [40] A. Miyoshi, Y. Sakai, Construction of a Detailed Kinetic Model for Gasoline Surrogate Mixtures, *Proceedings of the 2017 JSAE Annual Congress (Spring)* (2017).
- [41] A. Miyoshi, Y. Sakai, Construction of a detailed kinetic model for gasoline surrogate mixtures, *Transactions of Society of Automotive Engineers of Japan* 48 (5) (2017) 1021–1026.
- [42] A. Miyoshi, Y. Sakai, Construction of the gasoline surrogate detailed reaction mechanism, in: *JSAE Annual Congress Spring, 2017*, p. Paper number 20175311.
- [43] Y. Sakai, A. Miyoshi, Development of Reduced Chemical Kinetics Mechanism of Gasoline Surrogate Fuel, in: *The 28th Internal Combustion Engine Symposium, 2017*, p. Paper No. 20178019.
- [44] Y. Sakai, K. Hasegawa, A. Miyoshi, Development of Reduced Chemical Kinetics Mechanism of Gasoline Surrogate Fuel with Oxygenated Compounds, in: *The 29th Internal Combustion Engine Symposium, 2018*, p. Paper No. 20183155.
- [45] A. Gaydon, I. Hurle, *The shock tube in high-temperature chemical physics*, Reinhold Pub., New York, 1963.
- [46] R. Hanson, D. Davidson, *Recent advances in laser absorption and shock tube methods*

- for studies of combustion chemistry, *Progress in Energy and Combustion Science* 44 (2014) 103–114.
- [47] A. R. Amadio, M. W. Crofton, E. L. Petersen, Test-time extension behind reflected shock waves using CO<sub>2</sub>–He and C<sub>3</sub>H<sub>8</sub>–He driver mixtures, *Shock Waves* 16 (2) (2006) 157–165.
- [48] M. F. Campbell, R. M. Spearrin, A. M. Tulgestke, D. F. Davidson, R. K. Hanson, T. Parise, Strategies for obtaining long constant-pressure test times in shock tubes, *Shock Waves* 25 (6) (2015) 651–665.
- [49] R. Sivaramakrishnan, K. Brezinsky, H. Vasudevan, R. Tranter, A SHOCK-TUBE STUDY OF THE HIGH-PRESSURE THERMAL DECOMPOSITION OF BENZENE, *Combustion Science and Technology* 178 (1-3) (2006) 285–305.
- [50] U. Burke, W. K. Metcalfe, S. M. Burke, K. A. Heufer, P. Dagaut, H. J. Curran, A detailed chemical kinetic modeling, ignition delay time and jet-stirred reactor study of methanol oxidation, *Combustion and Flame* 165 (2016) 125–136.
- [51] H. Curran, P. Gaffuri, W. Pitz, C. Westbrook, A Comprehensive Modeling Study of n-Heptane Oxidation, *Combustion and Flame* 114 (1-2) (1998) 149–177.
- [52] R. S. Tranter, K. Brezinsky, D. Fulle, Design of a high-pressure single pulse shock tube for chemical kinetic investigations, *Review of Scientific Instruments* 72 (7) (2001) 3046–3054.
- [53] A. Farooq, J. B. Jeffries, R. K. Hanson, Sensitive detection of temperature behind reflected shock waves using wavelength modulation spectroscopy of CO<sub>2</sub> near 2.7  $\mu\text{m}$ , *Applied Physics B: Lasers and Optics* 96 (1) (2009) 161–173.

## 6 Bibliography

- [54] J. M. Hall, E. L. Petersen, An optimized kinetics model for OH chemiluminescence at high temperatures and atmospheric pressures, *International Journal of Chemical Kinetics* 38 (12) (2006) 714–724.
- [55] C.-J. Sung, H. J. Curran, Using rapid compression machines for chemical kinetics studies, *Progress in Energy and Combustion Science* 44 (2014) 1–18.
- [56] S. S. Goldsborough, S. Hochgreb, G. Vanhove, M. S. Wooldridge, H. J. Curran, C.-J. Sung, Advances in rapid compression machine studies of low- and intermediate-temperature autoignition phenomena, *Progress in Energy and Combustion Science* 63 (2017) 1–78.
- [57] G. Mittal, M. Chaos, C. J. Sung, F. L. Dryer, Dimethyl ether autoignition in a rapid compression machine: Experiments and chemical kinetic modeling, *Fuel Processing Technology* 89 (12) (2008) 1244–1254.
- [58] H. J. Curran, P. Gaffuri, W. J. Pitz, C. K. Westbrook, W. R. Leppard, Autoignition chemistry in a motored engine: An experimental and kinetic modeling study, *Symposium (International) on Combustion* 26 (2) (1996) 2669–2677.
- [59] ASTM International, ASTM D2699-18a, Standard Test Method for Research Octane Number of Spark-Ignition Engine Fuel (2018).  
URL <https://www.astm.org/Standards/D2699.htm>
- [60] ASTM International, ASTM D2700-18a, Standard Test Method for Motor Octane Number of Spark-Ignition Engine Fuel (2018).  
URL <https://www.astm.org/Standards/D2700.htm>



- [61] G. Kalghatgi, Fuel Anti-Knock Quality - Part I. Engine Studies, SAE Technical Paper 2001-01-3584 (2001).
- [62] K. Maruta, T. Kataoka, N. I. Kim, S. Minaev, R. Fursenko, Characteristics of combustion in a narrow channel with a temperature gradient, *Proceedings of the Combustion Institute* 30 (2) (2005) 2429–2436.
- [63] S. Minaev, K. Maruta, R. Fursenko, Nonlinear dynamics of flame in a narrow channel with a temperature gradient, *Combustion Theory and Modelling* 11 (2) (2007) 187–203.
- [64] Y. Saiki, Y. Suzuki, Effect of wall surface reaction on a methane-air premixed flame in narrow channels with different wall materials, *Proceedings of the Combustion Institute* 34 (2) (2013) 3395–3402.
- [65] Y. Saiki, Y. Fan, Y. Suzuki, Radical quenching of metal wall surface in a methane-air premixed flame, *Combustion and Flame* 162 (10) (2015) 4036–4045.
- [66] A. Di Stazio, C. Chauveau, G. Dayma, P. Dagaut, Combustion in micro-channels with a controlled temperature gradient, *Experimental Thermal and Fluid Science* 73 (2016) 79–86.
- [67] S. Lapointe, C. L. Druzgalski, M. J. McNenly, Numerical study of a micro flow reactor at engine pressures: Flames with repetitive extinction and ignition and simulations with a reduced chemical model, *Combustion and Flame* 197 (2018) 102–110.
- [68] H. Nakamura, A. Yamamoto, M. Hori, T. Tezuka, S. Hasegawa, K. Maruta, Study on pressure dependences of ethanol oxidation by separated weak flames in a micro

## 6 Bibliography

- flow reactor with a controlled temperature profile, *Proceedings of the Combustion Institute* 34 (2) (2013) 3435–3443.
- [69] Y. Tsuboi, T. Yokomori, K. Maruta, Lower limit of weak flame in a heated channel, *Proceedings of the Combustion Institute* 32 (2) (2009) 3075–3081.
- [70] Y. Kizaki, H. Nakamura, T. Tezuka, S. Hasegawa, K. Maruta, Effect of radical quenching on CH<sub>4</sub>/air flames in a micro flow reactor with a controlled temperature profile, *Proceedings of the Combustion Institute* 35 (3) (2015) 3389–3396.
- [71] F. E. Fendell, Ignition and extinction in combustion of initially unmixed reactants, *Journal of Fluid Mechanics* 21 (2) (1965) 281–303.
- [72] T. Kamada, H. Nakamura, T. Tezuka, S. Hasegawa, K. Maruta, Study on combustion and ignition characteristics of natural gas components in a micro flow reactor with a controlled temperature profile, *Combustion and Flame* 161 (1) (2014) 37–48.
- [73] M. Hori, A. Yamamoto, H. Nakamura, T. Tezuka, S. Hasegawa, K. Maruta, Study on octane number dependence of PRF/air weak flames at 1-5 atm in a micro flow reactor with a controlled temperature profile, *Combustion and Flame* 159 (3) (2012) 959–967.
- [74] M. Hori, H. Nakamura, T. Tezuka, S. Hasegawa, K. Maruta, Characteristics of n-heptane and toluene weak flames in a micro flow reactor with a controlled temperature profile, *Proceedings of the Combustion Institute* 34 (2) (2013) 3419–3426.
- [75] S. Kikui, T. Kamada, H. Nakamura, T. Tezuka, S. Hasegawa, K. Maruta, Characteristics of n-butane weak flames at elevated pressures in a micro flow reactor with

- a controlled temperature profile, *Proceedings of the Combustion Institute* 35 (3) (2015) 3405–3412.
- [76] H. Nakamura, H. Takahashi, T. Tezuka, S. Hasegawa, K. Maruta, K. Abe, Effects of CO-to-H<sub>2</sub> ratio and diluents on ignition properties of syngas examined by weak flames in a micro flow reactor with a controlled temperature profile, *Combustion and Flame* 172 (2016) 94–104.
- [77] H. Oshibe, H. Nakamura, T. Tezuka, S. Hasegawa, K. Maruta, Stabilized three-stage oxidation of DME/air mixture in a micro flow reactor with a controlled temperature profile, *Combustion and Flame* 157 (8) (2010) 1572–1580.
- [78] S. Kikui, H. Nakamura, T. Tezuka, S. Hasegawa, K. Maruta, Study on combustion and ignition characteristics of ethylene, propylene, 1-butene and 1-pentene in a micro flow reactor with a controlled temperature profile, *Combustion and Flame* 163 (2016) 209–219.
- [79] S. Suzuki, M. Hori, H. Nakamura, T. Tezuka, S. Hasegawa, K. Maruta, Study on cetane number dependence of diesel surrogates/air weak flames in a micro flow reactor with a controlled temperature profile, *Proceedings of the Combustion Institute* 34 (2) (2013) 3411–3417.
- [80] T. Okuno, H. Nakamura, T. Tezuka, S. Hasegawa, K. Maruta, Ultra-lean combustion characteristics of premixed methane flames in a micro flow reactor with a controlled temperature profile, *Proceedings of the Combustion Institute* 36 (3) (2017) 4227–4233.
- [81] D. Bradley, M. Lawes, C. G. W. Sheppard, *Combustion and the thermodynamic*

## 6 Bibliography

- performance of spark ignition engines, *Proceedings of the Institution of Mechanical Engineers, Part C: Journal of Mechanical Engineering Science* 214 (1) (2000) 257–268.
- [82] B. Gauthier, D. Davidson, R. Hanson, Shock tube determination of ignition delay times in full-blend and surrogate fuel mixtures, *Combustion and Flame* 139 (4) (2004) 300–311.
- [83] J. Andrae, P. Björnbohm, R. Cracknell, G. Kalghatgi, Autoignition of toluene reference fuels at high pressures modeled with detailed chemical kinetics, *Combustion and Flame* 149 (1-2) (2007) 2–24.
- [84] S. M. Sarathy, G. Kukkadapu, M. Mehl, W. Wang, T. Javed, S. Park, M. A. Oehlschlaeger, A. Farooq, W. J. Pitz, C.-J. Sung, Ignition of alkane-rich FACE gasoline fuels and their surrogate mixtures, *Proceedings of the Combustion Institute* 35 (1) (2015) 249–257.
- [85] M. Hartmann, I. Gushterova, M. Fikri, C. Schulz, R. Schießl, U. Maas, Auto-ignition of toluene-doped n-heptane and iso-octane/air mixtures: High-pressure shock-tube experiments and kinetics modeling, *Combustion and Flame* 158 (1) (2011) 172–178.
- [86] T. Javed, C. Lee, M. AlAbbad, K. Djebbi, M. Beshir, J. Badra, H. Curran, A. Farooq, Ignition studies of n-heptane/iso-octane/toluene blends, *Combustion and Flame* 171 (2016) 223–233.
- [87] M. AlAbbad, T. Javed, F. Khaled, J. Badra, A. Farooq, Ignition delay time measurements of primary reference fuel blends, *Combustion and Flame* 178 (2017) 205–216.

- [88] B. Chen, C. Togbé, H. Selim, P. Dagaut, S. M. Sarathy, Quantities of Interest in Jet Stirred Reactor Oxidation of a High-Octane Gasoline, *Energy & Fuels* 31 (5) (2017) 5543–5553.
- [89] G. Kukkadapu, K. Kumar, C.-J. Sung, M. Mehl, W. J. Pitz, Experimental and surrogate modeling study of gasoline ignition in a rapid compression machine, *Combustion and Flame* 159 (10) (2012) 3066–3078.
- [90] G. Kukkadapu, K. Kumar, C.-J. Sung, M. Mehl, W. J. Pitz, Autoignition of gasoline surrogates at low temperature combustion conditions, *Combustion and Flame* 162 (5) (2015) 2272–2285.
- [91] A. Yamamoto, H. Oshibe, H. Nakamura, T. Tezuka, S. Hasegawa, K. Maruta, Stabilized three-stage oxidation of gaseous n-heptane/air mixture in a micro flow reactor with a controlled temperature profile, *Proceedings of the Combustion Institute* 33 (2) (2011) 3259–3266.
- [92] ANSYS Inc., CHEMKIN-PRO 17.2 (2016).
- [93] G. Smith, Y. Tao, H. Wang, Foundational Fuel Chemistry Model Version 1.0 (FFCM-1) (2016).  
URL <http://nanoenergy.stanford.edu/ffcm1>
- [94] M. P. Burke, M. Chaos, Y. Ju, F. L. Dryer, S. J. Klippenstein, Comprehensive H<sub>2</sub>/O<sub>2</sub> kinetic model for high-pressure combustion, *International Journal of Chemical Kinetics* 44 (7) (2012) 444–474.
- [95] C. Kappel, K. Luther, J. Troe, Shock wave study of the unimolecular dissociation of

## 6 Bibliography

- H<sub>2</sub>O<sub>2</sub> in its falloff range and of its secondary reactions, *Physical Chemistry Chemical Physics* 4 (18) (2002) 4392–4398.
- [96] H. Hippler, H. Neunaber, J. Troe, Shock wave studies of the reactions  $\text{HO} + \text{H}_2\text{O}_2 \Rightarrow \text{H}_2\text{O} + \text{HO}_2$  and  $\text{HO} + \text{HO}_2 \Rightarrow \text{H}_2\text{O} + \text{O}_2$  between 930 and 1680 K, *The Journal of Chemical Physics* *The Journal of Chemical Physics* *The Journal of Chemical Physics* 1031 (129) (1995) 1755–14506.
- [97] M. P. Burke, S. J. Klippenstein, L. B. Harding, A quantitative explanation for the apparent anomalous temperature dependence of  $\text{OH} + \text{HO}_2 = \text{H}_2\text{O} + \text{O}_2$  through multi-scale modeling, *Proceedings of the Combustion Institute* 34 (1) (2013) 547–555.
- [98] W. B. DeMore, Reaction of hydroperoxo radicals with ozone and the effect of water vapor on hydroperoxo kinetics, *The Journal of Physical Chemistry* 83 (9) (1979) 1113–1118.
- [99] W. B. DeMore, Rate constant and possible pressure dependence of the reaction hydroxyl + hydroperoxo, *The Journal of Physical Chemistry* 86 (1) (1982) 121–126.
- [100] U. C. Sridharan, L. X. Qiu, F. Kaufman, Rate constant of the hydroxyl + perhydroxyl ( $\text{HO}_2$ ) reaction from 252 to 420 K, *The Journal of Physical Chemistry* 88 (7) (1984) 1281–1282.
- [101] L. F. Keyser, Kinetics of the reaction hydroxyl + hydroperoxo  $\Rightarrow$  water + oxygen from 254 to 382 K, *The Journal of Physical Chemistry* 92 (5) (1988) 1193–1200.
- [102] R.-R. Lii, R. A. Gorse, M. C. Sauer, S. Gordon, Temperature dependence of the gas-phase self-reaction of hydroperoxo radicals in the presence of ammonia, *The Journal of Physical Chemistry* 84 (8) (1980) 813–817.

- [103] R. Cox, J. Burrows, T. Wallington, Rate coefficient for the reaction  $\text{OH} + \text{HO}_2 = \text{H}_2\text{O} + \text{O}_2$  at 1 atmosphere pressure and 308 K, *Chemical Physics Letters* 84 (2) (1981) 217–221.
- [104] M. J. Kurylo, O. Klais, A. H. Laufer, Mechanistic investigation of the hydroxyl + hydroperoxo reaction, *The Journal of Physical Chemistry* 85 (24) (1981) 3674–3678.
- [105] M. Braun, A. Hofzumahaus, F. Stuhl, VUV Flash Photolysis Study of the Reaction of HO with HO<sub>2</sub> at 1 atm and 298 K, *Berichte der Bunsengesellschaft für physikalische Chemie* 86 (7) (1982) 597–602.
- [106] H. Hippler, J. Troe, Rate constants of the reaction  $\text{HO} + \text{H}_2\text{O}_2 \Rightarrow \text{HO}_2 + \text{H}_2\text{O}$  at  $T > 1000$  K, *Chemical Physics Letters* 192 (4) (1992) 333–337.
- [107] N. K. Srinivasan, M.-C. Su, J. W. Sutherland, J. V. Michael, B. Ruscic, Reflected Shock Tube Studies of High-Temperature Rate Constants for  $\text{OH} + \text{NO}_2 \rightarrow \text{HO}_2 + \text{NO}$  and  $\text{OH} + \text{HO}_2 \rightarrow \text{H}_2\text{O} + \text{O}_2^\ddagger$ , *J. Phys. Chem. A* 110 (2006) 6602–6607.
- [108] Z. Hong, S. S. Vasu, D. F. Davidson, R. K. Hanson, Experimental Study of the Rate of  $\text{OH} + \text{HO}_2 \rightarrow \text{H}_2\text{O} + \text{O}_2$  at High Temperatures Using the Reverse Reaction, *The Journal of Physical Chemistry A* 114 (17) (2010) 5520–5525.
- [109] J. M. Goodings, A. N. Hayhurst, Heat release and radical recombination in premixed fuel-lean flames of  $\text{H}_2 + \text{O}_2 + \text{N}_2$ . Rate constants for  $\text{H} + \text{OH} + \text{M} \rightarrow \text{H}_2\text{O} + \text{M}$  and  $\text{HO}_2 + \text{OH} \rightarrow \text{H}_2\text{O} + \text{O}_2$ , *Journal of the Chemical Society, Faraday Transactions 2* 84 (6) (1988) 745.
- [110] J. Peeters, G. Mahnen, Reaction mechanisms and rate constants of elementary steps

## 6 Bibliography

- in methane-oxygen flames, Symposium (International) on Combustion 14 (1) (1973) 133–146.
- [111] M. Chaos, F. L. Dryer, Syngas Combustion Kinetics and Applications, *Combustion Science and Technology* 180 (6) (2008) 1053–1096.
- [112] C. L. Rasmussen, J. Hansen, P. Marshall, P. Glarborg, Experimental measurements and kinetic modeling of CO/H<sub>2</sub>/O<sub>2</sub>/NO<sub>x</sub> conversion at high pressure, *International Journal of Chemical Kinetics* 40 (8) (2008) 454–480.
- [113] R. Sivaramakrishnan, A. Comandini, R. Tranter, K. Brezinsky, S. Davis, H. Wang, Combustion of CO/H<sub>2</sub> mixtures at elevated pressures, *Proceedings of the Combustion Institute* 31 (1) (2007) 429–437.
- [114] W. G. Lovell, Knocking Characteristics of Hydrocarbons, *Industrial and Engineering Chemistry* 40 (12) (1948) 2388–2438.
- [115] A. Walsh, The knock ratings of fuels, Symposium (International) on Combustion 9 (1) (1963) 1046–1055.
- [116] J. Griffiths, P. Halford-Maw, C. Mohamed, Spontaneous ignition delays as a diagnostic of the propensity of alkanes to cause engine knock, *Combustion and Flame* 111 (4) (1997) 327–337.
- [117] C. Westbrook, W. Pitz, J. Boercker, H. Curran, J. Griffiths, C. Mohamed, M. Ribaucour, Detailed chemical kinetic reaction mechanisms for autoignition of isomers of heptane under rapid compression, *Proceedings of the Combustion Institute* 29 (1) (2002) 1311–1318.



- [118] S. Tanaka, F. Ayala, J. C. Keck, J. B. Heywood, Two-stage ignition in HCCI combustion and HCCI control by fuels and additives, *Combustion and Flame* 132 (1) (2003) 219–239.
- [119] E. J. Silke, H. J. Curran, J. M. Simmie, The influence of fuel structure on combustion as demonstrated by the isomers of heptane: a rapid compression machine study, *Proceedings of the Combustion Institute* 30 (2) (2005) 2639–2647.
- [120] J. A. Badra, N. Bokhumseen, N. Mulla, S. M. Sarathy, A. Farooq, G. Kalghatgi, P. Gaillard, A methodology to relate octane numbers of binary and ternary n-heptane, iso-octane and toluene mixtures with simulated ignition delay times, *Fuel* 160 (2015) 458–469.
- [121] F. Buda, R. Bounaceur, V. Warth, P. Glaude, R. Fournet, F. Battin-Leclerc, Progress toward a unified detailed kinetic model for the autoignition of alkanes from C4 to C10 between 600 and 1200 K, *Combustion and Flame* 142 (1-2) (2005) 170–186.
- [122] P. Grajetzki, H. Nakamura, T. Tezuka, S. Hasegawa, K. Maruta, Evaluation of the reactivity of ultra-lean PRF/air mixtures by weak flames in a micro flow reactor with a controlled temperature profile, *Combustion Science and Technology* 190 (11) (2018) 1950–1970.
- [123] P. Grajetzki, H. Nakamura, T. Tezuka, S. Hasegawa, K. Maruta, A novel reactivity index for SI engine fuels by separated weak flames in a micro flow reactor with a controlled temperature profile, *Fuel* 245 (June 2019) (2019) 429–437.
- [124] V. N. Nori, J. M. Seitzman, *Chemiluminescence Measurements and Modeling in*

## 6 Bibliography

- Syngas, Methane and Jet-A Fueled Combustors, 45th AIAA Aerospace Sciences Meeting and Exhibit (2007).
- [125] S. A. Carl, M. Van Poppel, J. Peeters, Identification of the  $\text{CH} + \text{O}_2 \rightarrow \text{OH}(\text{A}) + \text{CO}$  Reaction as the Source of  $\text{OH}(\text{A-X})$  Chemiluminescence in  $\text{C}_2\text{H}_2/\text{O}/\text{H}/\text{O}_2$  Atomic Flames and Determination of Its Absolute Rate Constant over the Range  $T = 296$  to  $511$  K, *J. Phys. Chem. A* 1077 (2003) 11001–11007.
- [126] M. Tamura, P. A. Berg, J. E. Harrington, J. Luque, J. B. Jeffries, G. P. Smith, D. R. Crosley, Collisional Quenching of  $\text{CH}(\text{A})$ ,  $\text{OH}(\text{A})$ , and  $\text{NO}(\text{A})$  in Low Pressure Hydrocarbon Flames, *Combustion and Flame* 114 (3-4) (1998) 502–514.
- [127] A. Pravilov, L. Smirnova, Temperature Dependence of the Spectral Distribution of the Rate Constant of Chemiluminescence in the Reaction  $\text{O}(3\text{P}) + \text{CO} \rightarrow \text{CO}_2 + \text{h}\nu$ , *Kinetics and Catalysis* 22 (4) (1985) 832–838.
- [128] M. Slack, A. Grillo, High temperature rate coefficient measurements of  $\text{CO} + \text{O}$  chemiluminescence, *Combustion and Flame* 59 (2) (1985) 189–196.
- [129] A. Gaydon, H. Wolfhard, *Flames: Their Structure, Radiation, and Temperature*, fourth edi Edition, Chapman and Hall, 1978.
- [130] V. N. Nori, J. M. Seitzman,  $\text{CH}^*$  chemiluminescence modeling for combustion diagnostics, *Proceedings of the Combustion Institute* 32 I (1) (2009) 895–903.
- [131] U.S. Department of Energy Efficiency and Renewable Energy Office of Transportation Technologies, Homogeneous Charge Compression Ignition (HCCI) Technology-A Report to the U.S. Congress, Tech. rep. (2001).

- [132] Z. Zheng, M. Yao, Numerical study on the chemical reaction kinetics of n-heptane for HCCI combustion process, *Fuel* 85 (17-18) (2006) 2605–2615.



## 7 Acknowledgments

I would like to take the opportunity and express my sincere gratitude to all the people that contributed in one way or another to my research and this thesis. First of all, I want to thank my supervisor Prof. Kaoru Maruta for the opportunity that he has given me. I deeply appreciate all the support and encouragement and the stimulating discussions we had. Furthermore, I want to thank Prof. Hisashi Nakamura for his important insights and all the fruitful discussion we had over the years. I am also grateful to Prof. Hideaki Kobayashi for his time and effort that went into reviewing this thesis.

This thesis would not have been possible without the help of the staff of the Energy Dynamics Lab. Mr. Takuya Tezuka was an indispensable help in preparing and performing experiments. The experience and skill of Mr. Susumu Hasegawa also contributed to successful experiments. On the administrative side, Ms. Hiromi Ito was a big support throughout my time here. More recently, Ms. Reiko Chiba also was a great help with administrative work.

Since coming to this lab, I received tremendous help from its students. I especially want to thank Mr. Hiroki Takahashi and Mr. Tomohiro Tanaka for being my tutors and helping me getting settled in Sendai. Furthermore, I want to thank Dr. Xing Li and Mr. Takakazu Onishi for getting me acquainted with combustion research in the beginning

## *Acknowledgments*

of my stay. Every single lab member contributed to the positive atmosphere and the exchange of ideas and information. These people are Mr. Taiki Kamada, Mr. Satoshi Suzuki, Mr. Yuta Kizaki, Mr. Yuji Kuwayama, Mr. Koichi Takase, Mr. Shogo Kikui, Mr. Takashige Shimizu, Mr. Shogo Onishi, Ms. Saho Yajima, Dr. Ajit Kumar Dubey, Mr. Jiayan Lyu, Mr. Takahiro Onda, Mr. Takayuki Monobe, Dr. Tomoya Okuno, Mr. Ryota Tatsumi, Mr. Yuta Sasaki, Mr. Yuma Daimaru, Mr. Jun Zenpou, Mr. Mohd Hafidzal Bin Mohd Hanafi, Mr. Yuki Murakami, Mr. Shintaro Takahashi, Mr. Toru Sugita, Mr. Ryota Nakada, Mr. Kodai Uesugi, Mr. Mitsumasa Shindo, Mr. Keisuke Akita, Mr. Takaki Akiba, Mr. Keisuke Kanayama, Mr. Shota Morikura, Mr. Taichi Mukoyama and Mr. Yoshimichi Yamamoto. I also would like to thank our short-term international students and researchers Dr. Mohammad Akram, Mr. Alizeb Hussain Syed, Ms. Imene Radhouane, Mr. Branko Tanchev, Mr. Alejandro Monsech Hernandez, Mr. Dominic Kevin Fernandes, Mr. Maciek Cichonski, Ms. Ann Wambuku Waireri, Dr. Ryan James Milcarek, Mr. Marcus Stein, Dr. Olivier Mathieu and Ms. Kari Lovise Ness.

My sincere gratitude goes to my family who always encouraged and supported me on my way. I especially want to thank my wife Gabriela for her love and support and for always being by my side during this not always easy time.

This work was partially supported by Council for Science, Technology and Innovation (CSTI), Cross-Ministerial Strategic Innovation Promotion Program (SIP), Innovative Combustion Technology (Japan Science and Technology), grant number 18-141008568. I would also like to thank Tohoku University for the Tohoku University President Fellowship and the Institute of Fluid Science for their support through 卓越した大学院拠点形成支援事業"流動ダイナミクス知の融合教育研究世界拠点".